THGEM BASED NEUTRON IMAGING SYSTEM

DEVELOPMENT OF AN ADVANCED GASEOUS NEUTRON IMAGING SYSTEM BASED ON THICK GAS ELECTRON MULTIPLIERS WITH 2D DELAY LINE READOUT

BY

DEVIN STEWARD MAXWELL BURKE, M.Sc,

McMaster University, Hamilton, Canada

A THESIS

SUBMITTED TO THE DEPARTMENT OF PHYSICS AND ASTRONOMY

AND THE SCHOOL OF GRADUATE STUDIES

OF MCMASTER UNIVERSITY

IN PARTIAL FULFILMENT OF THE REQUIREMENTS

FOR THE DEGREE OF

DOCTOR OF PHYSICS AND ASTRONOMY

© Copyright by Devin Steward Maxwell Burke, April 2021

All Rights Reserved

Doctor of Physics and Astronomy (2021) McMaster University

(Physics and Astronomy) Hamilton, Ontario, Canada

TITLE:	Development of an advanced gaseous neutron imaging system based on thick gas electron multipliers with 2D delay line readout
AUTHOR:	Devin Steward Maxwell Burke M.Sc. (Nuclear Astrophysics), McMaster University, Hamilton, Canada
SUPERVISOR:	Dr. Soo Hyun Byun
NUMBER OF PAGES:	xix, 139

Lay Abstract

In this work is presented the development process of a novel and cost-effective neutron imaging system capable of imaging soft biological and dense materials that X-rays are unable to penetrate. Such a system may be scaled to large areas for many applications including the study of large archeological objects or employed as a security measure to monitor border checkpoints for transportation of controlled radioactive materials.

Abstract

Neutron imaging is a non-destructive technique with many applications in diverse fields such as industrial quality assurance, archaeology, and border security. However with the high cost of the standard fill gas ^{3}He and the high cost of scaling conventional digital imaging systems to large areas its applications are limited. Here is presented the proof of concept for a gaseous neutron imaging system utilizing a $^{10}B_4C$ solid state converter and THGEM technology and 2D passive delay line readout. THGEMs used for signal amplification can be produced cost-effectively and in large areas by PCB manufacturers. This combined with the reduced channel processing requirements of delay lines over individual pixel readouts results in a cost effective and scalable system when compared to similar designs using solid state multipliers such as silicon photo-multipliers. Here is presented a proof of concept of this imaging system with data acquisition accomplished by digitization and offline image reconstruction achieving mean X and Y resolution of $\langle\sigma_X\rangle = (1.37 \pm 0.24)$ mm and $\langle\sigma_Y\rangle = (1.15 \pm 0.13)$ mm respectively. Studied in parallel with this system is the effectiveness of gadolinium oxide based paint as a thermal neutron shield and image contrast agent.

To my parents, Michelle and Donald

who have always supported me.

Acknowledgements

This document wouldn't exist without the support of dozens of people who have contributed it in the form of expert advice, academic supervision, mechanical expertise and emotional support. I would first like to thank Dr. Soo Hyun Byun, my academic supervisor. He has always supported my ideas and contributions to this project and others. Being always ready and able to listen and brainstorm with his students, and always willing to lend his personal hands-on support to any task he is the best kind of supervisor any student could ask for. I would like to thank the other members of my supervisory committee Dr. David Chettle, Dr. Alan Chen, and Dr. Troy Farncombe for their advice and editorial contributions to my work. I would also like to thank Justin Bennett for always being an enthusiastic supporter of my work and all of the radiation science graduate program students. Justin provided invaluable mechanical and technical advice throughout the entirety of this project and us graduate students would be far worse for his absence. There are several advisors I have benefited from throughout this work I would like to thank who were always happy to provide their help and advice. These people include Dr. Andrei Hanu who developed the delay line and hardware DAQ, Dr. Carina Höglund and her collaborators at the ESS, and Marco Locatelli and Pierluigi from CAEN. I would also like to thank all the friends I have known over the past 12 years and the other students in the graduate program.

When I think back at the innumerable discussions we have had, the good times, and all the support I have received and reciprocated I know I could not have gotten this far without you. I want to thank the teachers and professors I have had the incredible fortune to have studied under over the years who instilled in me my passion for science and at least a small portion of their knowledge to help me on my way. Finally I want to thank my family for their unerring support my whole life. They have always pushed me to accomplish anything I set my mind to and it's primarily thanks to their effort and sacrifices that I am able to write these words.

Contents

List of Figures

List of Tables

List of Acronyms

CCD charge-coupled device

CFD constant fraction discriminator

DAQ data acquisition system

ECL emitter-coupled logic

ESF edge spread function

ESS European Spallation Source

FPGA field-programmable gate array

FMC FPGA Mezzanine Card

FWHM full width at half maximum

FIFO first in, first out

GEM gas electron multiplier

GUI graphical user interface

HDL hardware description language

HV high voltage

IAEA International Atomic Energy Agency

IC integrated circuit

LPC low pin count

LVTTL low voltage transistor-transistor logic

MAD McMaster alignment diffractometer

MICROMEGAS MICRO MEsh GAseous Structure

MNR McMaster Nuclear Reactor

NIM nuclear instrumentation module

PCB printed circuit board

PSF point spread function

RETGEM resistive thick gas electron multiplier

RPM radiation portal monitor

SiPM silicon photomultiplier

SNM special nuclear materials

TDC time-to-digital converter

TDC-DAQ time-to-digital converter data acquisition system

TEP tissue equivalent propane

THGEM thick gas electron multiplier

TTL transistor-transistor logic

UART universal asynchronous receiver/transmitter

Chapter 1

Introduction

1.1 Neutron imaging: applications and demand

Neutron imaging is a versatile and growing [1] practice of non-destructive imaging that can be used to probe a wide range of materials in fields such as renewable energy [2], nuclear power [3], biology [4], and archeology [5]. Neutron imaging takes advantage of the penetrative capabilities of neutrons to investigate the internal structures of dense, high Z materials which are difficult or impossible to measure with similar photon measurement techniques. Neutron imaging techniques can also make use of the neutron attenuating properties of hydrogen to directly image biological materials including soft tissue. These techniques are particularly useful at imaging plants due to the presence of ^{10}B, an isotope with a high neutron capture cross section, found in plant cell walls [6, 7].

Neutron imaging techniques rely on the neutral charge and magnetic characteristics of neutrons to penetrate materials or probe magnetic characteristics of a medium. Neutrons are chargeless particles carrying a spin of $\frac{1}{2}$ and an associated magnetic

moment. The lack of charge means that neutrons will not experience long range electromagnetic interactions with electrons in a material and will not experience the braking force felt by heavy ions and electrons. Neutrons carry a magnetic moment which means they can interact with unpaired electrons and non-zero spin nuclei in a material making them a valuable probe to study magnetic materials [8]. Any imaging method that relies on using particles to directly probe a sample is inherently limited by the diffraction limit of the material. If the probe wavelength is greater than the spacing between sample objects it can interact with, the resolution of the system will be diffraction limited and sample objects may be unresolvable. The wavelength and kinetic energy of a neutron are described by:

$$\lambda = \frac{h}{m_n v} \quad , \quad E = \frac{1}{2} \times m_n v^2 \tag{1.1.1}$$

Neutrons are typically categorized according to their temperature ($T = E \cdot {k_B}^{-1}$). These categories vary depending on application but in general they can be described as ultra-cold (0.00025 meV), Cold (1 meV), thermal (25 meV), and epithermal (0.5 eV $<$ E $<$ 1 keV). Neutrons above 1 keV are often referred to as *fast* due to their high kinetic energy. Most neutrons produced for imaging come from fission or spallation sources and are categorized as fast, many times with energies of several MeV. These neutrons need to be slowed down or *moderated* to increase their interaction cross section with a sample material so a room temperature medium with a high ^{1}H content such as polyethylene or water is used to slow the neutrons by elastic collisions until they reach an associated temperature of 300 K. Thermal neutrons at 300 K have $E = 25.85$ meV, $v = 2224\ m \cdot s^{-1}$ and $\lambda = 1.8$ Å. This wavelength is small enough to probe interatomic spacing and penetrate deeply into materials.

In addition to the scientific and industrial applications, there is growing interest in neutrons as a probe in border security. The International Atomic Energy Agency (IAEA) has tracked an increasing number of incidents involving the illicit trafficking of special nuclear materials (SNM) and other controlled radioactive substances [9] and there is a demand for security systems which can reliably detect these materials [10]. Border security checks require rapid and cost-effective screening of large objects such as luggage, vehicles, and shipping containers. There are however three major issues that are making the design and implementation of large area neutron imaging systems; these are the implementation of high intensity neutron sources, and the cost and acquisition of the neutron sensitive material.

In response to this demand there has been a flurry of development in neutron detection and imaging systems [10]. Systems designed to address this demand are typically passive detection systems that do not require a neutron beam source. These can take the form of radiation portal monitors (RPMs) which usually are ^{3}He proportional counters [11]. These detectors are often embedded in moderating material such as high density polyethylene to moderate neutrons to an energy region with higher neutron absorption cross section. This design is known as a bonner sphere and is a common RPM [12]. The standard neutron sensitive material in modern detection systems is ^{3}He. Since He is a lightweight gas, natural sources of He quickly leak into space. Terrestrial production of ^{3}He is primarily through beta decay of ^{3}H, an important component of nuclear weapons making its production and sales strictly controlled. This supply limitation, and the high demand from the border security and neutron detection industries, have combined to create a worldwide shortage of the isotope [13].

RPMs can detect elevated levels of neutron radiation in the environment but are not able to pinpoint their source. An imaging system sensitive to neutrons can be used to pinpoint the location of neutron sources (a passive system) or construct an image from an attenuated beam of neutrons (an active system). Many novel individual pixel readout neutron imaging systems have been proposed based on solid-state or liquid scintillator converters. ^{6}Li based scintillation systems have been combined with high performance charge-coupled device (CCD) [14] and silicon photomultiplier (SiPM) [15] devices to produce high resolution (μm scale) neutron imaging systems which have been very successful in small-scale applications able to reach detection efficiency rivaling ^{3}He devices ($\sim 65\%$) [14]. A major hurdle in designing and deploying similar imaging systems is the extremely high monetary and computational cost of scaling individual pixel readout detectors to large areas. While μm scale CCD and SiPM devices perform very well, they are very expensive and each individual pixel requires its own pulse processing chain. When scaled to a large area system capable of screening an object such as a vehicle or shipping container, the cost and computational difficulty become enormous. The high image resolution these systems are capable of are ultimately unnecessary at these larger length scales. The goal of security applications is to locate neutron sources in large containers which does not require μm scale resolution, making these devices an over-engineered solution.

There have been attempts to address the high cost of scaling an imaging system with localization detectors that use neutron scattering interactions to detect fast neutrons. The security industry has seen the development of liquid scintillator based detection systems for used in fixed installations and field deployment [16]. A 0.9x0.4 m^2 battery operable device, it uses the EJ-309 fast neutron sensitive liquid scintillator

to localize neutron sources although the resolution is too low to be considered true imaging. However, because the system is sensitive to fast neutrons, it is able to differentiate between neutron sources according to their neutron kinetic energy. Each detection cell of this system is 9 square inches which is much easier to scale to large areas. This is a promising avenue of development but its resolution is limited by the fact it uses a liquid scintillator instead of a solid state converter.

A solution which can address the requirements of international customs organizations would be an imaging system with a solid-state converter, it should be capable of moderate resolving capability (mm scale), and can be cost-effectively scaled to a large area system without an enormous computational load. In this thesis is described the development of a neutron imaging system which aims to meet these requirements by using a solid-state $^{10}B_4C$ converter with two large area scalable THGEM amplification stages and delay-line readout. A similar one-dimensional detection system has been developed based on the MICRO MEsh GAseous Structure (MICROMEGAS) detector [17, 18] and has used ^{10}B based converters to be adapted to a neutron imaging system [19, 20]. The MICROMEGAS system uses multiple $^{10}B_4C$ converters to achieve 20-40% thermal neutron detection efficiency [20] and a flexible nickel-plated polyimide mesh to amplify charge signals very similar to a gas electron multiplier (GEM) however like a GEM it is mechanically fragile, easily damaged by high voltage discharges, and requires specialized manufacturing. The μm scale holes in the mesh also allow for systems with excellent sub-mm resolution. A MICROMEGAS type imaging detector will likely outperform a THGEM based device for most applications but is an over-engineered solution that may not be suitable for mass production and deployment. At the cost of mechanical stability and high voltage discharge resistance the system can

achieve a resolution that is not necessary for container inspection. A THGEM based system can achieve very similar performance to GEM and MICROMEGAS systems in some metrics (20% energy resolution, 10 MHz/mm^2 counting rate, $10^4 - 10^7$ gain [21]) while remaining mechanically stable, high voltage discharge resistant, and easy to manufacture.

1.2 Neutron interactions with matter

In neutron imaging the attenuation of neutrons by a sample is of primary concern. A beam becomes attenuated when neutrons are absorbed by a sample or deflected away from the path of the beam. Figure 1.1 is an illustration of the attenuation of a neutron beam with fluence rate $\Phi(x)$ by a thin sample of thickness dx such that only a single interaction is possible for incoming particles. The attenuated beam exits the sample with fluence $\Phi(x + dx)$. This interaction with a target of target number density n is described by Equation (1.2.1) [22, 23].

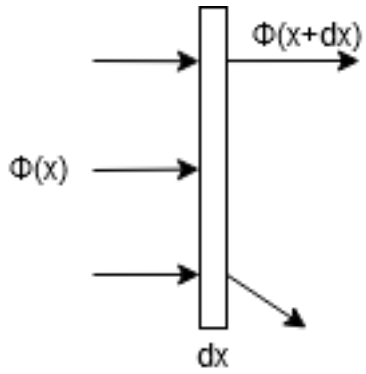

Figure 1.1: Attenuation of a beam by a thin material.

$$\begin{aligned} \Phi(x+dx) &= \phi(x)(1-dx\cdot n\sigma) \\ \frac{\Phi(x+dx)-\Phi(x)}{dx} &= -n\sigma\Phi(x) \\ \frac{d\Phi(x)}{dx} &= -n\sigma\Phi(x) \end{aligned} \tag{1.2.1}$$

In the classical description of particle attenuation, the probability of an interaction is described by its reaction cross section σ. This can be thought of as the characteristic area of a *target* the neutron would have to hit for there to be an interaction. The differential form of the attenuation equation for a thin material of thickness dx is seen in Equation (1.2.1) and its solution is seen in Equation (1.2.2).

$$\Phi(x) = \Phi_0 e^{-n\sigma x} \tag{1.2.2}$$

Real samples containing multiple elements and isotopes are actually composed of many different potential targets with number densities and reaction cross sections n_i and σ_i so for an actual sample the sum of contributions from each target species is needed. The sum of $n_i\sigma_i$ products for all target species is the linear attenuation coefficient μ_t and the associated attenuation equation becomes Equation (1.2.3). In a neutron image, the gray value of the image is proportional to the absorption and scattering of neutrons by the sample. From the gray value we can extract information on the linear attenuation coefficient to identify properties of the material such as density or isotopic identity.

$$\begin{aligned} \mu_t &= \sum_i n_i\sigma_i \\ \Phi(x) &= \Phi_0 e^{-\mu_t x} \end{aligned} \tag{1.2.3}$$

The majority of interactions between neutrons and a material are either absorption events (also called neutron capture events) or elastic scattering events. Because thermal neutrons have low kinetic energy (E = 25 meV) they are unable to excite internal degrees of freedom of a target nucleus making inelastic scattering impossible. However when fast neutrons are being moderated by a material they may undergo a stage of moderation by inelastic scattering by a dense material like Fe or Pb before they are moderated to room temperature by elastic scattering. In neutron imaging it is required that a neutron be converted into a particle that can interact with a detection medium.

1.3 Neutron converters

Neutron detection systems typically rely on nuclear interactions producing prompt charged energetic particles. Materials with such interactions are termed *converters* in this context. Neutron converters are typically discussed in terms of epithermal or fast neutron converters, which are converters that are effective above the *cadmium cutoff* of 0.5 eV neutron kinetic energy, and slow neutron converters which are effective below the cutoff. Typically, slow neutron converters are optimized to convert thermal neutrons (neutrons in thermal equilibrium with their environment) which have an average kinetic energy of 25 meV for a room temperature environment. Slow neutron converters are typically the most effective for imaging and environment monitoring due to the high neutron interaction cross sections in the slow neutron region so this discussion will focus on these. Isotopes typically used for thermal neutron conversion are seen in Table 1.1. Fissile isotopes such as ^{233}U and ^{235}U are sometimes used as neutron converters because of the high Q value of fission ($\sim$ 200 MeV) [24] but are

often undesirable because they are natural emitters of heavy ionizing alpha radiation.

Table 1.1: Common thermal neutron converters and their associated capture reactions [25, 23].

isotope	interaction	Q (MeV)	σ (barns)	relevant product
^{157}Gd	^{157}Gd(n,γ)^{158}Gd	7.9	255000	internal conversion e$^-$
^{113}Cd	^{113}Cd(n,γ)^{114}Cd	5.9	20000	internal conversion e$^-$
^{3}He	$^{3}_{2}$He(n,p)$^{3}_{1}$H	0.764	5330	heavy ions
^{10}B	$^{10}_{5}$B(n,α)$^{7}_{3}$Li (6%) $^{10}_{5}$B(n,α)$^{7}_{3}$Li* (94%)	2.792 2.310	3840	heavy ions
^{6}Li	$^{6}_{3}$Li(n,α)$^{3}_{1}$H	4.78	940	heavy ions

^{157}Gd has the highest neutron capture cross section of all isotopes but it only makes up 15.7% of the abundance of elemental Gd. The majority of the Q value of Gd neutron capture is carried away by prompt gammas which are weakly ionizing and only a small percentage ($\sim 0.8\%$) of capture reactions produce more strongly ionizing internal conversion electrons [26]. Gd is most commonly seen in neutron conversion screens used to expose radiographic film for neutron radiography. Prompt gammas have a low interaction probability with the film so the image development relies on internal conversion electrons. This is acceptable in radiography because long exposure times compensate for the low detection efficiency [22]. ^{113}Cd is similar to ^{157}Gd in that its capture Q value is emitted primarily in the form of prompt gammas and internal conversion electrons but its lower Q value and capture cross section typically make Gd the preferred choice of the two.

^{3}He is the standard fill gas for neutron sensitive proportional counters used in environment monitoring and dosimetry due to its high cross section. The only other existing gaseous compound that uses a converter seen in Table 1.1 is BF_3. Of the two, ^{3}He has a higher cross section and superior conversion efficiency. A 2 cm path length through 1 atm ^{3}He has a thermal neutron conversion efficiency of 25% and increases

to 76% at 5 atm [23]. As discussed in the previous section however the rising cost of ^{3}He has made it an undesirable choice as a fill gas. BF_3 has been investigated as an alternative to ^{3}He and has shown to be effective despite the lower cross section [27] however BF_3 detectors must be operated at higher voltages. BF_3 detectors must be operated at higher pressure to reach the same efficiency as a ^{3}He detector but this introduces health concerns in case of worker exposure because BF_3 is toxic.

As an alternative to neutron sensitive fill gases is the so-called boron-lined proportional counter which uses ^{10}B to convert neutrons to heavy ions to ionize a conventional fill gas. Because the product ions must be able to escape the solid surface of the conversion layer, the efficiency of a single layer is limited [28]. The product escape efficiency of a single ^{10}B layer is typically under 4% [23], low compared to the alternatives discussed so far. This loss of efficiency may be offset by using detector surfaces with grooves onto which boron is deposited. This increases the contact area between converter and fill gas and has been shown to improve the escape efficiency of the layer by as much as 40% over a planar converter (for neutron wavelength 4.7 Å) [29]. Multi-bladed ^{10}B detection systems which use multiple converter layers have also seen success with 65% efficiency using nine microlayers [30].

There is no Li containing fill gas that can act as an alternative to ^{3}He. The ^{6}Li neutron capture reaction has a higher Q value than the ^{10}B capture reaction but this is offset by its smaller cross section. Enriched ^{6}Li compounds are often avoided in solid state detector designs because ^{6}Li is heavily regulated. When ^{6}Li is bombarded with neutrons it produces tritium, an extremely rare isotope of hydrogen and an important component of a hydrogen bomb. Both ^{10}B and ^{6}Li thermal neutron capture reactions have heavy ion products so the higher efficiency of ^{10}B based neutron converters makes

them preferred for most solid state applications. Where ^{6}Li typically outperforms the alternatives is as a component in neutron scintillators. LiI is chemically similar to NaI and is a passable scintillator (35% light output of NaI) when mixed with a small amount (0.1 atomic %) of europium [23]. A common and commercially available neutron scintillator combines LiF compound dispersed in ZnS(Ag). A sub-mm thick scintillating layer of LiF/ZnS(Ag) can typically achieve thermal neutron detection efficiency of 25-30% and is the preferred converter for many high resolution digital imaging systems [31] although some advanced modern instruments use isotopically enriched $^{157}Gd_2O_2S$:Tb scintillators [32] to achieve very high resolutions on the order of 10s of μm.

In imaging applications, it is very important to have a thin converter. If the conversion of an attenuated beam takes places over a thick converter such as gas filled cavity, any resulting image would be smeared so a dense solid state converter is preferred. Of the common converter materials discussed here, the options for solid converters include ^{10}B compounds, ^{6}LiF, Gd, and Cd. Gd and Cd neutron capture reactions produce weakly ionizing radiation and are not ideal for a THGEM based amplification scheme. Neutron scintillators will also produce weakly ionizing electrons when paired with a photocathode so are not preferred. The introduction of a photocathode also results in further loss of efficiency. Enriched ^{6}Li compounds are heavily regulated so are not preferred to work with despite the higher Q value of its capture reaction. $^{10}B_4C$ is not subject to similar regulations and produces heavy ionizing radiation via its ^{10}B in the form of energetic alpha and lithium ions. $^{10}B_4C$ is the converter which is easiest to acquire while producing energetic heavily ionizing products ideal for a proportional counter so it was selected as the converter for this

project.

1.4 Neutron imaging technology

1.4.1 Neutron radiography

Neutron imaging was developed as a novel technique in the late 1930s and 1940s and similar to contemporary photography relied on exposing radiographical film to produce an image. This is an analog technique which requires converter and film cartridges and is relatively labour intensive compared to many modern digital imaging systems. A schematic of a typical radiography setup is seen in Figure 1.2. Neutrons are highly attenuated by ^{1}H so they are often used to image systems containing hydrocarbons or water, an example of this is seen in Figure 1.3. Taking advantage of the boron in plant cell walls, radiography can be used to study plant water transport systems [33].

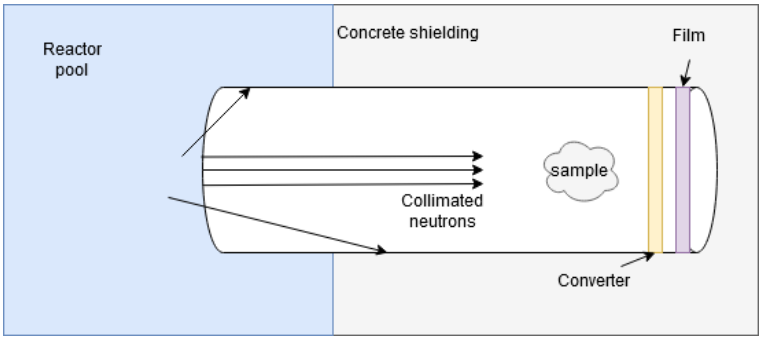

Figure 1.2: Schematic of a typical neutron radiography setup using a reactor source.

Radiography is a high resolution neutron imaging technique very similar to X-ray radiography. Radiography is the favoured neutron imaging technique for use in industry. In fields such as aviation that have very high safety standards it is

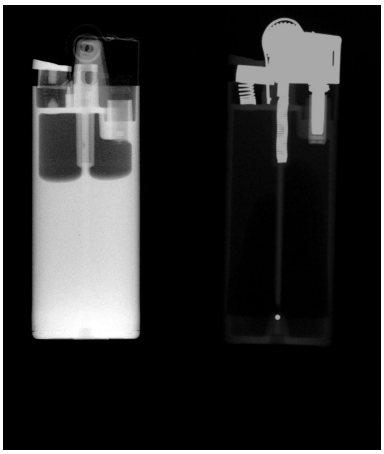

Figure 1.3: A butane lighter imaged with neutrons (left) and X-rays (right). In the neutron image the butane level can be measured. This is impossible in the X-ray image. Copyright Nray Services Inc., used with permission.

necessary to be able to inspect the interior of components that might cause an extreme hazard if they fail. Figure 1.4 is an example of the inspection of a turbine blade for manufacturing defects, a task which cannot be met by X-ray imaging due to the high density of the component materials.

Neutron imaging is a technique with a long history of use by industry (radiography) as well as in research (as part of the larger field of neutron physics). Each group has their preferred language. Typically in research the term fluence rate is used to describe the rate area density of neutrons at a given position but in industry the term flux is favoured for this same property. Here the terms fluence and fluence rate will continue to be used to remain consistent with other chapters in this document. However in other literature the term flux may be used interchangeably.

In order to make use of neutrons for analog radiography or digital neutron imaging it's required that a reliable neutron source be secured. There are three categories of neutron sources: accelerator, radioisotope and reactor. Accelerator based sources

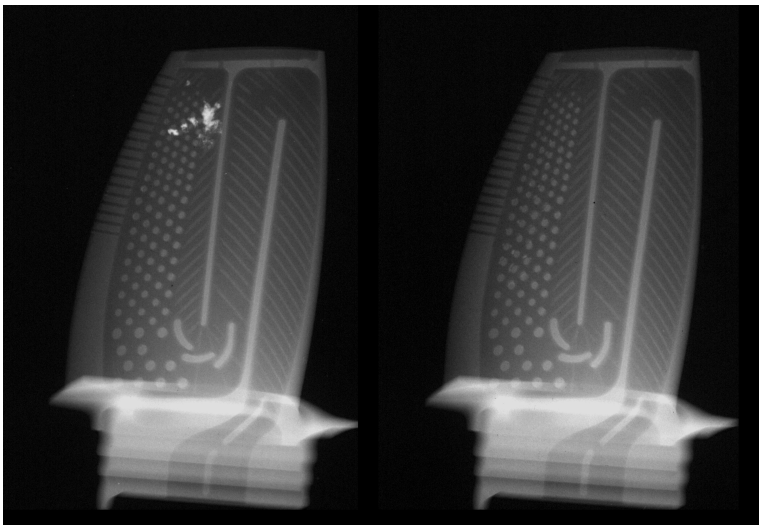

Figure 1.4: Neutron radiograph of a turbine blade demonstrating the ability to pinpoint the presence of a manufacturing flaw seen in the left image. Copyright Nray Services Inc., used with permission.

accelerate a beam of particles like alphas or protons to a spallation target such as depleted uranium, tungsten or mercury to produce an intense fluence rate of neutrons as high as 10^{14} $\mathrm{n \cdot cm^{-2} \cdot s^{-1}}$ [22]. At a modern spallation facility such as ICON facility at the Paul Scherrer Institut (PSI) the typical flux at the sample stage is 10^{7} $\mathrm{n \cdot cm^{-2} \cdot s^{-1}}$ [34]. Spallation sources are powerful but are not portable and are typically found at national laboratories such as the Spallation Neutron Source at Oak Ridge National Laboratory or PSI. Radioisotope based sources have the benefit of being easy to use and portable at the cost of fluence rate which can range from $10^{5} - 10^{9}$ $\mathrm{n \cdot cm^{-2} \cdot s^{-1}}$. Because of their low fluence rate relative to spallation and reactor sources, radioisotope sources are not normally used for imaging. An example of an isotopic source is a ^{241}AmBe source which takes advantage of the alpha decay of ^{241}Am and the $^{9}\mathrm{Be}(\alpha, \mathrm{n})^{12}\mathrm{C}$ reaction to produce fast neutrons. In order to use neutrons from either of these sources for imaging they need to be moderated

with a high hydrogen content medium such as water or polyethylene to thermal energies. The third neutron source is a reactor based source such as the MNR. Research reactors like the MNR can produce neutron fields with a fluence rate of 10^{15} n $\cdot$ cm^{-2} $\cdot$ s^{-1} or more and have the additional benefit of built-in moderation by the reactor core moderator. At the MNR imaging beam ports the typical fluence rate at the sample stage is 10^{6} n $\cdot$ cm^{-2} $\cdot$ s^{-1}. Research reactors are the favoured source for neutron radiography due to ease of construction of beam ports, built-in neutron moderation, and accessibility. At a research reactor, a neutron imaging beamline can be constructed simply by installing a beam port into the pool to the sample stage with a fast neutron filter such as a single-crystal filter.

Modern radiographical systems do not rely on pixel readouts so are able to produce very high resolution images on the order 1 μm and for such applications where this resolution is desired, radiography is still the favoured imaging mode today. In a typical radiography setup a neutron source is collimated by a neutron and gamma absorbing medium; directing unidirectional neutrons towards a sample set in front of a cartridge containing a neutron conversion medium and radiographical film. Typically in radiography the converter material is a vapour deposited film of Gd. ^{157}Gd capture produces a spectrum of gamma rays and conversion electrons. The capture cross section of ^{157}Gd does not exhibit a $\frac{1}{v}$ dependence like ^{6}Li, ^{3}H, and ^{10}B converters do. This preferential interaction with thermal neutrons makes Gd useful in wide-spectrum imaging beamlines as it will suppress the fast and epithermal neutron background [22]. Internal conversion electrons from Gd neutron capture expose the radiographic film which must be developed and analyzed afterwards. An indirect form of radiography is also possible in the case that a sample can itself become activated by neutrons. In

such a case a sample is activated by a neutron source and placed in front of a film cartridge. The film gray value carries information on the radioactivity of the sample which is proportional to its neutron absorption.

1.4.2 Digital and gaseous neutron imaging

High performance CCD devices are capable of producing high resolution imaging systems comparable to radiography but are able to collect and read out images at a far greater rate. They have the additional benefit of being reusable. Radiographic film has a low collection efficiency necessitating a high intensity source like a research reactor or a spallation source. Digital systems based on CCD and similar technologies have a higher collection efficiency so are better suited to imaging with low intensity sources. A digital neutron imaging system can be designed such that a conventional CCD based digital camera can collect the image. Instead of a converter and film, a neutron scintillator like ^{6}LiF/ZnS or Gd_2O_2S:Tb is used to produce scintillation photons. A mirror is used to direct scintillation light away from the path of the beam towards a focusing lens and camera; the camera is kept out of the path of the beam to protect it from radiation damage. A schematic of a typical CCD based digital imaging system based on neutron scintillation is seen in Figure 1.5. An example of such a system is the neutron microscope system at the Paul Scherrer Institute in Villigen, Switzerland [32]. Such systems making use of high performance, cooled CCDs can achieve high resolutions comparable to radiography. The goal of the neutron microscopy project is to produce a system with a resolution of 5 μm. One downside to such a system is the cost to scale to large areas. A high performance CCD device is very expensive on the order of hundreds of dollars per square cm. The cost to scale

up an individual pixel readout CCD system to a large area system capable of imaging objects like shipping containers and vehicles would be extreme.

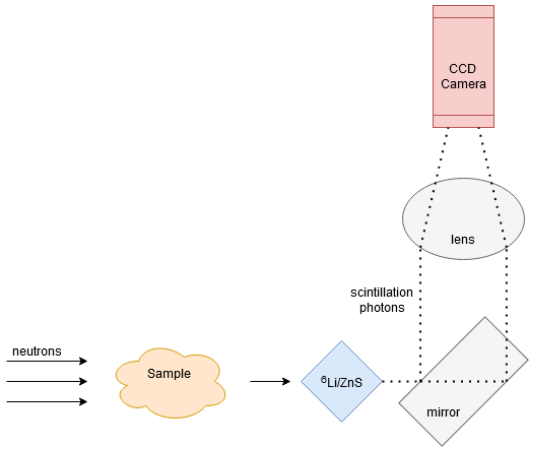

Figure 1.5: Schematic of a digital neutron imaging system based on a ^{6}Li/ZnS neutron scintillator and cooled CCD camera.

It is possible to design a gaseous neutron imaging system but a major challenge in any design is the long range of charged particles in a gaseous medium. Using a neutron sensitive fill gas is not desired because of to its low density, such a system would produce a smeared image as the proton tracks will originate throughout the volume of gas. Typically a solid state converter like ^{6}Li or ^{10}B is used in combination with a conventional fill gas. It is difficult for a gaseous system to compete with a scintillation based system because of the long ion range in gas, usually several centimetres at atmospheric pressure. The most successful such system is Micromegas, a parallel plate system which uses a solid state converter and micromesh cathode permeable to free charges that has achieved a neutron resolution of 400 μm [18]. This system is scalable to large areas but its readout is one-dimensional.

1.5 Instrument operation

The instrument is a gaseous neutron imaging system that uses a solid state $^{10}B_4C$ neutron converter, a two stage THGEM charge amplification stage with P10 fill gas, and a 2D passive delay line readout. A schematic of the instrument operation is seen in Figure 1.6.

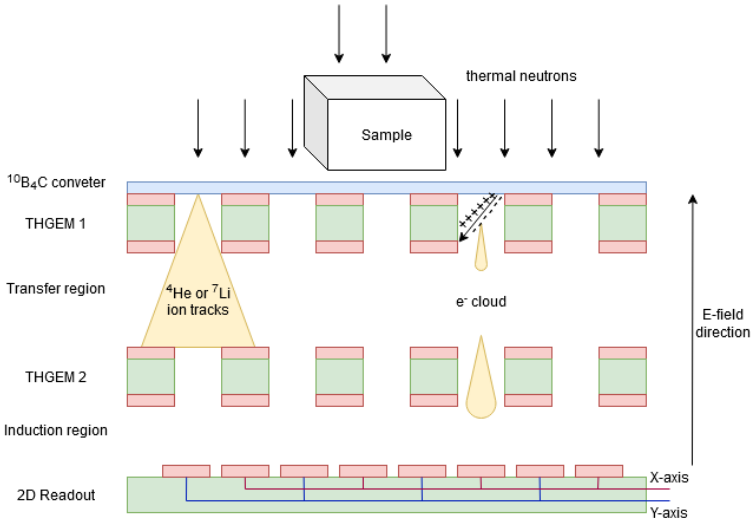

Figure 1.6: Schematic of detector operation.

$$\begin{aligned} n + {}^{10}B &\rightarrow {}^4He^{2+} + {}^7Li^{3+} + 2.79\ \text{MeV}\ (6\%) \\ n + {}^{10}B &\rightarrow {}^4He^{2+} + {}^7Li^{3+} + 2.31\ \text{MeV} + \gamma(0.48\ \text{MeV})\ (94\%) \end{aligned} \tag{1.5.1}$$

An attenuated beam of thermal neutrons strikes a $^{10}B_4C$ microlayer converter. The neutron capture reaction has two modes as described by Equation (1.5.1). The thermal neutrons carry a very small amount of momentum relative to the momentum of the individual reaction products. The total momentum of the thermal neutron/^{10}B

pair is very small compared to the combined momentum of the interaction product pair which means the ion product momentum values may be treated as if they sum to zero which requires the products to be emitted in opposite directions with an isotropic angular distribution. This reaction property means that either the alpha or the Li will be directed towards THGEM 1 but never both for a single reaction. Gamma reaction products also have an isotropic angular distribution but have a lower ionization density than the ion products and may produce free charge pairs far from the surface of the converter. For this reason, gamma products will produce a low level background fog in the image if they are not discriminated against. Selection of a gamma insensitive fill gas can mitigate this effect. Capture product ions will liberate electron-ion pairs in the holes of the THGEMs and the transfer region. The total charge is amplified inside the THGEM holes via Townsend avalanches and the resulting charge cloud induces a charge on an array of diamond shaped copper pads attached to passive axis delay lines. Each delay line cell introduces a 1.5 ns delay to the signal such that the time difference between output signals at either end of the delay line encodes the position of the originating pad along that axis.

1.5.1 Converter thickness

The detector is operated in a forward transmission configuration in which incoming neutrons strike the converter and detected reaction products exit the microlayer surface in the forward direction of the beam. If the ion product originates at a converter layer depth greater than their range it is unable to escape the surface. This means there must be an ideal converter layer thickness that maximizes conversion efficiency and minimizes the number of ion products that are stopped by the converter. To

determine this thickness the transmission configuration was simulated in GEANT4 [35]. These results were compared with an analytical model based on empirical data collected from literature. This analytical model is described here. The transmission configuration is depicted in Figure 1.7.

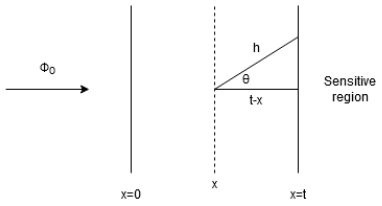

Figure 1.7: Schematic of transmission neutron converter.

A monoenergetic neutron beam with fluence Φ_0 is converted to ion products inside a converter layer of thickness t at depth $t-x$ from the surface in contact with a gaseous sensitive region. Since the $^{10}\mathrm{B}(\mathrm{n},\alpha)^{7}\mathrm{Li}$ reaction is isotropic and the products travel in opposite directions it is known that for every capture event, one product will be directed into a solid angle towards the sensitive region with the exception of perfectly vertical trajectories. Capture products have trajectories into the solid angle Ω.

$$\Omega(x) = \int_0^{2\pi} \int_0^{\theta_{max}} \sin\theta \;\, \mathrm{d}\theta \, \mathrm{d}\phi \tag{1.5.2}$$

The maximum escape trajectory angle $\theta_{\max}$ from the layer depth and product range in the converter material R can be calculated.

$$\begin{aligned} \cos\theta &= \frac{t-x}{h} \\ \theta_{max} &= \arccos\frac{t-x}{R} \end{aligned} \tag{1.5.3}$$

For an isotropic reaction, the fraction of particles that can escape is $F(x)$. This term includes an additional factor of 2 to account for the two possible ion species in the

^{10}B capture reaction. A factor of 2 is selected for simplicity, because the range of the two ion products differs, its true value is between 1 and 2.

$$\begin{aligned} F(x) &= \frac{\Omega(x)}{4\pi} \cdot 2 \\ &= \frac{1}{2\pi} \int_0^{2\pi} \int_0^{\theta_{max}} \sin\theta \ \mathrm{d}\theta \, \mathrm{d}\phi \\ &= (1 - \frac{t-x}{R}) \qquad\qquad t - x \leq R \\ &= 0 \qquad\qquad\qquad\qquad \text{otherwise} \end{aligned} \tag{1.5.4}$$

The neutron beam will be attenuated by the converter material according to its total attenuation coefficient μ which is the sum of its capture and scattering coefficients μ_c and μ_s.

$$\begin{aligned} \Phi(x) &= \Phi_0 e^{-\mu x} \\ \mu &= \mu_c + \mu_s \end{aligned} \tag{1.5.5}$$

By differentiating the fluence $\Phi(x)$, the change in fluence at depth x is calculated which is equivalent to the interaction rate density or the rate of capture events within some area at depth x. The neutron capture cross section for our converter is much larger than its scattering cross section for a monoenergetic beam of thermal neutrons so the simplification to neglect scattering is made. The interaction rate density is then the neutron capture rate density $\frac{\mathrm{d}N_c}{\mathrm{d}t}$.

$$\frac{\mathrm{d}N_c}{\mathrm{d}t} = \Phi_0 \mu_c e^{-\mu x} \ \mathrm{d}x \tag{1.5.6}$$

Now the escape fraction (Equation (1.5.4)) can be multiplied by the neutron capture rate density (Equation (1.5.6)) to calculate the differential escape rate density. For

the case of $t < R$:

$$\begin{aligned} &\text{Case} : t < R \\ &F(x) \cdot \frac{\mathrm{d}N_c}{\mathrm{d}t} = (1 - \frac{t-x}{R})\Phi_0 \mu_c e^{-\mu x}\, \mathrm{d}x \quad 0 \le t - x \le R \\ &\qquad = 0 \qquad\qquad\qquad\qquad\qquad\qquad\qquad\qquad \text{otherwise} \end{aligned} \tag{1.5.7}$$

For the case of $t > R$, the modification $\Phi_0 \rightarrow \Phi_0 e^{-\mu(t-R)}$ is made.

$$\begin{aligned} &\text{Case} : t > R \\ &F(x) \cdot \frac{\mathrm{d}N_c}{\mathrm{d}t} = (1 - \frac{t-x}{R})\Phi_0 \mu_c e^{-\mu(t-x-R)}\, \mathrm{d}x \quad 0 \le t - x \le R \\ &\qquad = 0 \qquad\qquad\qquad\qquad\qquad\qquad\qquad\qquad \text{otherwise} \end{aligned} \tag{1.5.8}$$

The escape efficiency ϵ_{R_i} for an ion of range R_i is then the differential escape rate normalized by Φ_0 and integrated.

$$\begin{aligned} \epsilon_{R_i} &= \frac{1}{\Phi_0}\int_{t-R_i}^{t} (1 - \frac{t-x}{R_i})\Phi_0 \mu_c e^{-\mu(t-x-R_i)}\, \mathrm{d}x \qquad t > R_i \\ &= \frac{\mu_c}{\mu^2 R_i} e^{-\mu(2t-R_i)}(e^{\mu R_i} - \mu R_i - 1) \qquad\qquad t > R_i \\ &\qquad\qquad\qquad\qquad\qquad\qquad\qquad\qquad\qquad\qquad\qquad\qquad (1.5.9) \\ &= \frac{1}{\Phi_0}\int_{t-R_i}^{t} (1 - \frac{t-x}{R_i})\Phi_0 \mu_c e^{-\mu x}\, \mathrm{d}x \qquad\qquad t \le R_i \\ &= \frac{\mu_c}{\mu^2 R_i} e^{-\mu t}(e^{\mu t}(\mu R - \mu t + 1) - 1 - \mu R) \qquad t \le R_i \end{aligned}$$

The total escape efficiency ϵ_{tot} is calculated by taking the weighted sum of escape efficiency for the four possible ion ranges. These ranges for product ions in B_4C were calculated using SRIM 2013 [36] and are summarized in Table 1.2.

Table 1.2: Summary of ^{10}B neutron capture ion product ranges in B_4C [36].

Ion (kinetic energy)	Range (μm)	Ion (kinetic energy)	Range (μm)
^{4}He (1.78 MeV)	R_1=4.12	^{4}He (1.47 MeV)	R_3=3.34
^{7}Li (1.01 MeV)	R_2=1.90	^{7}Li (0.84 MeV)	R_4=1.69

$$\epsilon_{tot} = 0.06(\frac{1}{2}(\epsilon_{R_1} + \epsilon_{R_2})) + 0.94(\frac{1}{2}(\epsilon_{R_3} + \epsilon_{R_4})) \tag{1.5.10}$$

Using the ($\lambda = 2$ Å) neutron attenuation coefficients for ^{10}B, ^{11}B, and ^{nat}C [37] the total escape efficiency is calculated and plotted against layer thickness. These results for converter materials $^{10}B_4C$ and $^{nat}B_4C$ are compared with GEANT4 simulation results in Figure 1.8. As expected the ^{10}B enriched converter material exhibits superior escape efficiency. The total escape efficiency peaks for the analytical model at $t = 3$ μm, $\epsilon_{tot} = 4.8\%$ and for the GEANT4 results at $t = 2.4$ μm, $\epsilon_{tot} = 4.1\%$. With assistance from Dr. Carina Höglund and collaborators at the European Spallation Source (ESS) we acquired 5x5 cm^2 $^{10}B_4C$ conversion layers 3.2 μm thick deposited on 1 mm thick Al-5754 substrate. This thickness is slightly above the peaks seen in our results but it is unlikely that the difference will be significant in our experiments.

1.5.2 Thick gas electron multipliers

The charge amplification stage is composed of a set of two cascaded THGEMs. A THGEM is a mechanically robust, high gain gaseous electron multiplier similar in structure to a typical GEM but with larger physical dimensions on the order of several hundred micrometers to millimeters. The THGEM was originally presented by Periale et al. [38] as a low cost alternative to photomultipliers and has seen significant attention in the field of radiation detector design [39, 40, 41, 42]. It

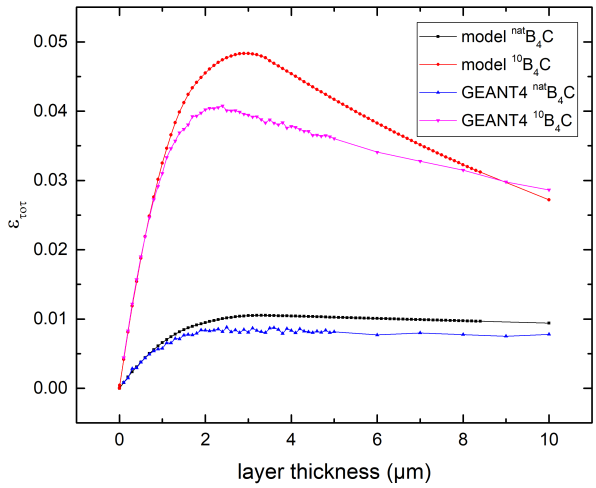

Figure 1.8: Total $^{10}B(n,\alpha)^7Li$ ion product escape efficiency from the surface of a $^{nat}B_4C$ or $^{10}B_4C$ microlayer for a neutron beam in the transmission configuration.

can be manufactured using standard PCB manufacturing techniques by drilling an array of small holes in copper clad PCB material such as FR4. Applying a high voltage across the sides of the THGEM results in a strong electric field (geater than 10 kV·cm^{-1}) capable of causing Townsend avalanches in the THGEM holes. This concept of operation is depicted in Figure 1.6. A single THGEM can achieve gain on the order of 10^4 and by adding a second THGEM the gain can be increased to 10^6 [39]. While THGEMs are capable of these high gains, they are easily damaged by high voltage discharges. By removing a small amount of material from the edge of the holes the THGEM can withstand greater biases before exhibiting discharge damage. The gain can be improved by chemically etching 0.1 mm wide rims away from the THGEM holes as seen in Figure 1.9 [39]. It is also seen that these etched rims can be inconsistent, hole-rim eccentricity will cause gain variance along the THGEM and negatively affect long term gain stability [42].

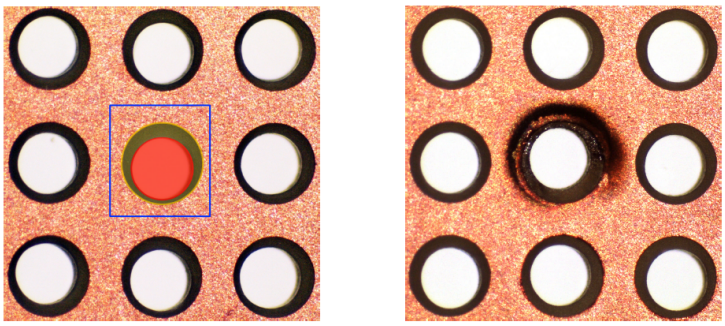

Figure 1.9: Optical image of etched rims exhibited hole-rim eccentricity (left), and holes damaged by high voltage discharges (right) [43]

While a higher signal-to-noise ratio is desired for for imaging applications as described in this work, THGEMs without etched rims are selected due to ease of manufacturing. The additional gain provided by including etched rims is found to not be necessary in this work as an adequate signal-to-noise ratio was observed following pulse amplification for the full area of the readout board. The most important property of THGEMs for imaging applications is the spatial constraint of the Townsend avalanches. Charge amplification is contained within THGEM holes and events will not trigger secondary events in neighbouring holes. This is desired for imaging applications because it means that charge amplification will not broaden image features and worsen resolution.

The electron cloud exiting the bottom of the THGEM has a radial distribution that will broaden as it travels away from the hole exit. The resolution of any imaging system based on THGEMs will highly depend on the transverse diffusion of this cloud. Ray et al. used ANSYS and Garfield++ simulations to study this diffusion [44]. It was found that for 200 μm diameter holes, and a 1 mm wide drift gap, the broadening of the resolution has $\sigma = 170$ μm and that the full width of the electron cloud is less than 1 mm. Provided the pad pitch of the readout is greater than the

expected resolution broadening it is not expected that this transverse diffusion will have a significant effect on the resolution.

1.5.3 2D passive delay line readout

The 2D anode readout is based on lumped parameter passive delay lines rather than individual pixel readout. Using a delay line, the origin pixel of a signal can be deduced from the difference in signal arrival time between either end of the line. This drastically reduces costs associated with individual pixel pulse processing allowing such a system to be more easily scaled to large areas. The readout is composed of a 2D array of diamond shaped copper pads connected to an X and Y axis delay line via internal PCB layer traces as seen in Figure 1.6. An image of a 32 cell readout is seen in Figure 1.10.

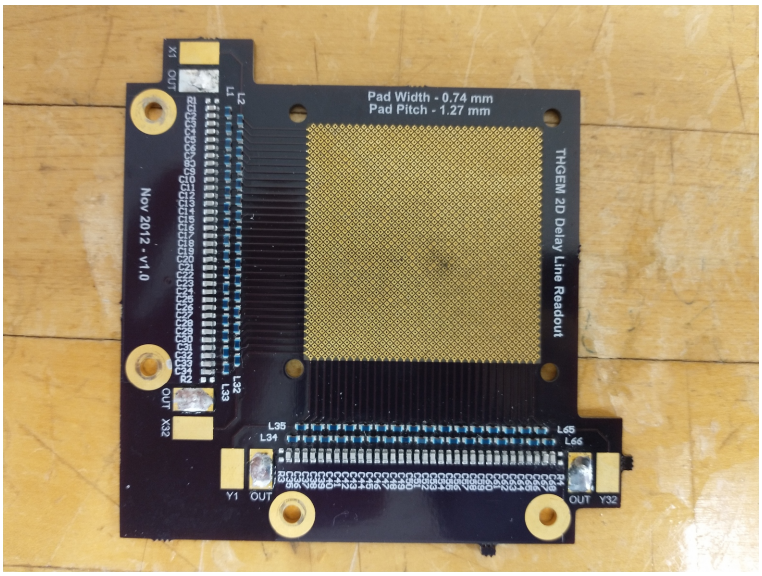

Figure 1.10: Image of 32 cell delay line readout. Pads have width 0.74 mm and pitch 1.27 mm.

Charge clouds exiting the bottom of THGEM 2 induce a current signal in the

spatially corresponding readout pads. This signal travels down the interior traces to the delay lines where each cell delays the signal by a length of time t_d. A delay line cell is a type of LC circuit which delays a signal by a tunable length of time provided it has a frequency less than the cell's cutoff frequency. An electrical diagram of a delay line cell with nominal impedance Z_0, time delay t_d and cutoff frequency ω_0 is seen in Figure 1.11.

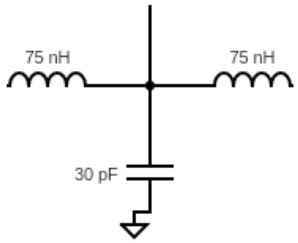

Figure 1.11: Electrical diagram of a delay line cell.

A passive lumped parameter delay line behaves as a filter which attenuates signals above its cutoff frequency.

$$\omega_0 = \frac{1}{\sqrt{LC}} \tag{1.5.11}$$

Like all real filters, its true behaviour is dependent on the signal frequency ω.

$$\begin{aligned} t_d &= \frac{1}{\omega}[\frac{\omega}{\omega_0} + \frac{1}{3}(\frac{\omega}{\omega_0})^3 + ...] \\ &\approx \sqrt{\frac{L}{C}} \qquad\qquad \omega << \omega_0 \\ &\approx \frac{1}{\omega_0} \end{aligned} \tag{1.5.12}$$

This dependence also holds true for the nominal impedance.

$$\begin{aligned} Z_0 &= \frac{\frac{L}{C}}{\sqrt{1-(\frac{\omega}{\omega_0})^2}} \\ &\approx \sqrt{\frac{L}{C}} \qquad\qquad \omega << \omega_0 \end{aligned} \tag{1.5.13}$$

The delay cell parameters need to be carefully chosen to ensure that the special case of $\omega << \omega_0$ is satisfied. In imaging applications, dependence of the delay time on the signal would negatively impact image resolution. For the work described in this document delay lines with $t_d = 1.5$ ns, are used. The circuit has $\omega_0 = 670$ MHz. The typical period of a preamplified signal from our imaging system is ~ 20 ns and has an angular frequency of $\omega = 314$ MHz. Higher order contributions to the cell delay are therefore expected to be on the order of 0.1 ns which is not considered to be significant for our application.

Chapter 2

Pulse processing and data acquisition

An early milestone of this work was to reconstruct the detector, pulse processing chain and time-to-digital converter data acquisition system (TDC-DAQ) developed by Hanu et al. [45]. A schematic of this system is depicted in Figure 2.1. The pulse processing chain is composed of commercial Ortec fast timing preamplifiers, constant fraction discriminators (CFDs), and homemade timing amplifiers. The TDC-DAQ is composed of a commercial time-to-digital converter (TDC) and field-programmable gate array (FPGA) which are responsible for measuring the arrival time of logical signals and reconstructing the image from time of flight respectively. Many components used by Hanu et al. were lost or degraded and needed to be replaced or redesigned. This chapter will discuss the modifications to the detector assembly and pulse processing chain made to compensate for obsolete and degraded components as well as adapt the detector to be sensitive to neutrons. After a brief description of the firmware implementation of the TDC-DAQ, changes will be discussed at each stage in

the pulse processing chain. Eventually it was decided that since the objective of this project is to demonstrate that this detector can be a viable neutron imaging system, the hardware implementation TDC-DAQ was deprioritized. In the interest of time the TDC-DAQ and the majority of the pulse processing was replaced by a desktop digitizer system such that image reconstruction could be performed offline utilizing timing measurements taken from the digitized analog detector signals.

2.1 Prior work

In its original design by Hanu et al., the event timing and reconstruction was implemented in hardware. The details of this design will be discussed here insofar as they pertain to their reproduction. Implementing the TDC-DAQ in hardware has several benefits over a digital solution including but not limited to increased throughput, reduced cost, reduced computational load, and ease of scalability. Digital systems, especially at a large scale may be prohibitively expensive and having to digitize the full analog signal greatly reduces system throughput.

A hardware implementation of the TDC-DAQ must perform three primary tasks: first it must extract timing information from each of the 4 axis signal channels and the trigger channel, second it must perform the image reconstruction and store the image as a histogram in memory, and third it must interface with an external device to output image data. The first task is accomplished by a PCB housing the TDC-GPX, an integrated circuit (IC) developed by Acam Messelectronic GMBH. This is a high performance TDC which processes the logical signal input from the CFDs. When configured in I-mode, the TDC-GPX will generate time stamps from the arrival of TTL signals at up to eight TSTOP channels relative to one TSTART channel. The

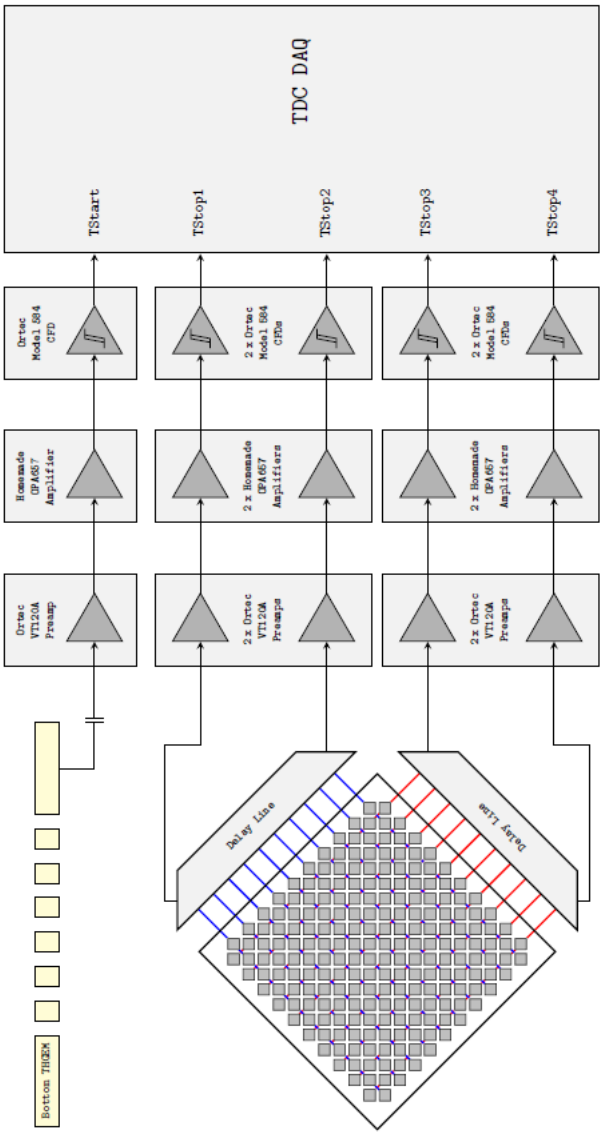

Figure 2.1: Schematic of the pulse processing chain used by the THGEM based delay line imaging system developed by Hanu et al. [45].

principle of how the TDC-GPX operates in this system is depicted in Figure 2.2. Since the logical trigger signal will always precede the arrival of axis signals in the imaging system it is used as the TSTART signal; X and Y axis logical signal arrival times are then measured relative to the trigger arrival time. The TDC-GPX has a

nominal time resolution of 81 ps in I-mode and a peak event rate of 182 MHz.

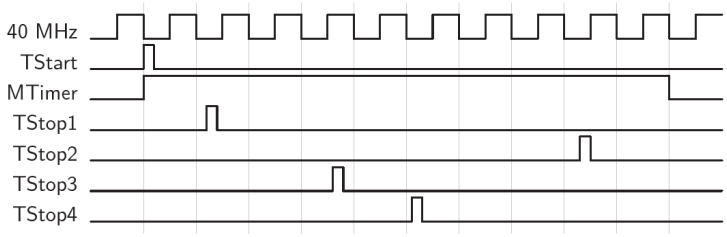

Figure 2.2: Timing diagram of a TDC-GPX operation over an MTIMER wide collection window [45].

The logical trigger output signal is fed into the TSTART channel which starts an internal timer signal called MTIMER. This timer is derived from an external 40 MHz clock and its width is the window of time over which each channel will register an input signal. A register on each input channel will increment on each clock rising edge. This counting is stopped when a logical transistor-transistor logic (TTL) pulse arrives at a TSTOP input. The counter in each channel can be multiplied by the time between clock pulses to get the timing between the arrival of the TSTART signal and the channel TSTOP signal. This information in the case of the TDC-GPX can then be accessed via two interface first in, first out (FIFO) registers. Under ideal conditions, it is expected that each of the four TSTOP channels should see one logical pulse during an acquisition cycle. The MTIMER is configured to be 250 ns wide and the TDC-GPX takes 60 ns to reset after an event. In addition to this is observed a dead time of 200 ns after four continuous measurements. This defines the throughput rate of the TDC-GPX to be 1.96 MHz [45]. The TDC-GPX is housed on a PCB along with the required external clock circuit and power supply circuits as seen in Figure 2.3.

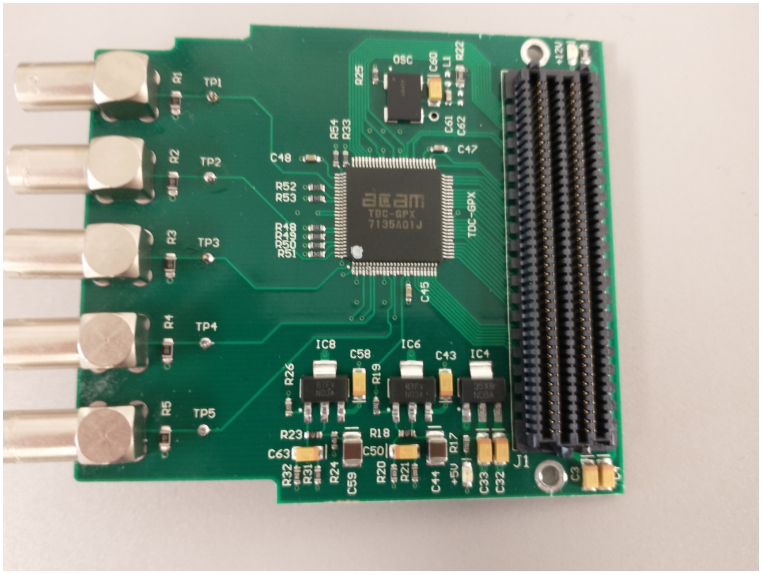

Figure 2.3: PCB housing the TDC-GPX. Resistors R1-R5 are desoldered for operation.

The timing information from the TDC-GPX must be read and processed to reconstruct the XY coordinates of the originating pixel, this information must also be stored in memory and made accessible to a user. These tasks are performed by a Spartan 6 FPGA housed on an Xilinx SP601 development board (see Figure 2.4). The SP601 interfaces with the TDC-GPX via a FPGA Mezzanine Card (FMC) low pin count (LPC) connector. The SP601 is a powerful development platform with many available peripherals but for this work the FMC, universal asynchronous receiver/transmitter (UART) interfacing connectors, and the on-board DDR2 memory are the important features. An FPGA is an array of programmable logic blocks and rewireable interconnects. It is a device which allows firmware and software developers to create, iterate, and test digital logic designs and the interconnects on the SP601 board allow interfacing of the FPGA with external resources and interfaces. These designs can be fully specified by a hardware description language (HDL) such

as VHDL or verilog. The FPGA firmware was developed by Hanu et al. [45] and a high level description of its architecture is seen in Figure 2.5.

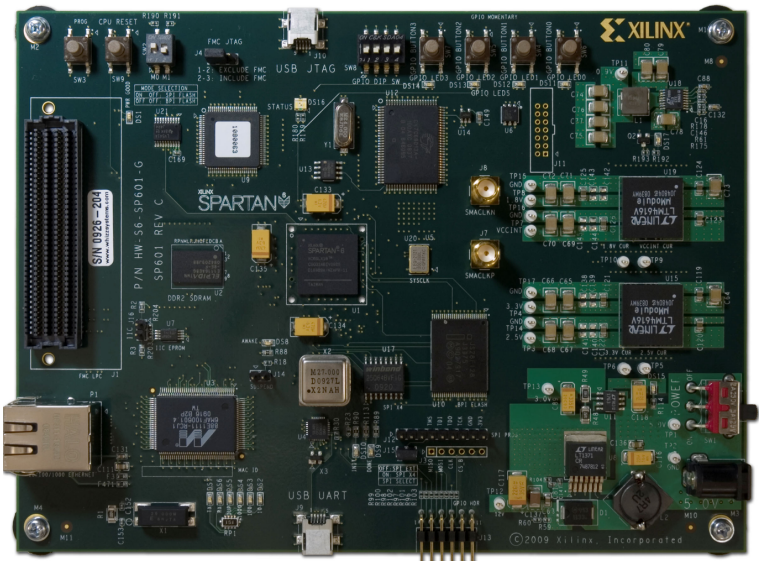

Figure 2.4: Xilinx SP601 development board featuring the Spartan 6 FPGA.

The FPGA interfaces, configures, and reads the FIFOs on the TDC-GPX using the TDC-GPX core and read-write controllers and stores the timestamps in a FIFO on the FPGA. Because the timestamps are stored in the FIFO, the TDC-GPX is freed up to measure a new set of incoming signals. This means that signal collection by the TDC-GPX and event reconstruction in the FPGA can be performed in parallel, increasing the throughput of the system. The maximum throughput rate of the TDC-DAQ is 1.8 MHz and is limited by the throughput rate of the event reconstruction in the histogramming controller. The histograms for the X and Y coordinates are defined in memory and are incremented by the histogramming controller. This memory can be accessed through a UART connection by a PC. A MATLAB software package developed by Hanu et al. [45] is used to read the memory, start data acquisition cycles, and configure the TDC-GPX. The graphical user interface (GUI) for this

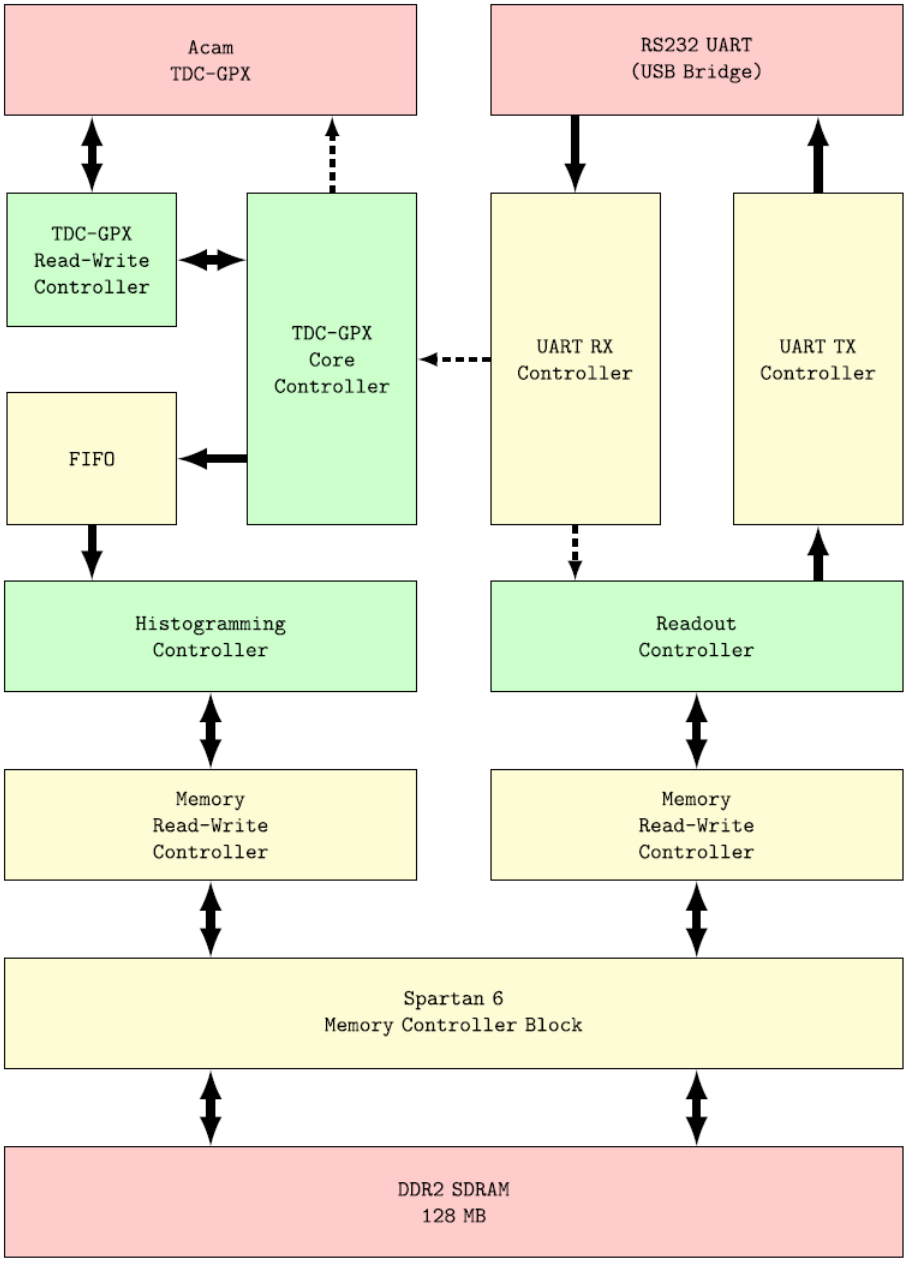

Figure 2.5: Block diagram of the firmware architecture loaded onto the FPGA. Control modules are enclosed by the dashed rectangle. Data flow and control signals are represented by solid and dashed arrows, respectively [45].

software can be seen in Figure 2.6.

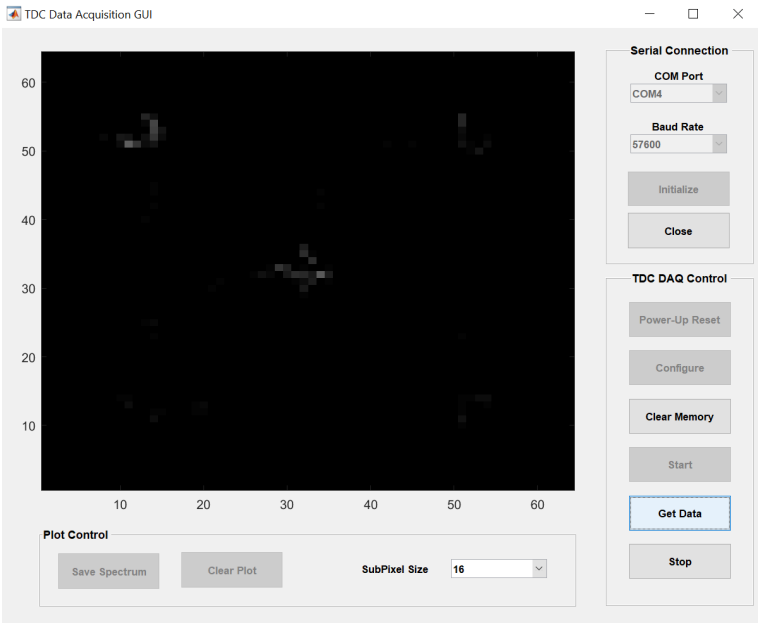

Figure 2.6: Matlab graphical user interface to control the TDC-DAQ [45].

One of the primary initial goals of this project was to rebuild the TDC-DAQ so that it could be iterated on and adapted for neutron imaging. This chapter will focus on the efforts to achieve this goal. Eventually it was decided that the firmware approach to the TDC-DAQ would be abandoned in favour of digitization.

2.2 Rebuilding the detector and DAQ

2.2.1 Detector assembly

The 2D imaging detection system can be adapted to be sensitive to photons, alphas and neutrons. Images may be collected using alphas and photons when the detector stack is assembled as seen in Figure 2.7.

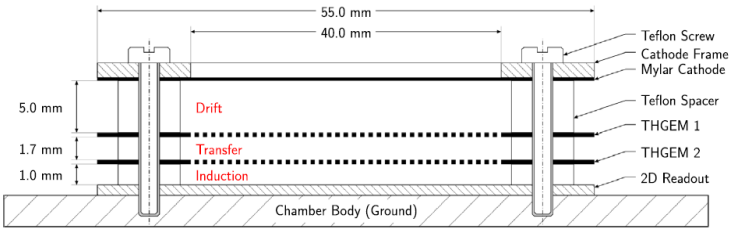

Figure 2.7: Detector stack configuration for imaging with an x-ray source. Alphas may be used by placing an alpha source just above the mylar cathode [45]. The assembly is housed in an Al-6061 chamber.

To image with neutrons a neutron conversion layer is required to produce secondary particles that can ionize a fill gas. For reasons discussed in Chapter 1, a 3.2 μm thick microlayer of enriched $^{10}B_4C$ deposited on a 1 mm thick substrate of Al-5754 was used. The microlayers were produced at the ESS by Dr. Carina Höglund and collaborators. This converter is held on a polyoxymethylene purpose built shelf (see Figure 2.8) some distance above the first THGEM. The finished assembly is seen in Figure 2.9. In this configuration the substrate is secured onto the shelf with polyimide tape, microlayer side facing the THGEMs. The top side of the Al substrate is biased to act as the drift region cathode. An alternative neutron imaging configuration is to secure the neutron conversion layer, microlayer side down, flush with the top of the first THGEM. In this alternate configuration there is no drift region and no drift field; neutron capture products exit the microlayer directly into THGEM holes or are stopped by copper. This configuration results in superior image spatial resolution and will be discussed in Chapter 4. The 2D readout PCB is fixed to an aluminum chamber base with metallic grounding screws. The assembly is secured by four flat head M3 nylon screws cut to length such that they thread into the chamber base through the holes in each component such that the flat head is below the surface of the countersunk hole in the neutron converter (see the full assembly in Figure 2.10).

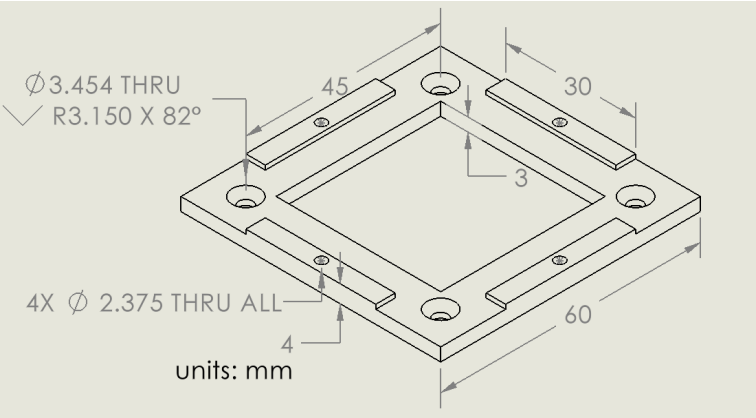

Figure 2.8: Neutron conversion layer shelf machined from polyoxymethylene. The neutron conversion layer can be secured to the shelf by the heads of screws in the holes on the raised portions or simply taped down.

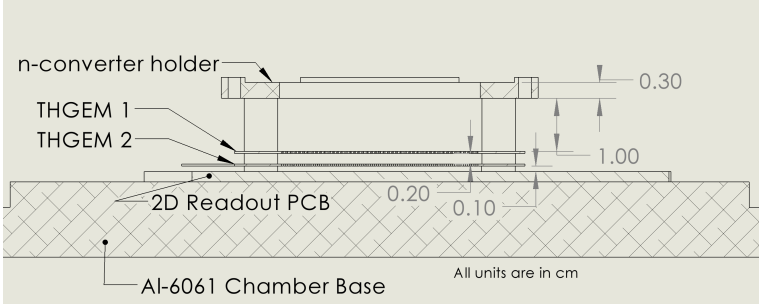

Figure 2.9: Detector stack configured to image with neutrons. The aluminum substrate of the neutron conversion layer acts as the cathode in this configuration.

2.2.2 Power supply and filtering

The anodes and cathode are biased by a CAEN four channel high voltage desktop power supply. The design of the power circuits are unchanged from Hanu [43] but the physical components were missing and needed to be rebuilt. The anode and cathode power circuits are shown in Figure 2.11.

The voltage divider PCBs used by Hanu et al. were still available but they lacked the low pass filter so new PCBs to be housed inside the detector were designed. A render of the first attempt to design this PCB is seen in Figure 2.12.

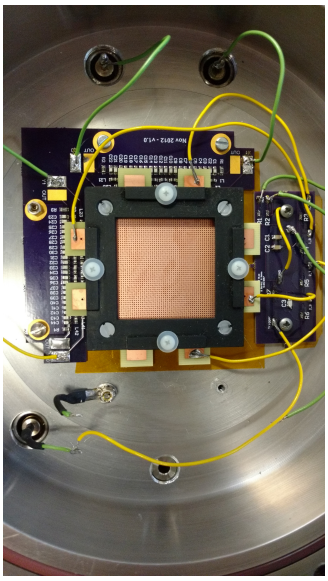

Figure 2.10: Image of 2017 version of neutron imaging assembly with drift region and version one of the HV bias circuit and THGEM. Neutron converter not present. This version of the assembly was not actually used on a neutron beamline.

Version 1 of the HV bias PCB is a single layer PCB. When attempting to bias the detector with an alpha source large voltage spikes in the preamplifier signal and audible *pinging* sounds coming from within the chamber were observed. This indicates high voltage discharges between THGEMs or the bias PCB. On inspection no evidence of spark damage was found on the THGEMs or anywhere else in the detector assembly so it was concluded the discharges must be occurring on the HV bias PCB. It is suspected that discharges may have occurred between the anode and cathode circuits on the same layer, a few more iterations of a two layer PCB were developed before arriving at version 2 seen in Figure 2.13. Larger footprints were used in this version to reduce the probability of high voltage discharges. Depending on the fill gas one may be able to use a Paschen curve to predict HV discharges but these data could not be found in the literature on tissue equivalent propane; the fill gas available

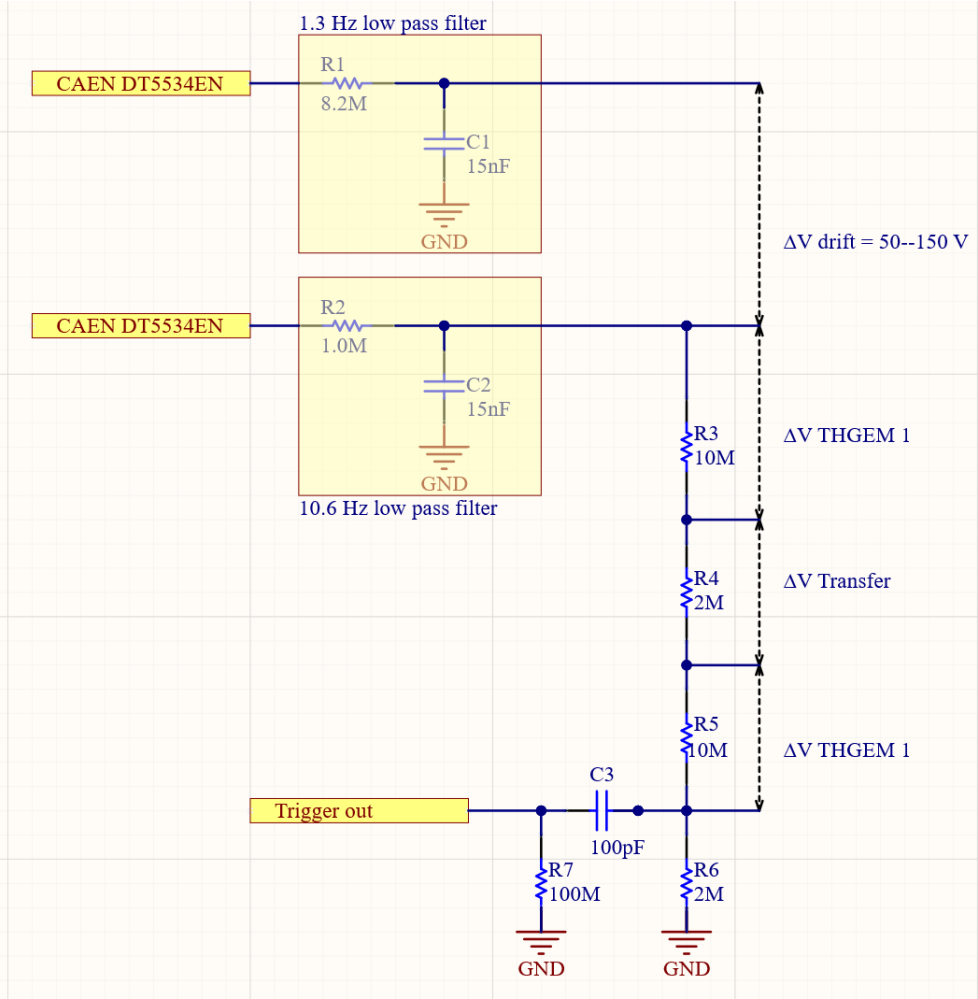

Figure 2.11: Voltage divider circuits for a two THGEM anode with cathode configuration. Low pass filters are included for each circuit to reduce signal noise originating from the power supply.

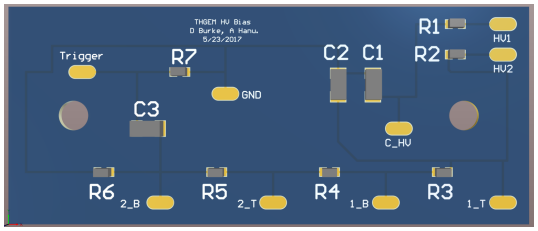

Figure 2.12: 3D render of the single layer version 1 of the HV bias PCB including low pass filters for both anode and cathode circuits.

at this point.

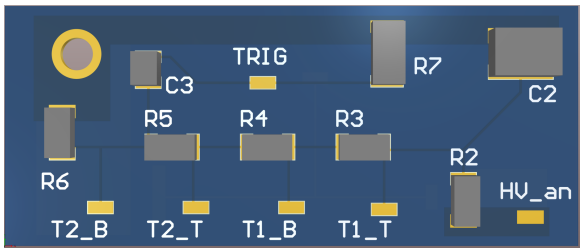

(a) Top anode layer.

(b) Bottom cathode layer.

Figure 2.13: 3D renders of top and bottom layers of the HV bias circuit version 2 including low pass filters.

Several rounds of testing with an alpha source still resulted in high voltage discharges with no visible damage to the detector assembly. In order to determine where the discharges were occurring, a new detector window was cut from 3/8 inch thick acrylic. Repeating attempts to see a signal from an alpha source, it was discovered that HV discharges were occurring across the anode low pass filter in the HV bias circuit (see Figure 2.14). In one last attempt to solve this problem, 3D printed polyactic acid caps were made to fit over the low pass filter capacitors, however discharges still occurred across the surface of the PCB.

It was at this point that it was decided to abandon putting all components of the HV bias circuit on the same PCB inside the detector. The components and footprints used in version 2 of the HV PCB were selected to comply with component clearance standards specified in IPC-2221 [46] however these standards are set for

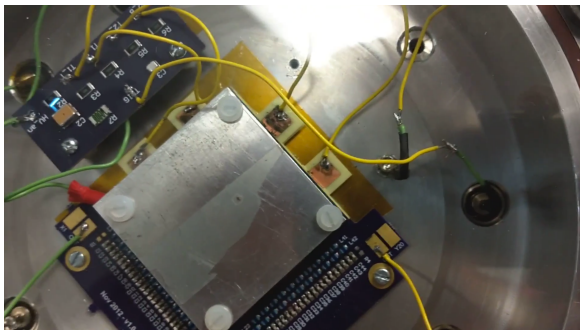

Figure 2.14: Image of high voltage discharges across the low pass filter portion of the HV bias circuit version 2.

parts operating under atmospheric conditions. The low pass filter components were desoldered from the board, R1 and R2 were shorted, and polyimide tape was placed over the C1 and C2 footprints. A secondary filter was constructed as a standalone module kept outside the detector chamber (see Figure 2.15). The capacitors in the low pass filters have the largest voltage drops of any component in the detector and are the most likely source of high voltage discharges.

2.2.3 Thick Gas Electron Multipliers

New THGEMs were required for the detector assembly (see Figure 2.16). A detection system with a spatial resolution of 1 mm would require the use of a THGEM with dimensions below this threshold. The THGEMs were fabricated by a local PCB manufacturer from 0.4 mm thick FR4 with copper cladding. 0.4 mm holes with a pitch of 0.8 mm were drilled through the PCBs and the THGEMs were treated to remove burrs from this process. The active area of the final version of the THGEM is 38.5x38.5 mm^2. Two versions of this THGEM were produced, the first version has a slightly larger active area but this was reduced to prevent overlap between the copper and assembly standoffs.

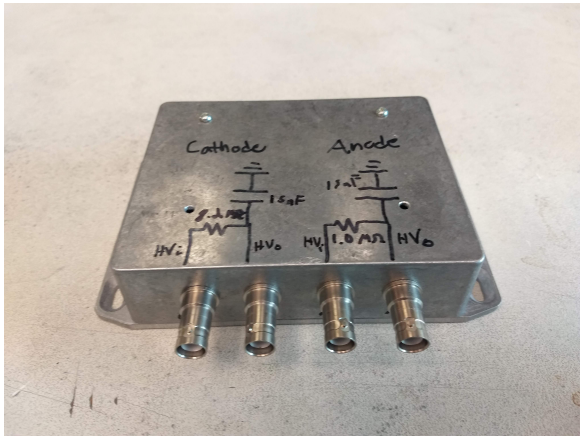

(a) Closed filter circuit.

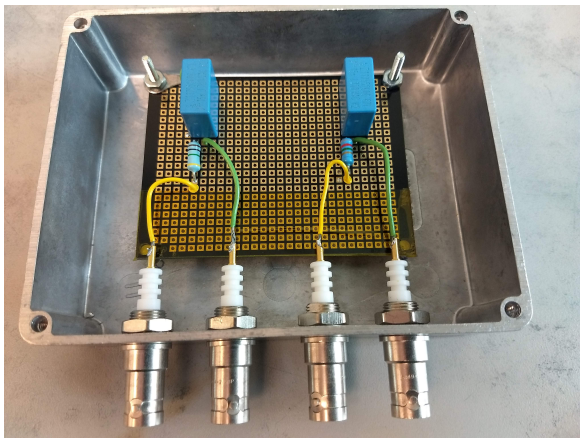

(b) Open filter circuit

Figure 2.15: External HV low pass filter circuit.

The first version of the THGEM had two tabs on two sides to bias the top and bottom of the boards. This design resulted in high voltage copper in close proximity to the components on the delay line (see Figure 2.9). This problem was solved in the second version by reducing the design to one tab for each side of the board such that the tabs would be easier to solder to and do not hang over the components on the 2D readout.

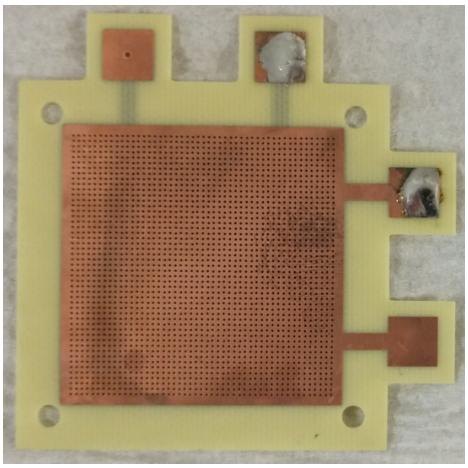

(a) Version 1.

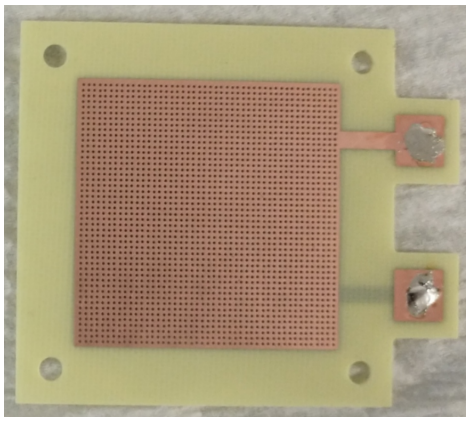

(b) Version 2.

Figure 2.16: THGEMs fabricated from 0.4 mm thick FR4. Holes are 0.4 mm in diameter with a pitch of 0.8 mm. The discoloration seen in version 1 is due to oxidation and damage from high voltage discharges.

2.2.4 2D delay line readout

The 2D readout developed by Hanu et al. is a four layer board composed of diamond shaped copper pads with traces on internal layers connected to two passive delay lines composed of LC cells with a delay of 1.5 ns·cell^{-1} and a characteristic impedance of 217 Ω. This readout was constructed with L = 330 ± 30 nH inductors and C = 7.00±0.07 pF capacitors. The delay line is terminated by a 217 Ω resistor to eliminate signal reflections in the delay line. A general discussion of delay lines is found in Chapter 1. When this delay line is tapped by a RG-58 transmission cable and a preamplifier with a 50 Ω input impedance reflection artifacts appear in the image. An RG-58 transmission cable has a characteristic impedance of 50 Ω, the impedance mismatch between delay line and transmission cable causes a portion of the output signal energy to reflect back towards the delay line. When two transmission lines of differing impedance are connected in series, the fraction of energy reflected is described

by the reflection coefficient Γ described by Equation (2.2.1). The attenuation by the real resistance of the inductors is specified by Equation (2.2.2) where R is the DC resistance of the delay line, typically a few ohms.

$$\Gamma = \frac{Z_0 - Z_1}{Z_0 + Z_1} \tag{2.2.1}$$

$$A = 1 - (Z_0/(Z_0 + R)) \tag{2.2.2}$$

With a 217 Ω delay line and 50 Ω transmission line, $\Gamma = 0.62$ is expected. To minimize image artifacts caused by reflections the delay line components are replaced with with $L = 75 \pm 2$ nH inductors and $C = 30.0 \pm 0.3$ pF capacitors and the delay line terminators were removed. These components result in a delay line with characteristic impedance 50 Ω but maintain a delay of 1.5 ns·cell^{-1}. No reflection are expected because the impedance of the delay line matches the impedance of the RG-58 transmission cable and the input impedance of the VT120A preamplifier. A comparison of the preamplifier output signals is seen in Figure 2.17 and Figure 2.18. In Figure 2.17, multiple peaks in the output signal are seen with subsequent peak heights being attenuated by a factor of about 0.6 which is close to the expected value. As expected no reflections are seen in the output signal of the $Z_0 = 50$ Ω delay line.

The delay line length was measured using a Berkeley Nucleonics model PB-5 pulse generator [47]; the testing circuit is depicted in Figure 2.19. A CAEN DT5743 desktop digitizer with a 50 Ω input impedance was used to digitize the input and output signals. RG-58 cables of equal length were connected to the input and output

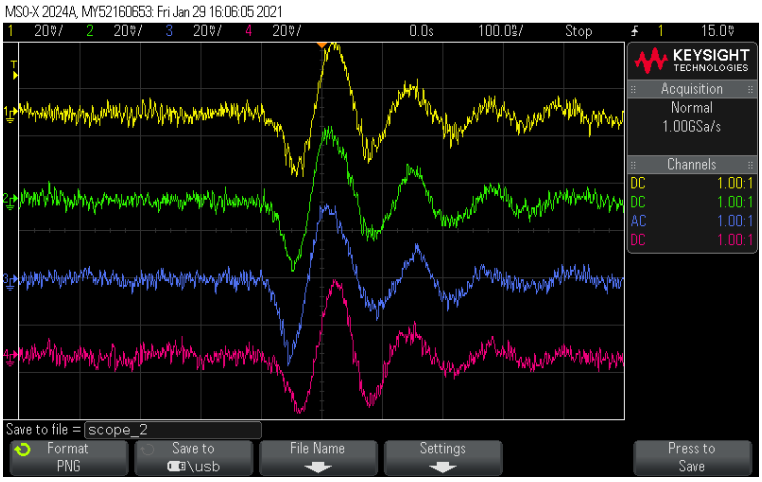

Figure 2.17: Preamplifier output signals from a Z_0=217 Ω delay line with visible reflections. Pictured from top to bottom are the X left, X right, Y left and Y right channels. Signals are produced via charge amplification by a two-stage THGEM configuration with an Am-241 source.

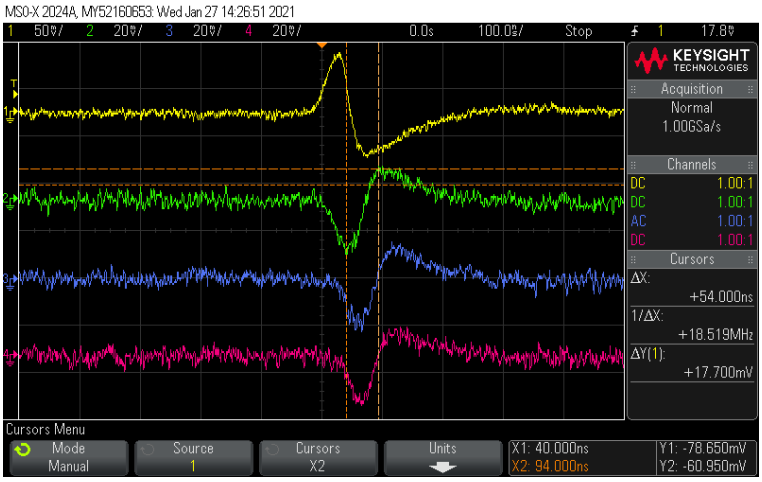

Figure 2.18: Preamplifier output signals from a Z_0=50 Ω delay line. No signal reflections are discernible. Pictured from top to bottom are the trigger, X left, X right, and Y left channels. Signals are produced via charge amplification by a two-stage THGEM configuration with an Am-241 source.

port for the X and Y axis signals. An example measurement of the delay line length is seen in Figure 2.20 and a summary of results is seen in Table 2.1. It is observed

that cell delays are greater than 1.5 ns $\cdot$ cell^{-1} for all three readout designs. For the 20 and 32 cell readouts this is likely due to stray capacitance on the readout between array pads and internal traces. A 51 cell delay line was designed to improve image resolution and reduce stray capacitance but did not function as desired due to high DC resistance of the inductors.

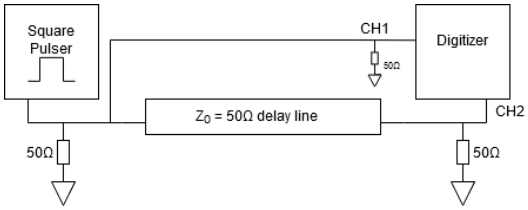

Figure 2.19: Delay line test circuit to measure full delay line length.

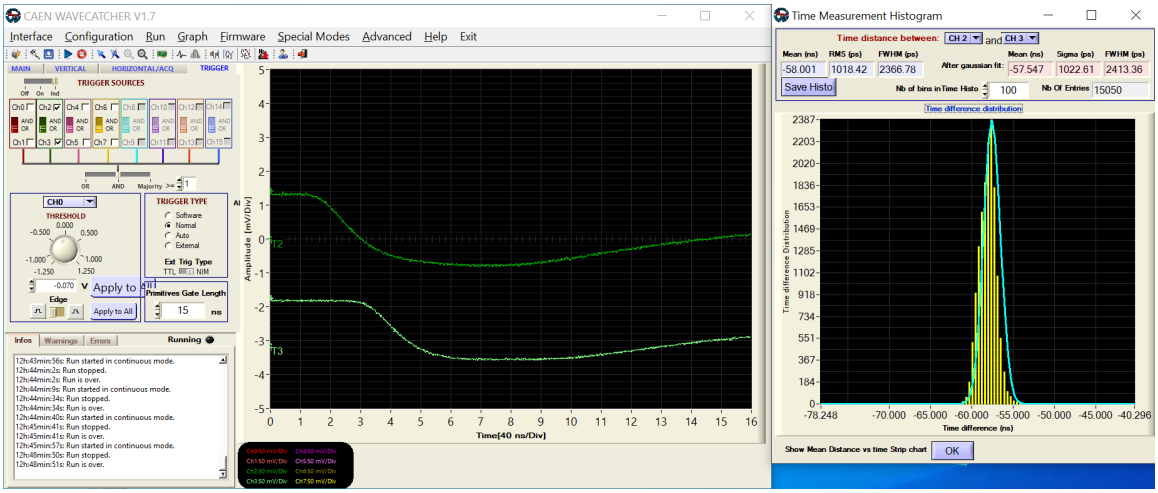

Figure 2.20: Delay line length measurement of the X-axis of the 32 cell 2D readout board with characteristic impedance Z_0=50 Ω. On the left is the digitized waveform of the input (dark green) and output (light green). The relative time difference between signals is measured by on-board CFD firmware and the resulting histogram is seen on the right with a gaussian fit.

Table 2.1: Summary of delay line length measurements results for 20, 32, and 51 cell delay lines.

Z_0=50	20 cells		32 cells		51 cells	
	X-axis	Y-axis	X-axis	Y-axis	X-axis	Y-axis
Length(ns)	35.3	35.3	58.0	57.7	243.5	241.5
FWHM (ns)	6.8	7.6	2.4	2.6	13.9	13.3
Cell delay ($ns \cdot cell^{-1}$)	1.8	1.8	1.8	1.8	4.8	4.7

With new THGEMs, a revised 2D readout board, and a rebuilt HV bias circuit with filtering, a successful test of the detector in an alpha configuration was performed. Typical preamplifier output pulses (Ortec VT120A fast timing preamplifier) using an alpha source can be seen in Figure 2.18. From this point reconstruction efforts could move on to pulse amplification and timing.

2.2.5 Amplification and timing

Early attempts to recreate the pulse processing chain from Hanu et al. [45] used the same equipment including the homemade pulse amplifiers and Ortec CFDs. Unfortunately, several months into testing the CFDs started to fail and without the ability to repair these modules, a replacement pulse processing chain was needed. Any replacement module(s) would have to meet the following requirements:

- Fast timing pickup
- 50 Ω input impedance
- Negative input polarity
- Integral timing filter constant less than 25 ns
- CFD timing with adjustable delay

The CAEN N1068 16 channel programmable spectroscopy amplifier and CFD module [48] was selected to satisfy these requirements. A channel block diagram for the N1068 is seen in Figure 2.21. Because this module contains timing filter amplification circuits it was able to fully replace the amplification and timing portions of the pulse processing chain.

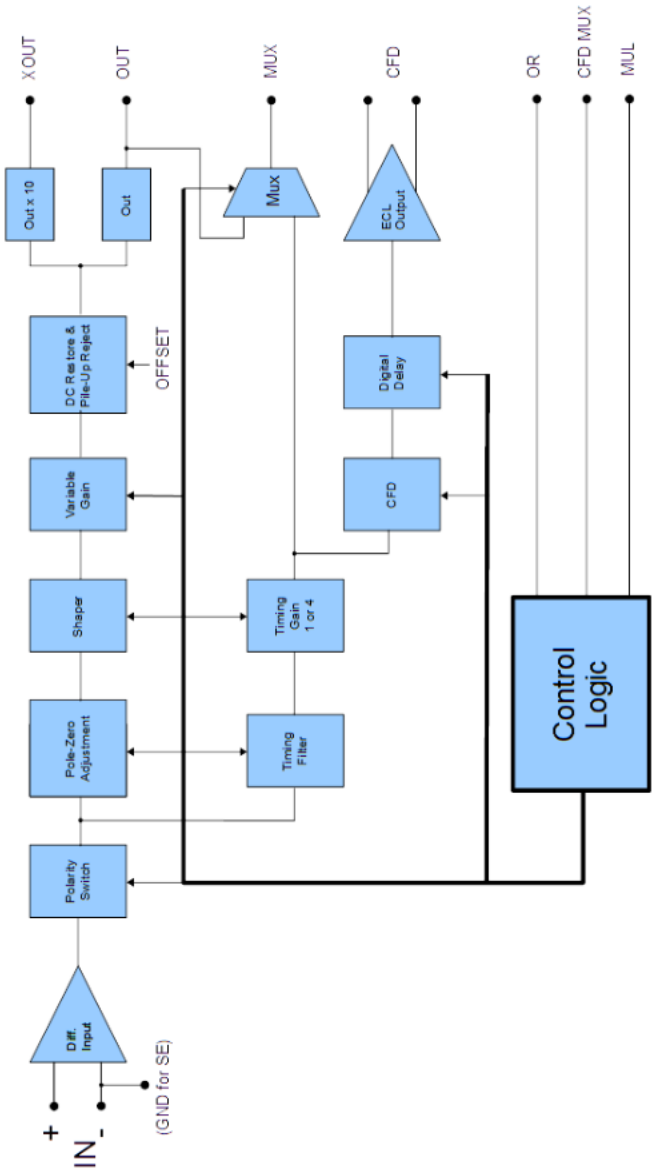

Figure 2.21: A channel block diagram for the CAEN N1068 module [49]. Copyright CAEN S.p.A, used with permission.

This module is an excellent all in one alternative to the former pulse processing chain however one downside of it is the output logic of the CFD signals. Because the N1068 outputs in emitter-coupled logic (ECL) but the TDC-GPX operates on low

voltage transistor-transistor logic (LVTTL) fast translation of the timing signals is required. ECL to LVTTL translation was accomplished with a homemade comparator based translation circuit. The requirements of the comparator are determined by the limitations of the TDC-GPX and the delay line. The TDC-GPX has a time resolution of 81 ps, a maximum event rate of 200 MHz in I-mode and the delay line has a nominal delay per cell of 1.5 ns. The selected comparator must have a delay of less than that of a delay line cell, and an event rate greater than or equal to the event rate of the TDC-GPX. The property of a comparator that determines its time resolution is called *jitter* and it describes the deviation of the output signal time from the true time of the signal. The ON Semiconductor MC100EPT25 was selected to meet these requirements. It is a differential ECL to LVTTL translator with a propagation delay of 1.1 ns, a maximum frequency of 275 MHz and a jitter less than 1 ps.

Two versions of a PCB housing five translator ICs were produced differentiated by their power supply scheme. The first version of the PCB attempted to power the ICs with a simple voltage divider. The manufacturer was asked to recommend the necessary components to power five ICs and they suggested a divider made from 70 Ω and 27 Ω resistors to drop 12 V input from a nuclear instrumentation module (NIM) crate to 3.3 V but the current drawn from the ICs was enough to heat the resistors and melt the solder causing the resistors to slide right off their footprints. A desktop power supply was used to directly power the circuit when using this first version of the translation PCB. The second version (see Figure 2.22) utilizes two linear regulators (the LM337KC and the LM317KC) and large ground planes to dissipate heat (see schematic in Figure A.2). This version of the translator circuit is far superior in that it has reduced noise due to filtering on the power supply circuit and it can be powered

with a NIM crate. In Figure 2.23 you can see an example signal including ECL to LVTTL translation.

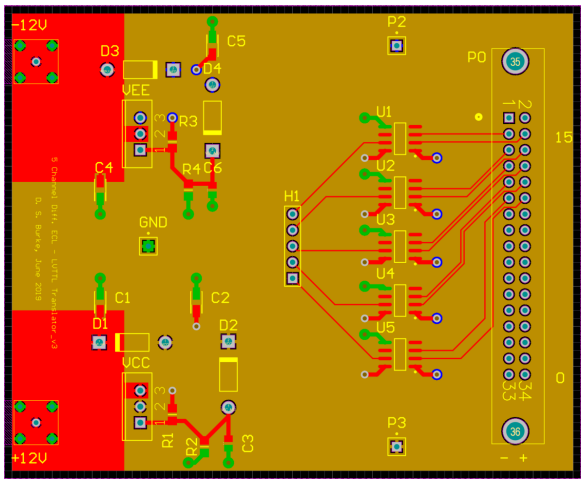

(a) Render of PCB with internal traces and ground plane.

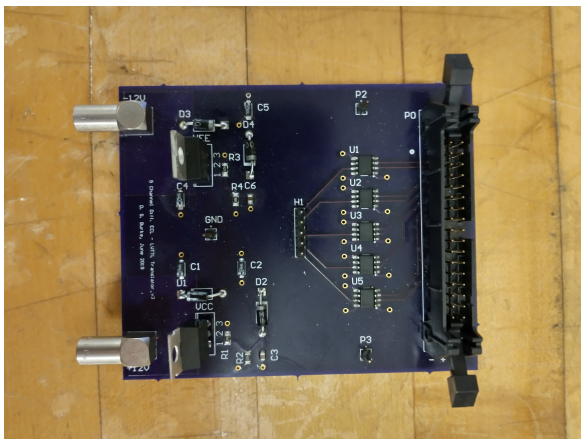

(b) Image of populated translation PCB.

Figure 2.22: Version 2 of the ECL to LVTTL 5 channel translation PCB

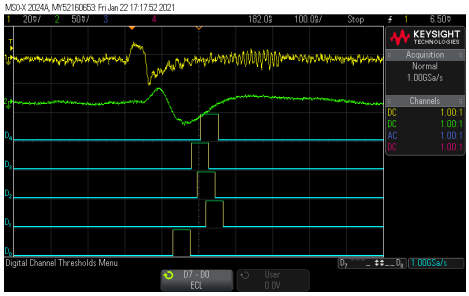

(a) N1068 output signals including logical ECL timing signals.

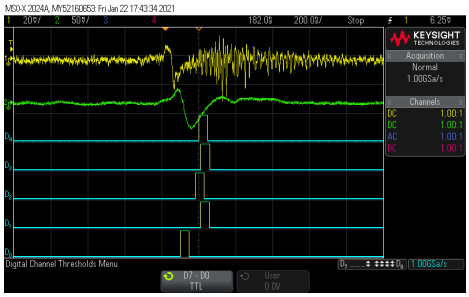

(b) ECL to LVTTL translated output.

Figure 2.23: Example of ECL to LVTTL logic translation. Included with digital timing is the preamplifier input signal (yellow) and the timing filter output from the N1068 multiplixer (green).

2.3 Imaging results and discussion of firmware implementation

With a new pulse processing chain images could be collected. A block diagram of the new pulse processing chain is seen in Figure 2.24. The homemade amplifiers and CFD modules are replaced with the CAEN N1068 and a 5 ch. differential ECL to LVTTL translator is included after the N1068 to translate the timing output. Without a radiation attenuating sample, images should appear as a square array of bright squares. This pattern is the result of the discrete nature of the 2D anode array of diamond shaped copper pads and the square shaped layout of the THGEM holes. Images were collected with an alpha source using the assembly configuration in Figure 2.7. 100 torr tissue equivalent propane (TEP) was the fill gas. In Figure 2.25 the first image collected with the 20 cell delay line readout without a sample object is seen. It is expected that the image should appear as rows of bright points corresponding to the array of pads but in addition to this are seen butterfly shaped voids extending

from the image corners with a larger central void. When left running overnight (see Figure 2.26) the image exhibits bright noise features. These images were taken with version 1 of the ECL to LVTTL translator which was powered by a desktop power supply. This noise is thought to be due to lack of power supply filtering on the PCB and spurious noise from the desktop power supply. Later images taken with version 2 of the translator PCB lacked similar noise artifacts.

A Cd-109 X-ray source was set $\sim$ 22 cm from the chamber wall to reduce the size of the angular distribution of photon trajectories impinging on the drift region of the detector and an image was collected. The resulting image seen in Figure 2.27 was collected after leaving the TDC-DAQ running overnight using version 2 of the translator PCB. Again a butterfly shaped void is seen in the image but with less pronounced Y axis lobes. New artifacts also appear as rough crescents near the corners and a cross at the origin. It is believed that the cross is due to cross talk between neighbouring channels of the TDC-GPX that becomes most prominent under high event rates. The crescent artifacts have not been explained, they are potentially a result of malfunction in the FPGA or TDC-GPX PCB as they do not appear when using digital implementations of the reconstruction algorithm. It is thought that these crescents may have been due to overlap of the spacers with the THGEM copper cladding but the same artifacts are seen with THGEMs that have a smaller active area with no overlap.

To see if these same artifacts appear with neutrons, the assembly was reconfigured to house a neutron converter (see Figure 2.9) and brought to beam port six at the MNR. Beam port six houses the MAD, a neutron instrument that uses single crystal silicon to deflect a thermal neutron ($\sim$ 25 meV) beam towards the sample stage.

Unlike the alpha and X-ray tests, a dark current from the unexposed readout was observed (see Figure 2.28). The dark current noise is binned near the origin which would suggest it is not due to background radiation but is instead electronic noise. A 25 minute exposure of the detector was taken with thermal neutrons to collect the image in Figure 2.29. The neutron event rate is significantly lower than the X-ray event rate at only 18 events·second^{-1}, much lower than expected. The neutron fluence measured by a BF_3 detector is typically on the order of 10^5 cm^{-1}·s^{-1}. Based on the expected transmission thermal neutron escape efficiency of a 3.2 μm thick microlayer of $^{10}B_4C$ (4%) (see Chapter 1) and the active area of the detector it is expected that the event rate be on the order of 10^4–10^5 events·second^{-1}. The presence of the butterfly shaped voids and the low event rate suggest that a significant number of events are being lost.

2.3.1 Choosing to move to digitized solution

Attempts were made to understand the butterfly shaped voids. A BNC PB-5 pulse generator and selectable delays were used to troubleshoot. Using the delays, a single pixel could be specified by setting the delay between the arrival of X and Y axis signals. When the delay was set to light up a pixel in the void region, there was no system response. A version to directly read the timestamps produced by the TDC-GPX was developed by Hanu et al. and used to debug the TDC-DAQ. Timestamps were collected overnight without changing the X and Y axis delays, the results are seen in Figure 2.30. In Figure 2.30a it is seen that the two pairs of *real* peaks are about bin 30 and bin 80. These peaks are expected from the delays set between the X and Y axis signals of 2.5 ns and 6.5 ns respectively. All other peaks are unexpected

and unexplained however it does not appear as if a significant number of events were ignored by the TDC-GPX. The height of peaks such as those around bin 105, 125 and 775 suggest that most events are likely producing multiple timestamps from the TDC-GPX. Since the FPGA histogramming firmware rejects events with multiple timestamps, this is likely the explanation for the lower than expected neutron event rate and possibly the butterfly shaped voids. New PCBs housing the TDC-GPX were professionally manufactured and populated in case the boards were somehow damaged but there was no observed improvement. The on-board diagnostics on the SP601 returned no system errors indicating no detectable damage to the development board.

At this point in the project there were less than eight months until the expected end date for the experimental work. In order to solve this issue a great deal of troubleshooting on the SP601, firmware, and TDC-GPX would need to be done to determine the cause of these observed artifacts. Implementing the data acquisition system (DAQ) in hardware is useful for reasons discussed at the beginning of this chapter however the goal of this project is to show that THGEMs and a passive delay line readout can be used effectively in a neutron imaging system. To prove this concept, the hardware implementation is not strictly necessary. It was decided that in order to meet the goals of the project the hardware approach to the TDC-DAQ would be abandoned in favour of a digitized solution. The entire pulse processing chain after the preamplifiers was replaced with a CAEN DT5743 desktop digitizer to perform measurements and record fully digitized signals. For some measurements, the homemade amplifiers developed by Hanu et al. were included in the pulse processing chain after the preamplifiers. Using the CFD timing function of the CAEN

Wavecatcher software, measurements of the signal arrival timestamps in real time were taken and saved to a text file. Using the same reconstruction algorithm as the FPGA histogramming block written in Python the image is reconstructed from these timestamps. The results of this work are the subject of Chapter 4.

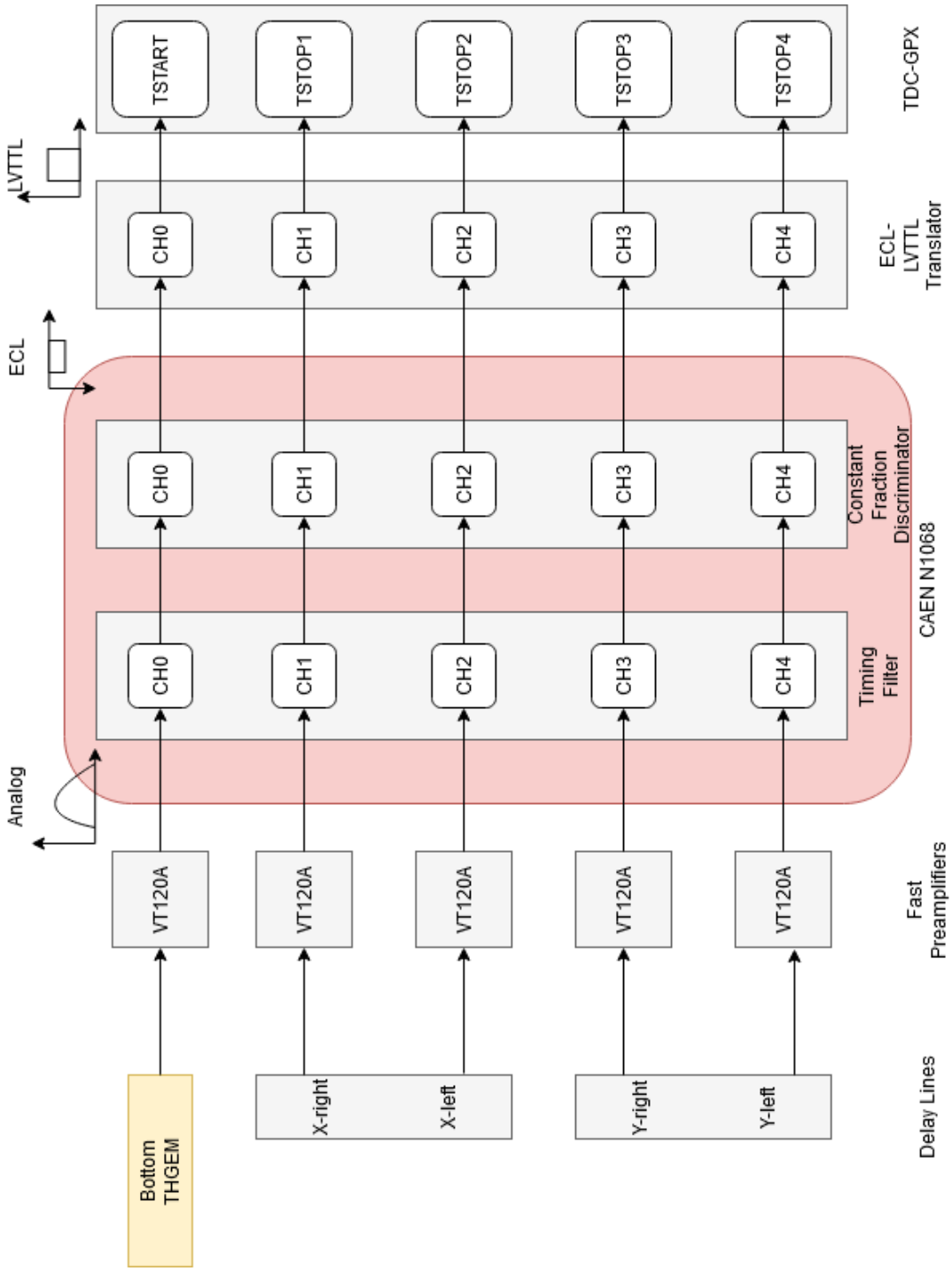

Figure 2.24: Block diagram for the hardware implementation of the pulse processing chain.

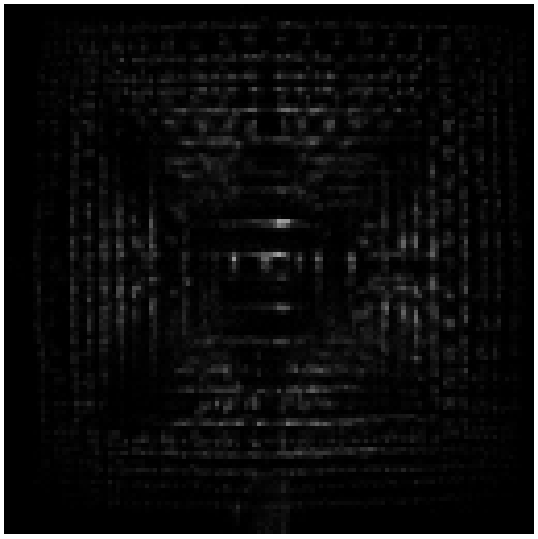

Figure 2.25: Image of detector exposed to alpha radiation from an Am-241 source 5 mm above THGEM 1. Collected with the hardware TDC-DAQ.

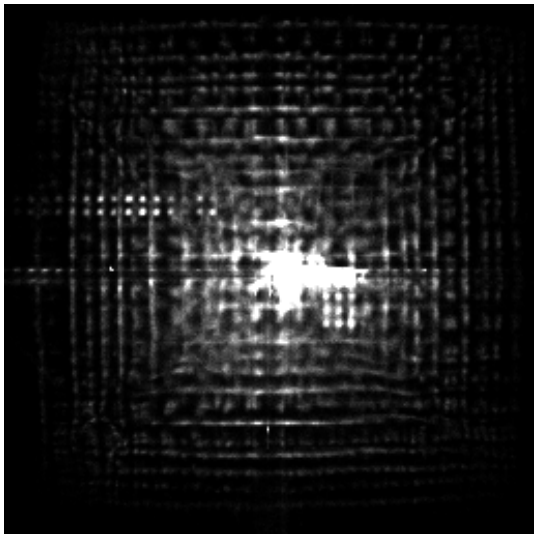

Figure 2.26: Long exposure image of detector exposed to alpha radiation from an Am-241 source 5 mm above THGEM 1 collected overnight. Collected with the hardware TDC-DAQ

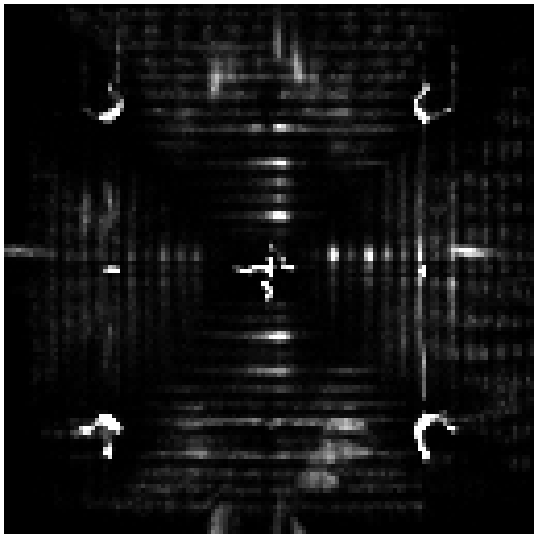

Figure 2.27: Overnight exposure image of detector exposed to X-ray radiation from Cd-109 source 22 cm from the detector wall. Collected with the hardware TDC-DAQ.

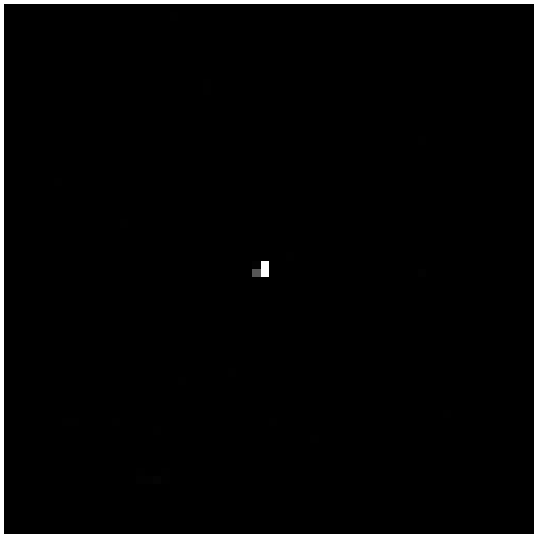

Figure 2.28: Dark current observed at MNR beam port six. Image collected with the hardware TDC-DAQ.

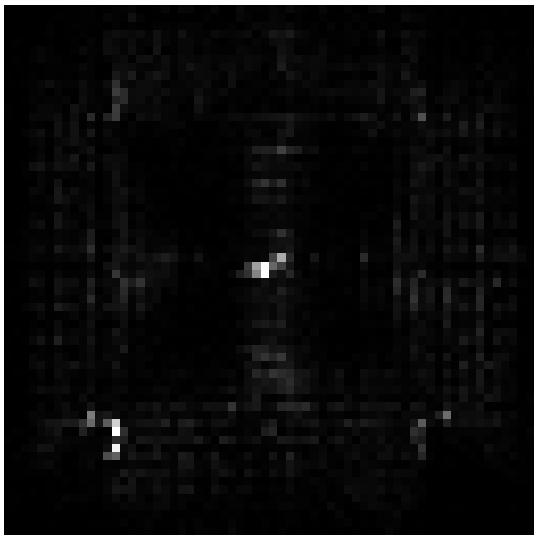

Figure 2.29: Image collected after full exposure of the detector to thermal neutrons at MAD. Image collected with the hardware TDC-DAQ.

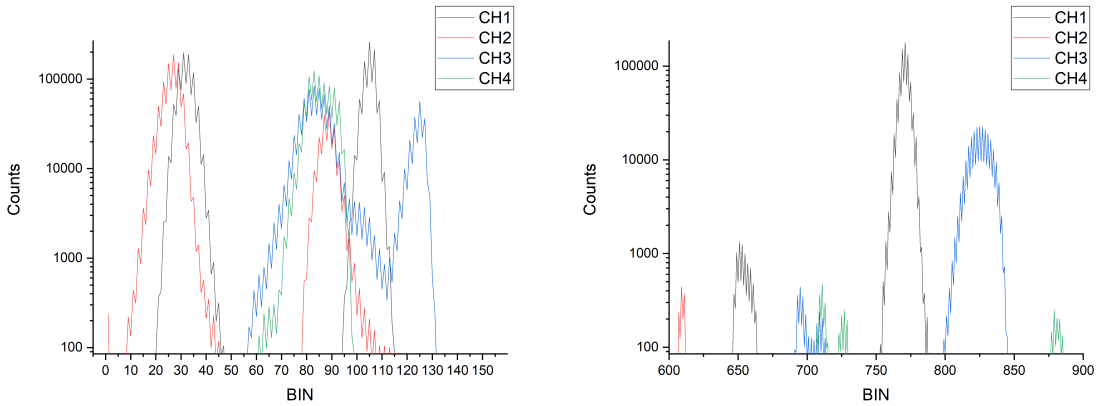

(a) (b)

Figure 2.30: Binned timestamps resulting from overnight collection of a test pulse. The X axis pulses differ by 2.5 ns and the Y axis pulses differ by 6.5 ns. Each bin is 82 ps wide.

Chapter 3

Gadolinium oxide paint as a shield and image contrast agent

As technologies in the nuclear sector advance, there are new radiation safety challenges that must be overcome to keep workers safe. Popular multilayer shields are simple and are often ad hoc constructions by users of the work space. These shields are typically made of two components, a high H density component to moderate neutrons like polyethylene or water and a high Z component to attenuate gammas like Pb or concrete. For some applications however more sophisticated solutions are required to meet various thermal or mechanical constraints. For example, one problem with polyethylene shielding is that pure polyethylene is flammable and thus not always suited for high temperature applications. Such constraints have prompted the development of novel shielding materials and in response sophisticated multilayered and composite materials have been developed to meet the needs of research and industry [50]. Sometimes, as depicted in Figure 3.1, a high Z material is used to attenuate

fast neutrons in the initial layer. This takes advantage of the lower energy first excited states found in high Z nuclei (ex. $^{56}_{26}\mathrm{Fe}^{\mathrm{J}^{\pi}=2^{+}}$ = 0.85 MeV and $^{184}_{74}\mathrm{W}^{\mathrm{J}^{\pi}=2^{+}}$ = 0.11 MeV [51, 52]) to attenuate neutron energies by inelastic scattering [53]. It has been seen that multilayer shields that attenuate fast neutrons by inelastic scattering through a high Z layer can outperform more traditional shields that use high H density materials as its initial layer; one example being a Pb-PE-Pb shield [54]. In this chapter, the performance of a neutron shielding paint which can be used as or in combination with the thermal neutron attenuation layer of a multilayer shield will be discussed.

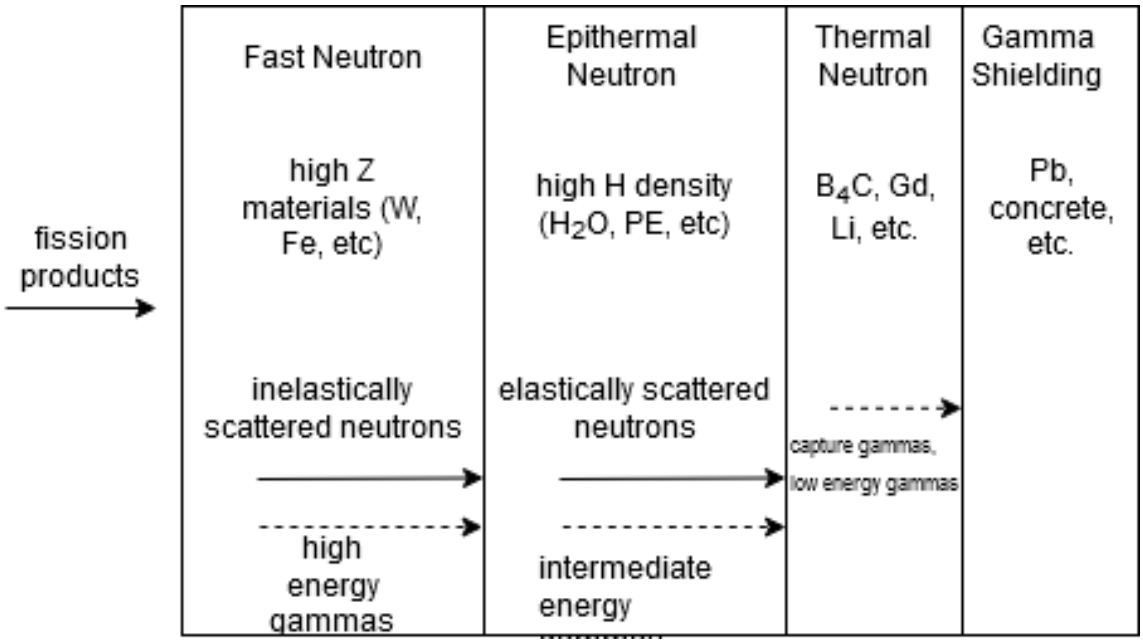

Figure 3.1: Schematic of a sophisticated multilayer shield design.

The work discussed in this chapter was initially motivated by a need to produce a low resolution (minimum feature size 1 mm) neutron imaging test object to evaluate a novel digital neutron imaging system. The low resolution of this proof of concept system makes it difficult to acquire neutron imaging test objects. Test objects such as

the Siemens Star [55] popular in research or the ASTM E545 [56] standard popular in industry have features designed well below 1 mm and are designed for high resolution neutron radiography. Readily available elements with high neutron absorption cross sections are Gd, Cd and B. Gd and Cd are both toxic and difficult to machine without contaminating their tools. This fact, in combination with the small features make cutting standards from these materials difficult or impossible for most commercial machine shops. DC-magnetron sputtering and lithographic methods were considered but were deemed impractical with the available equipment so it is determined that a physically robust paint mixed with oxide powder would be a practical solution. The performance of the resulting paint as a test object medium suggests it may also perform well as a more general purpose neutron shield.

Gd_2O_3 as a thermal neutron attenuating additive in composite materials is not a novel idea in and of itself, however it has seen relatively little attention in the literature compared to alternatives. Elemental Gd has the highest neutron absorption cross section in nature for thermal neutrons of any element however it is often overlooked in favor of B for neutron shielding due to the increased cost of Gd and the higher energy capture gammas. The thermal neutron cross section of elemental Gd is 49700 b, the bulk of this cross section is due to the isotopes ^{155}Gd and ^{157}Gd [37]. The relevant neutron capture reactions are ^{155}Gd(n,γ) and ^{157}Gd(n,γ) with $Q_{155} = 8536.35 \pm 0.07$ keV and $Q_{157} = 7937.39 \pm 0.06$ keV [57]. The reaction products are primarily prompt gammas and internal conversion electrons. The prompt gamma rays carry away the majority of the Q value of the reactions; 99.2% in the case of ^{157}Gd [26]. The prompt gamma spectrum for natural Gd has peaks at 83, 247, 975, 1230, 6750 and 7860 keV although most of the gammas are in the region below 1230 keV [58]. When

compared to B_4C as an additive in polyethylene, Gd_2O_3 is the superior additive in terms of thermal neutron attenuation [59].

A shielding paint layer could produce thinner multi-layer shields of the type seen in Figure 3.1 or it could be added to existing installations where materials exist to attenuate the prompt gammas. A shielding paint can be applied to other shielding materials like Fe, polyethylene, or Pb, to add a layer of neutron attenuation and it has the benefits of being low cost, thin, and versatile.

3.1 Paint Preparation

The shielding paint is prepared by mixing 99.9% Gd_2O_3 powder (average grain size 1–4 μm) with a base paint. It is important that the selected base have the following properties to ensure stability and ease of prototyping:

- Ablation Resistance
- Water Resistance
- Durability
- Fast drying
- Ease of application
- Adherence to aluminum

Considering these requirements, MINWAX® Fast-Drying Polyurethane Clear Semi-Gloss paint is selected. Additional features of this paint include clarity, and low viscosity allowing additives to be easily mixed into it. Paint additives can affect the

mechanical properties of the resulting coating. Too much Gd_2O_3 would cause the coating to ablate and wear over time. Samples of the shielding paint are prepared with increasing amounts of Gd_2O_3 additive to ensure the shielding paint would still easily adhere to a smooth surface without loss of durability. The sample preparation procedure is as follows:

1. Draw 10 mL polyurethane with pipette
2. Weigh into beaker on an analytical balance
3. Record mass
4. Fill cavities of ice cube tray with 10 mL polyurethane
5. Weigh out Gd_2O_3 to target mass for mass fraction 0.01 in small beaker
6. Transfer oxide to sample tray.
7. Weigh oxide remaining in beaker to calculate mass transferred.
8. Mix Gd_2O_3 into polyurethane with wooden applicator
9. Use foam brush to apply paint to acrylic test surface
10. Repeat for all target mass fractions
11. Allow samples to dry 24 hours

Table 3.1 summarizes the sample paint preparation.

Table 3.1: Gd_2O_3 paint sample preparation. The polyurethane volume and mass are 9.75±0.25 mL, 7.1±0.2 g respectively.

target mass fraction	Gd_3O_3 added (g)	mass fraction
0.01	0.0740	0.010±0.008
0.02	0.1190	0.02±0.01
0.03	0.1983	0.03±0.01
0.04	0.2914	0.04±0.02
0.06	0.4472	0.06±0.02
0.08	0.5826	0.08±0.02
0.10	0.7633	0.10±0.02
0.12	0.9442	0.12±0.02
0.16	1.3559	0.16±0.02
0.20	1.7634	0.20±0.02
0.25	2.3684	0.25±0.02
0.30	2.9829	0.30±0.02
0.35	3.794	0.35±0.02
0.40	4.7002	0.40±0.02

A foam brush is used to paint sample swatches on an acrylic sheet. This can be seen in Figure 3.2. All samples are subjected to a physical integrity check. For all samples it is found that:

- All paint dry, wooden applicators make clean contact
- No cracks
- No tackiness
- All samples could be removed with metallic scraper

It is found that mass fraction 0.4 retains mechanical stability. For further analysis, 300 mL of paint with Gd_2O_3 mass percentage of (40±2)% are produced.

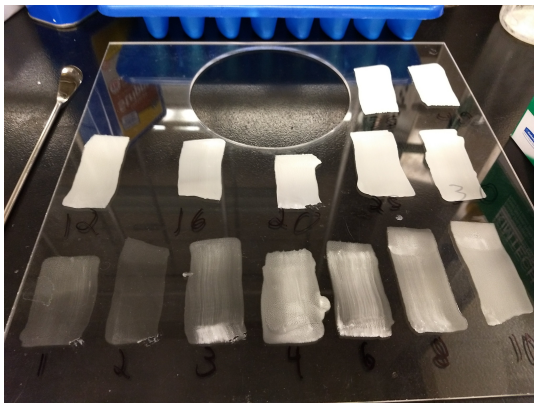

Figure 3.2: Gd paint swatches on an acrylic sheet. The mass fraction of each sample is written in black underneath the sample. The top two samples from left to right are mass fractions 0.35 and 0.40 respectively.

3.1.1 Sample Preparation

The resolution standard selected is derived from the United States Air Force 1951 (USAF 1951) imaging resolution optical standard for testing optical resolution of imaging devices [60]. This is a common standard for evaluating the resolution of optical systems. A subset of the USAF standard is selected to create the optical resolution standards. The layout of this standard is seen in Figure 3.3.

A stencil and stipple brush is used to paint the standard onto aluminum. The stencil is laser cut from a bulk sheet of frisket film. Frisket film is a self-adhesive sheet that can be applied to and peeled off a surface. The sample preparation procedure is as follows:

1. Clean and prepare a 5x5x0.1 cm wafer of aluminum
2. Apply cut frisket film stencil to wafer
3. Thoroughly mix bulk paint with automatic mixer
4. Dab paint onto wafer through the stencil using a stipple brush

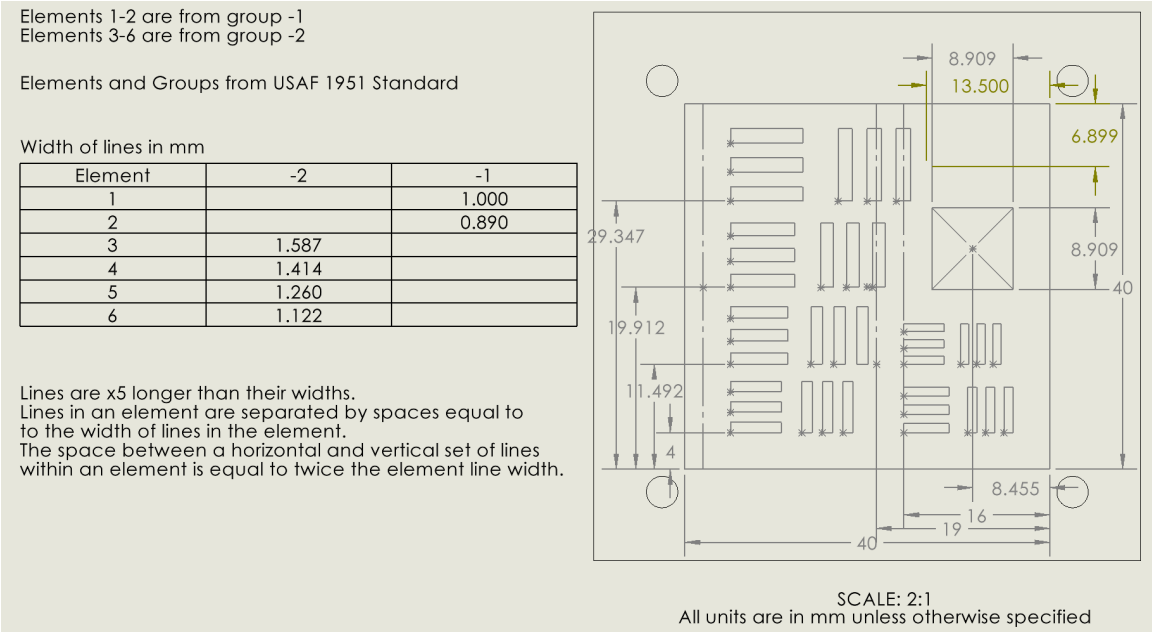

Figure 3.3: Technical drawing of the USAF 1951 derived resolution standard produced with the shielding paint [60].

5. Allow to dry at least 24 hours

6. Carefully remove frisket film

7. Repeat to produce four standards

8. Align and stack three samples together and secure with electical tape

The results of this preparation can be seen in Figure 3.4.

Samples used in thermal neutron beam measurements are prepared on 1 mm thick Al-6061 substrates. After a 10x10 cm^2 square is taped off, the interior area is painted and the tape is then removed after drying. The wet and dry masses of each coat are recorded. Samples with one coat, two coats and three coats of paint applied with a foam brush are prepared.

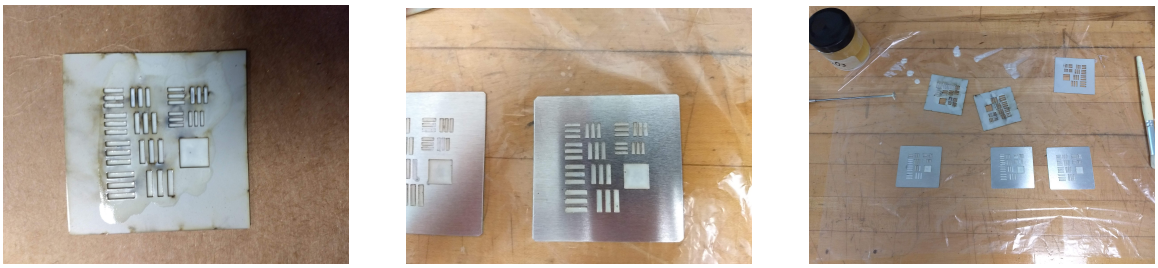

(a) (b) (c)

Figure 3.4: Prepared USAF-1951 derived, Gd based paint samples; (a) A closeup of the paint applied through the frisket stencil; (b) A completed sample; (c) Multiple completed samples.

3.2 Experiments

3.2.1 Neutron attenuation measurement using submerged ^{241}AmBe source

In order to test the attenuation capability of the Gd paint, a submerged BF_3 proportional counter and ^{241}AmBe neutron source are used. A schematic of the experiment is depicted in Figure 3.5. A hollow, 0.25 inch thick aluminum tube is painted and used as an attenuator. The performance of this attenuator is compared to a 4.3 ± 0.2 mm thick Cd attenuator. The ^{241}AmBe source is a wide spectrum source owing to the water moderator between the source and the counter. Neutrons arriving at the counter assembly have a wide range of possible kinetic energies, from moderated thermal neutrons to the unmoderated fast neutrons. This is similar to the spectrum of neutrons around a nuclear reactor core submerged in water. The BF_3 neutron count rate in the water tank is highest at 8 cm from the source which is the minimum distance between the proportional counter assembly and the source. The transmission T and attenuation A factors satisfy Equation (3.2.1).

$$1 = \mathrm{A} + \mathrm{T} \tag{3.2.1}$$

where T is the fraction of neutrons transmitted through the attenuator and A is the fraction of neutrons attenuated.

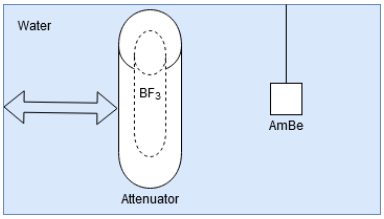

Figure 3.5: Schematic of the ^{241}AmBe experimental setup. A BF_3 proportional counter inside a thin hollow aluminum tube is submerged in a light water tank with a 1 Ci ^{241}AmBe neutron source. An attenuator can be inserted between the aluminum walls of the tube and the proportional counter. The proportional counter assembly is mounted to a movable bridge to adjust the distance to the ^{241}AmBe source.

3.2.2 Neutron beam radiography at the McMaster nuclear reactor

In cooperation with Nray Services Ltd and McMaster Nuclear Operations & Facilities [61] neutron radiographical images of the samples were taken at the McMaster Nuclear Reactor. A beam of thermalized neutrons from the reactor pool is attenuated by a set of four test objects to compare the contrast of painted standards to a cadmium attenuator. The test objects selected are:

- A hand-cut 1 mm thick Cd wafer
- A stack of three aligned USAF 1951 painted aluminum wafers seen in Section 3.1

- A single USAF 1951 painted wafer
- An aluminum wafer half coated in a single application of paint

The beam port is a collimator that extends from inside the reactor pool through the containment wall to an exterior imaging station. The collimator contains several filters to attenuate fast neutrons and gammas in the imaging beam. The collimator is surrounded by high density concrete shielding. Imaging is performed using the neutron imaging industry standard cassette system. Test objects are mounted to aluminum cassettes in front of a neutron sensitive film. After exposure this film is developed, measured with a densitometer and digitized as an array of gray scale values.

3.2.3 Thermal neutron beam attenuation at McMaster Alignment Diffractometer

The McMaster Alignment Diffractometer (MAD) [62] is a general purpose triple-axis instrument that can be used to measure large angle neutron diffraction from samples in single crystal, polycrystalline, and powder form. It is primarily used for sample alignment and the evaluation of crystal quality. To determine pure thermal neutron transmission properties of the paint shielding samples are produced to measure at the MAD. Despite being designed for crystalline samples, the sample stage is large enough to accommodate the paint samples. The neutron transmission properties of the sample are measured with a pure beam of thermal neutrons of wavelength 1.8 Å (E = 25 meV). The MAD utilizes a single crystal of silicon to select the desired wavelength of thermal neutrons to a high degree of precision.

3.3 Analysis and Discussion

As described in Section 3.1, the Gd paint is prepared by mixing Gd_2O_3 powder with a polyurethane base. The paint is mixed using a small handheld automatic paint mixer, however there is no way to tell how evenly the powder is mixed through the base paint or if there is oxide powder stuck to the bottom of the container. It is also observed that in the sample containers and the prepared bulk paints the powder would settle to the bottom over the course of several days. Because of this, the mass fraction of each swatch in Figure 3.2 is likely slightly less than labeled.

When applying multiple coats of paint to the aluminum cylinder used in the submerged ^{241}AmBe source experiment the layer thickness cannot be guaranteed consistent. For each layer, paint is applied with a foam brush over half the outer surface area of the cylinder but without a method of measuring the wet and dry layer thickness there is no way to empirically determine the uniformity or thickness of the coats.

The transmission factor of the painted attenuator is compared to that of a thick Cd attenuator as a reference measurement. This is done to mitigate the effect of epithermal and fast neutrons on the results. With this technique the relative attenuation factor $\frac{A_{Gd}}{A_{Cd}}$ is approximated as the attenuation factor of the paint for thermal neutrons. The results of the ^{241}AmBe attenuation experiment are seen in Figure 3.6 and Table 3.2.

It is apparent from the relative attenuation factors of each coat in Table 3.2 that the attenuation of subsequent coats is inconsistent. This indicates that paint may apply thinner for subsequent coats.

The radiographic film from the exposure of the test objects at the imaging beamline of the McMaster Nuclear Reactor has been analyzed with a densitometer and digitized.

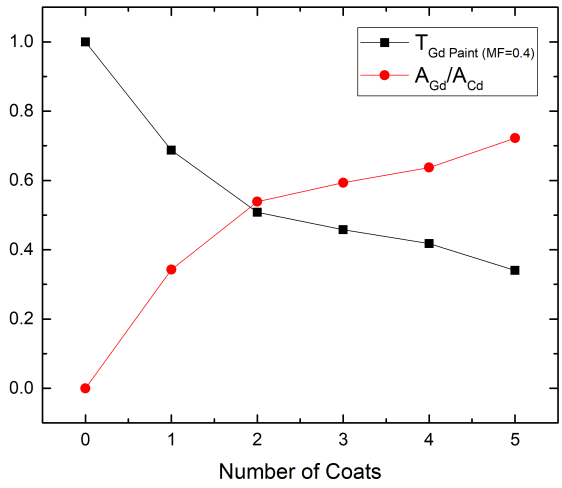

Figure 3.6: (Black) Transmission factor T of neutrons through Gd_2O_3 based paint on 0.25 inch thick Al pipe. (Red) The relative attenuation factor, the ratio of neutron attenuation factor of the painted pipe to a thick Cd attenuator where A_{Cd} = 0.914±0.001.

The neutron transmission value in Table 3.3 is the ratio of the light transmission value of the film in the region of the object of interest to local background. The fog level of the exposure is 0.12 and is subtracted from the densitometer measurements before the neutron transmission values are calculated. The results of this analysis are seen in Table 3.3. The neutron transmission values are calculated by Equation (3.3.1).

$$\text{Neutron Transmission} = \frac{\text{Densitometer} - \text{Fog}}{\text{Background} - \text{Fog}} \tag{3.3.1}$$

It is seen that 24% of neutrons are transmitted through the Cd. The Cd object is a 1 mm thick wafer of Cd with more than 10 attenuation lengths for 1.8 Å (25 meV) neutrons. This suggests significant gamma and epithermal neutron contamination in the beam because for a pure thermal beam of neutrons one would expect the neutron

Table 3.2: Neutron transmission factor T results for Gd painted attenuator with a submerged ^{241}AmBe neutron source. Attenuation factors for the painted attenuator are presented relative to that of thick Cd where $A_{Cd} = 0.914 \pm 0.001$.

coats	T_{Gd}	$\frac{A_{Gd}}{A_{Cd}}$	$\frac{A_{Gd}}{A_{Cd}}$ of coat
0	0	0	0
1	0.687±0.002	0.342±0.002	0.342±0.001
2	0.508±0.002	0.539±0.002	0.286±0.001
3	0.458±0.001	0.593±0.002	0.108±0.001
4	0.418±0.001	0.637±0.002	0.096±0.001
5	0.340±0.001	0.722±0.001	0.203±0.001

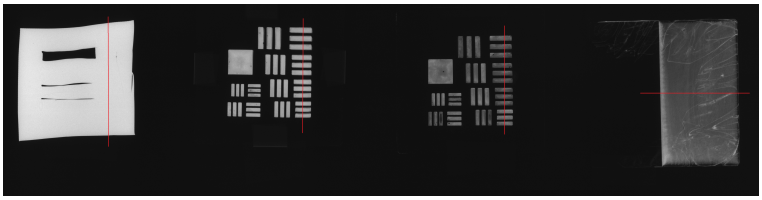

Figure 3.7: Approximated lines of interest selected for line profile comparison.

transmission for Cd to be virtually zero. As in the ^{241}AmBe experiment, attenuation is not exponential for multiple layers of paint. This may be caused by the presence of gammas and epithermal neutrons.

The radiographical film seen in Figure 3.7 is digitized and a contour plot of the gray scale value of each pixel is generated. This can be seen in Figure 3.8.

Table 3.3: Densitometer and neutron transmission measurements of test objects in Figure 3.7. The fog value of the film is found to be 0.12.

object	densitometer value	background	neutron transmission
Cd	0.77	2.78	24%
3 patterns	0.97	2.80	32%
1 pattern	1.37	2.80	47%
solid coat	1.63	2.75	57%

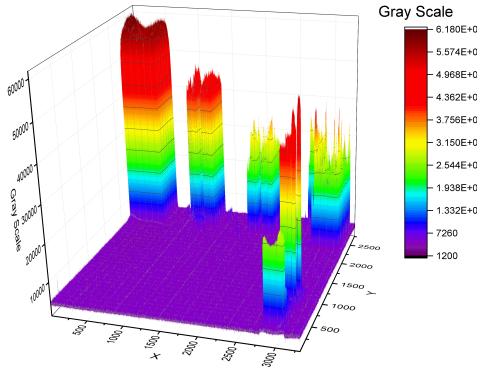

Figure 3.8: Contour plot of neutron radiographical images. The Z axis is the gray scale value of the corresponding pixel in the digitized film. The additional object in the bottom right quadrant is a Gd wire gauge provided by NRay Services and is not pictured in the film shown in this work.

The gray scale value of a pixel is proportional to the neutron beam attenuation through the object. By comparing the gray scale values for an object of interest to a Cd wafer one can get a measure of the neutron attenuation of the object with respect to Cd. This will mitigate the effect of epithermal neutron contamination in the beam and consequently the gray scale ratio of each object to Cd is an approximation of the thermal neutron attenuation factor. For each object in Figure 3.7 a line of interest is drawn across smooth looking regions for each test object, their line profiles can be seen in Figure 3.9.

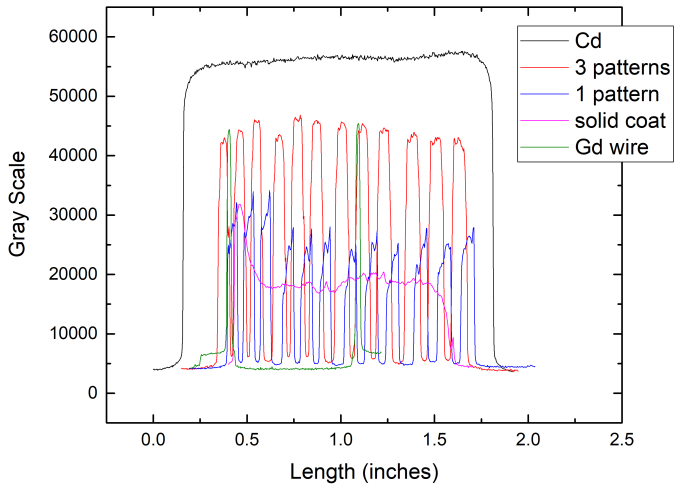

Figure 3.9: Line profile of gray scale values for test objects.

The gray scale values of each test object and a Gd wire are compared to Cd and summarized in Table 3.4. It is seen that the gray scale ratio for the 1 pattern object is greater than the ratio for the smooth single coat. It is expected that these to be similar since they are both a single application of paint on Al. This difference is likely due to different paint application methods. When painting the USAF pattern, the paint is dabbed on through a stencil. Here the paint fills the wells in the stencil and a thicker layer dries onto the substrate. The single coat object is painted in one motion with a foam brush resulting in a thinner layer applied.

At the McMaster Alignment Diffractometer the transmission factor of the shielding paint for 25 meV neutrons is determined. After analysis at the beam ports the sample layer thicknesses is measured using an optical Olympus BX51 upright microscope. The paint is scratched down to the substrate and the coating thickness is measured from the height difference between focal planes of the substrate and the

Table 3.4: Ratio of test object gray scale values to gray scale of Cd. This ratio approximates the thermal neutron attenuation factor.

test object	gray scale ratio to Cd
3 patterns	0.784±0.005
1 pattern	0.43±0.07
solid coat	0.34±0.02
Gd wire	0.86±0.02

paint surface. These values are used to calculate the attenuation coefficient and the area density of Gd. These results are summarized in Table 3.5 for a wide open (2x2 square inch) beam aperture. In Table 3.5, T_p is the neutron transmission through the paint calculated from $T_p = T/T_{Al}$ where T_{Al} is the transmission through the aluminum substrate and $T_{Al} = 0.981 \pm 0.002$. The wet density of the prepared Gd_2O_3 paint is needed to estimate the Gd area density expected after applying a wet coat of paint and its value is 7.407 $g \cdot cm^{-3}$. The Gd area density estimated for a wet paint ${}^{Gd}\rho_A^{wet}$ coat assumes that the transferred paint maintains a Gd_2O_3 mass fraction of

Table 3.5: Summary of results from MAD neutron transmission measurements, paint thickness measurements, and mass measurements.

Property	One Coat	Two Coats	Three Coats
wet mass [g]	1.33±0.02	2.70±0.14	3.49±0.15
${}^{Gd}\rho_A^{wet}$ [μmol cm^{-2}]	29.3±0.6	60±3	77±3
dry mass [g]	0.88±0.01	1.80±0.01	2.37±0.01
dry paint thickness [μm]	44±4	97±12	139±13
dry paint density [g cm^{-3}]	2.0±0.2	1.9±0.2	1.7±0.2
area density [mg cm^{-2}]	8.8±0.1	18.0±0.3	23.7±0.3
T_p	0.457±0.002	0.278±0.001	0.217±0.001
μ [cm^{-1}]	178±18	132±16	110±10
$\frac{\mu}{\rho}$ [g cm^{-2}]	89±2	71±1	64±1
${}^{Gd}\rho_A^{dry}$ [μmol cm^{-2}]	26.1±0.2	42.8±0.2	51.1±0.2

0.4. Using the transmission factor T_p, the dry area density ρ_A, and the paint thickness x, the attenuation coefficient μ (Equation (3.3.2)), the mass attenuation coefficient $\frac{\mu}{\rho}$ (Equation (3.3.3) where ρ is the dry paint density), and the area density of Gd in the dry film ${}^{Gd}\rho_A^{dry}$ (Equation (3.3.4) where n is the Gd number density and σ is the thermal neutron cross section for elemental Gd (49700 barns [37]) are calculated. To estimate the dry Gd area density it is assumed that all neutron beam attenuation through the paint is due to Gd atoms.

$$\begin{aligned} \mathrm{T_p} &= \mathrm{e}^{-\mu \mathrm{x}} \\ \mu &= -\frac{-\ln(\mathrm{T_p})}{\mathrm{x}} \end{aligned} \tag{3.3.2}$$

$$\begin{aligned} \mathrm{x} &= \frac{\rho_\mathrm{A}}{\rho} \\ \frac{\mu}{\rho} &= -\frac{-\ln(\mathrm{T_p})}{\rho_\mathrm{A}} \end{aligned} \tag{3.3.3}$$

$$\begin{aligned} \mu &= \mathrm{n}\sigma \\ \mathrm{n}\sigma &= -\frac{-\ln(\mathrm{T_p})}{\mathrm{x}} \\ {}^{\mathrm{Gd}}\rho_\mathrm{A}^{\mathrm{dry}} &= -\frac{-\ln(\mathrm{T_p})}{\sigma} \end{aligned} \tag{3.3.4}$$

In Table 3.5 it is seen that additional coats result in diminishing returns in their transmission factor. The first coat transmits 45.7% of thermal neutrons but the second coat transmits $27.8/45.7 = 61\%$ of neutrons and the third coat transmits $21.7/27.8 = 78\%$ of neutrons. This measurement might suggest that less paint is applied for each subsequent coating but this is not seen in the layer thickness measurements. It is important to note that the Gd area density differs between wet and dry coats. Since Gd_2O_3 is not volatile it is expected that the area density remain the same. This is

because the wet area density is calculated from mass measurements assuming that the Gd_2O_3 mass fraction of the applied paint remains 0.4 as it is in the bulk container. The dry area density is calculated from transmission measurements and is considered to be the more reliable calculation of the two.

To study the variance of the transmission across the width of the test sample the beam spot size is constricted to 1x1 cm^2 and the transmission profile is measured across the 10x10 cm^2 sample in 5 mm steps. Three profiles are taken of each sample near the top, middle and bottom of the painted square. The results of these measurements are summarized in Figure 3.10.

When a gaussian is fit to the transmission profile for the one coat and two coat samples a standard deviation of 0.06 and 0.03 respectively is calculated but this analysis fails for the three coat sample. The three coat sample transmission profile is poorly fitted by a gaussian distribution so instead the standard deviation is directly calculated from the data set by the usual expression. The mean transmission across the three profiles for each sample is seen in Figure 3.11. The standard error on the mean is calculated by $\sigma_{\bar{x}} = \frac{\sigma}{\sqrt{N}}$.

The three coat transmission profiles in Figure 3.10 show a larger transmission factor near the top of the sample suggesting that one or more coats are not applied evenly with the foam brush. This uneven application would explain the poor gaussian fit for this sample. Other application methods may result in more consistent coatings.

3.4 Conclusions

In this work it is shown that a Gd_2O_3 oxide paint is an effective attenuator of thermal neutrons. In each application of the paint in this experiment significant neutron attenuation is observed. For a single coat of paint we found that when shielding a wide-spectrum ^{241}AmBe source a transmission factor of T = 0.687±0.002 is measured. In a neutron radiography beamline a neutron transmission of T = 0.57 is observed. At the McMaster alignment diffractometer a thermal neutron transmission factor of $T = 0.457 \pm 0.002$ is observed. From these observations it is concluded that 1–3 coats of paint can effectively augment the neutron shielding properties of a material in wide-spectrum applications and can be a space efficient thermal neutron attenuating additive to multi-layer shielding. Because the paint maintains its robust properties even with large amounts of oxide additive (40% by mass) it is also concluded that it can be useful in producing neutron attenuating objects at intermediate length scales ($\sim$ 1 mm) cheaply without requiring specialized machining facilities willing to cut Gd or Cd.

It is observed that there are diminishing returns for additional coats of paint. It is seen in Figure 3.5 and Table 3.3 that a smaller proportion of neutrons are attenuated by each additional coat of paint which might suggest that each additional coat of paint is applied thinner than the coat before. However when the thickness of the painted samples is measured it is observed that the coat thickness is consistent at 40–50 μm per coat. This suggests that the difference in transmission is due to less oxide transferred to the sample. This is also reflected in the increasing mass attenuation length for additional coats and the difference between the measured Gd area density and the estimated area density in the wet coat derived from gravimetric

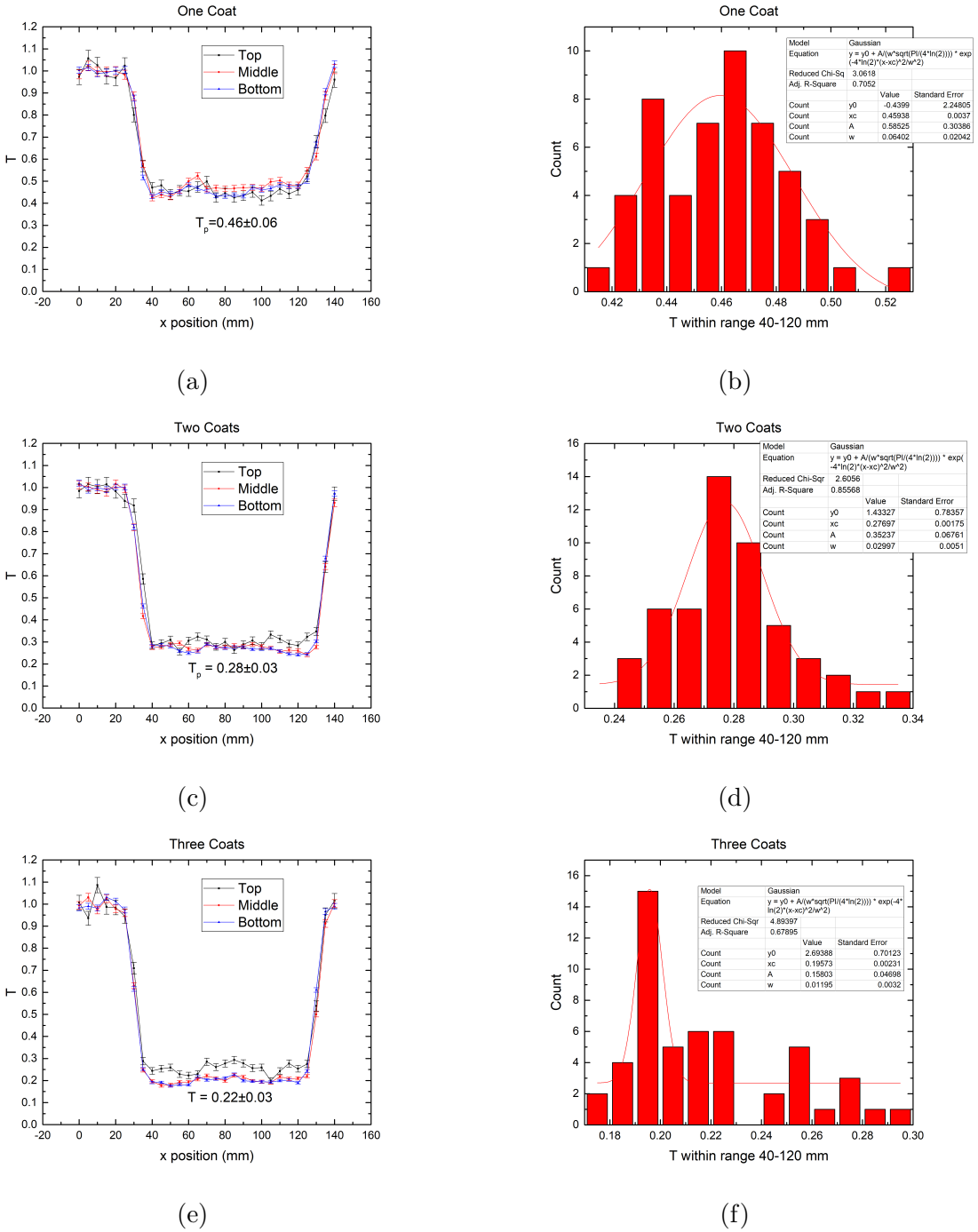

Figure 3.10: Transmission profiles across oxide paint samples. Beam spot size is 1x1 cm^2 and is scanned across each sample in 5 mm steps. The first 5 data points of each are averaged to measure T_{Al}. The first and last centimetre of the paint profiles are neglected because of edge layer irregularities.

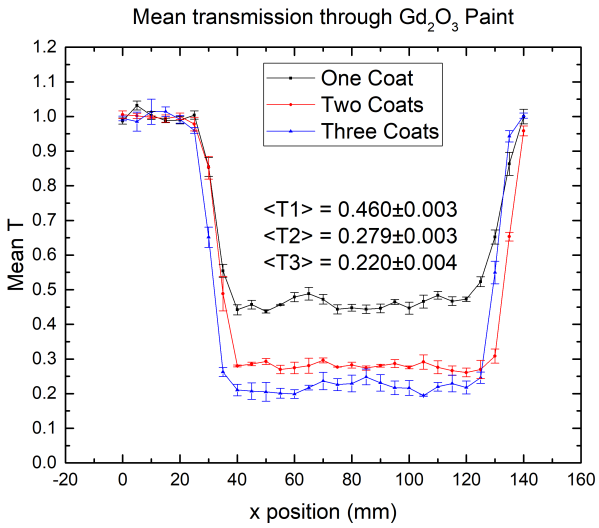

Figure 3.11: Mean transmission profiles for oxide paint samples of varying thickness.

measurements in Table 3.5. Diminishing neutron attenuation by additional coats may be explained by the application method. The oxide is clingy and tends to clump to itself and materials that touch it. The base paint, polyurethane is thin and must be mixed immediately before application to ensure even distribution of the oxide. It is suspected that the oxide clings to the foam brush during application, reducing the oxide density of the applied paint. It is suspected that other application methods such as wire brushes or screen printing may result in better agreement between wet and dry Gd area densities. Selecting a denser paint base such as shellac may also improve upon this with the additional benefit of a longer oxide settling time in the paint. Future work with this paint should investigate if this behaviour is maintained for different application techniques such as screen printing.

Chapter 4

Imaging a resolution standard

Neutron imaging is a powerful method of non-destructive imaging that can be used in diverse fields such as industrial quality assurance, archeology and scientific research [63]. Because neutrons carry no charge they are able to penetrate deeply into even dense materials such as lead and other metals. This property may make neutrons a useful probe for border security application in the search for SNM and other unsecured radioactive materials. There is a growing concern in the international community regarding increasing incidents of radioactive materials trafficking and there is a demand for security devices which can reliably detect SNM and controlled radioactive substances [10, 9]. Efficiently probing large vehicles and containers with neutrons requires a large area system but such systems may be prohibitively expensive and the primary fill gas used in gaseous neutron detection systems, ^{3}He, cannot be produced at a sufficient rate to meet demand [13]. In this work a prototype for a novel digital neutron imaging system is presented. This system is composed of cost effective components such that the system can be scaled to large areas or paneled together in a modular configuration.

4.1 Description of imaging instrument

This work builds on the prototype data acquisition system and delay line readout developed by Hanu *et al.* [45]. A picture and schematic diagram of the detector assembly used in this work is seen in Figure 4.1.

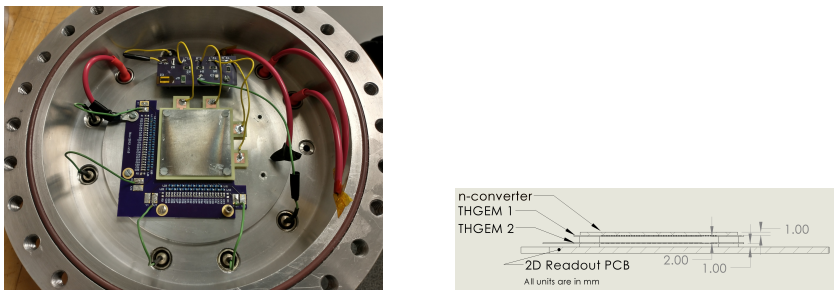

(a) (b)

Figure 4.1: Picture of assembled detector with no lid (a) and schematic of detector stack (b).

Instead of using a fill gas sensitive to neutrons such as ^{3}He, a solid state neutron converter is used. The neutron capture products from this converter then ionize the 760 torr P10 (Ar[90%]/CH_4[10%]) fill gas to produce free charge pairs for amplification. When selecting a converter material several isotopes with a high neutron capture cross section were considered. These isotopes include ^{157}Gd (259,000 barns), ^{6}Li (960 barns), and ^{10}B (3835 barns) [37]. Because ^{157}Gd has the highest neutron capture cross section in nature it is an excellent potential candidate because one would expect it to have superior conversion efficiency. The problem with using ^{157}Gd is that the neutron capture products are primarily gammas and internal conversion electrons which have relatively low ionization densities in gas. Long ionization tracks or ionization occurring far from the converter will smear the image, so heavy ion products which have a high ionization density are preferred. ^{6}Li has a lower cross section than

^{10}B but produces higher energy products. The issue with ^{6}Li is that it is a source of tritium for nuclear fusion and has other applications in the nuclear industry so it is heavily regulated and difficult to acquire. Because ^{10}B has a high cross section, it produces energetic alpha and ^{7}Li capture products, and is unregulated, it was selected for the converter. In cooperation with the European Spallation Source, 3.2 μm thick microlayers of ^{10}B enriched boron carbide on 1 mm thick Al-5754 substrates were acquired for use as a converter.

Neutron capture products exiting the converter surface are either stopped by copper or exit into the gas within the holes of the THGEM amplification region. Charge amplification is performed by two vertically aligned THGEMs to achieve a gain of $\sim 10^4$ [45]. THGEMs are a large scale variant of the GEM seen in micropattern gas detectors produced by drilling thousands of small holes in a copper clad PCB material. The selected PCB material is FR-4, a glass and epoxy laminate material which is a common dielectric in the PCB industry. THGEMs have the benefit of physical robustness over their much more fragile counterparts, they are relatively cheap to produce and can be manufactured by commercial PCB manufacturers. Most importantly for position sensitive applications, charge amplification is contained within the THGEM holes, constraining the positional distribution of charge induced on the readout board. Because the final resolution of the imaging system will depend on the size and pitch of these holes and a sub mm resolution is desired the chosen THGEM dimensions are 0.4 mm holes drilled into copper clad 0.4 mm thick FR-4 with pitch of 0.8 mm. An example of THGEMs used in this work is seen in Figure 4.2.

The 2D delay line readout is seen in Figure 4.3. It is an array of diamond shaped copper pads connected to a $Z_0 = 50\ \Omega$ passive delay line made of ferrite core and

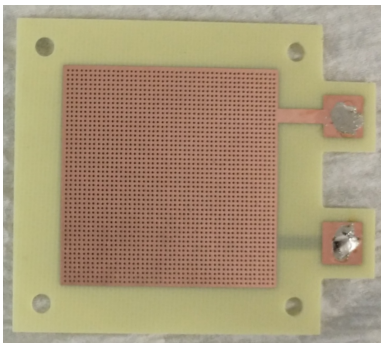

Figure 4.2: THGEM with active area 38.5x38.5 mm^2, 0.4 mm diameter holes with pitch 0.8 mm drilled. Copper tabs were used as solder contacts to bias the THGEMs.

wirewound L = 75 nH inductors, and ceramic C = 30 pF capacitors. Each delay line is connected to a row or column of pads connected via internal layer traces, and corresponds to either an X or Y axis coordinate for a given event. Signals induced on a group of pads travel down to either end of each delay line such that the coordinate can be reconstructed from the difference in arrival time. Each delay line has 32 LC cells with a nominal delay of $t_d = \sqrt{LC} = 1.5\ ns \cdot cell^{-1}$. It is expected that the total delay of each line is $32 \times 1.5 = 48\ ns \cdot cell^{-1}$ however when the full delay is measured with a BNC PB-5 pulser and desktop digitizer it is seen that the real length is 58 ± 2.5 ns. This is likely due to stray capacitance between copper traces and the diamond pads. An electrical diagram of a delay line cell is seen in Figure 4.4.

The pulse processing chain is composed of Ortec VT120a fast timing preamplifiers, a set of five Texas Instruments OPA657 based homemade pulse amplifiers with input/output impedance of 50 Ω, and a CAEN DT5743 desktop digitizer. The DT5743 digitizes (sampling period 625 ps) the four delay line signals from the pulse amplifiers and using software defined constant fraction discrimination, measures their arrival time relative to a trigger signal originating from the bottom THGEM. The X and

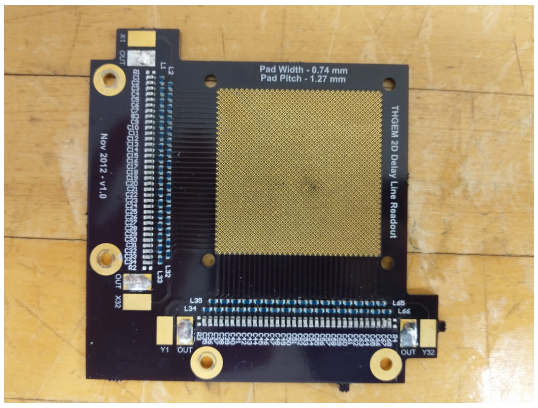

Figure 4.3: 2D delay line readout with 32 delay cells.

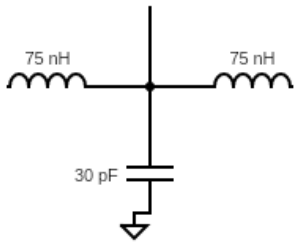

Figure 4.4: Electrical diagram of a single delay line cell.

Y coordinates are then reconstructed from timing measurements using an algorithm written in Python. An example coincidence event as seen in the CAEN Wavecatcher software is seen in Figure 4.5.

In Figure 4.5 each of the five output signals is seen: the trigger signal (red), X-left (dark green), X-right (light green), Y-left (purple), and Y-right (pink). The pulse processing chain leading to the digitizer includes the non-inverting VT120 preamplifiers and the inverting OPA657 pulse amplifiers. The trigger signal is filtered by the pulse amplifier but bypasses the amplification portion of the circuit, this is to avoid pulse heights exceeding the limit of the CAEN DT5743 input voltage. Periodic high frequency noise is seen in the trigger signal due to a fault in the OPA657 device,

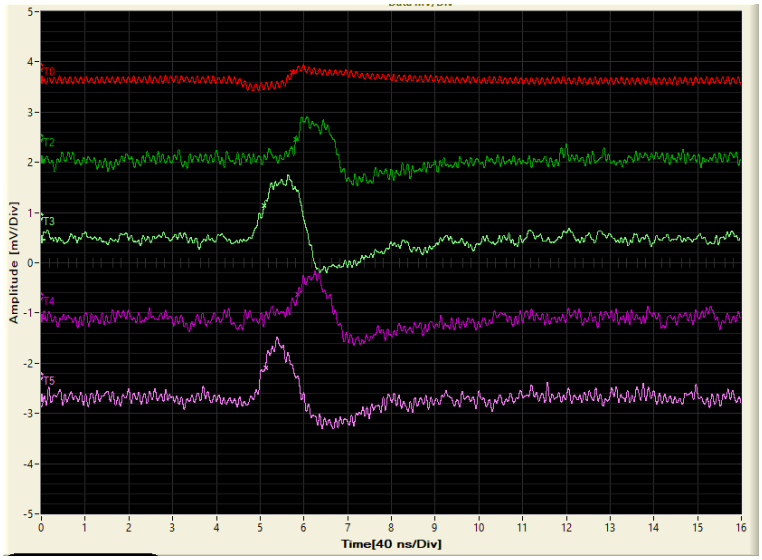

Figure 4.5: Coincidence event as seen in the CAEN Wavecatcher software. Timing pick off is displayed with an x on the rising edge. The digitizer sampling period is set to 625 ps.

however since this signal is only used for trigger logic and not timing, it does not negatively impact the imaging results. The coincidence window is set to 250 ns, the trigger logic is (TRIG AND (X-left AND X-right) AND (Y-left AND Y-right)). The CAEN Wavecatcher software includes a software implementation of CFD timing, the timing pick off is displayed on the signal with a $\times$ on the rising edge. The software outputs timestamps relative to the coincidence trigger to a text file. Python code was written to implement the following image reconstruction procedure.

1. Load text file and extract timestamps from axis signals into a set of four arrays.

2. Subtract arrays to calculate the timing difference between each end of delay line

   $\Delta X = XL - XR,\ \Delta Y = YL - YR$

3. Define image boundaries by measured delay line length.

4. Define bin edges by dividing delay line length by N where N is the desired number of pixels in the NxN image.

5. numpy.histogram2d automatically bins the Δ values into a 2D histogram which is displayed as an image by matplotlib.

6. (Optional) Repeat steps 1–5 for a flat field image. Apply flat field correction as described in the analysis section.

4.2 Experiment

Measurements were performed at the McMaster alignment diffractometer (MAD) [62], a neutron diffraction instrument situated at beam port six of the McMaster Nuclear Reactor (MNR). The MAD is a general purpose triple-axis instrument that can be used to measure large angle neutron diffraction from samples in single crystal, polycrystalline, and powder form. It is primarily used for sample alignment and the evaluation of crystal quality. The MAD can produce a collimated beam of thermalized neutrons originating from the reactor pool by using a single crystal of silicon to select ~ 25 meV neutrons from the reactor beam port. The MNR is also home to dedicated neutron imaging radiography beamlines however their specialized and enclosed setups, and heavy usage schedules, make them prohibitively difficult to utilize for this work. It is desired that the spatial intensity of the beam spot size be relatively constant so in cooperation with Nray Services Ltd., a radiographical image of the neutron beam spot at the MAD sample stage was taken. The results and analysis of this is seen in Figure 4.6. It is seen that the intensity varies within the beam spot along a diagonal. When a gray value profile across this feature is measured as seen in Figure 4.7 it is

seen that the gray value changes by approximately 8000 across this diagonal feature. Since the gray value is proportional to the thermal neutron intensity it is concluded that the neutron intensity varies by as much as 45% in the selected region. This is not an ideal beam property for neutron imaging, however techniques such as flat field correction may be used to mitigate the effects of beam spatial variance.

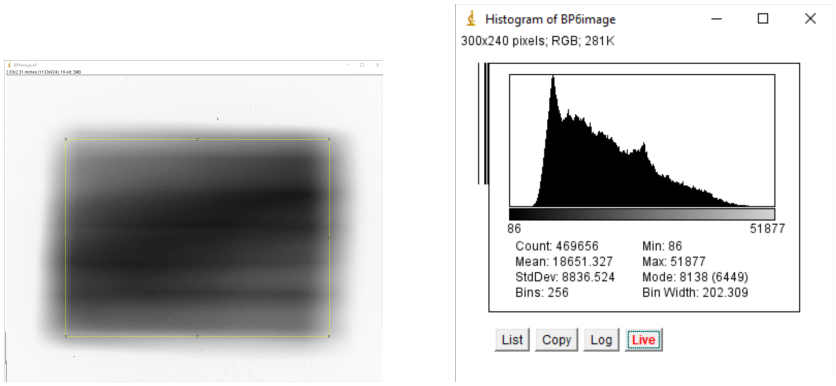

(a) (b)

Figure 4.6: Radiograph taken at the MAD sample stage (a) and gray value histogram (b).

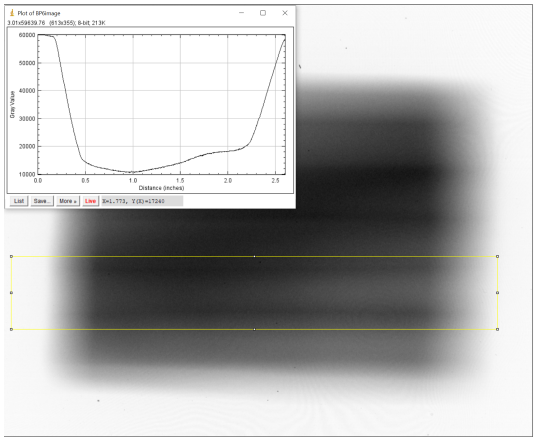

Figure 4.7: Line profile along X-axis of selected area of beam spot radiograph.

The image object is a resolution standard cut into a 1 mm thick Cd wafer by a commercial machine shop. The standard is a pattern derived from the United States

Air Force 1951 image resolution standard [60]. A technical drawing of the sample can be seen in Figure 4.8.

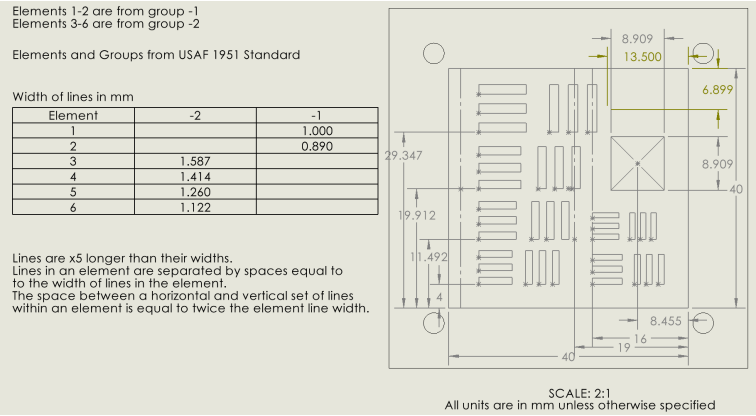

Figure 4.8: Technical drawing of the USAF 1951 derived resolution standard produced with the shielding paint [60].

4.3 Results and Analysis

Two measurements were performed at the MAD. The first image collected was a full exposure of the assembly and readout. This is the flat field image used to correct for beam intensity variances and readout pixel variances. The collection time of all images discussed here is 3 hours. In each case the event collection rate was limited by the data transfer rate of the digitizer. The coincidence event rate becomes saturated at 500 events·s^{-1}. The second image included the Cd USAF-1951 derived resolution standard. The flat field image and uncorrected sample image is seen in Figure 4.9 and the corrected image is seen in Figure 4.10.

A flat field correction is a standard calibration technique for digital imaging systems. It is performed by taking the sample image and multiplying it by the normalized flat field image (see Equation (4.3.1) where C is the corrected image, F is the flat

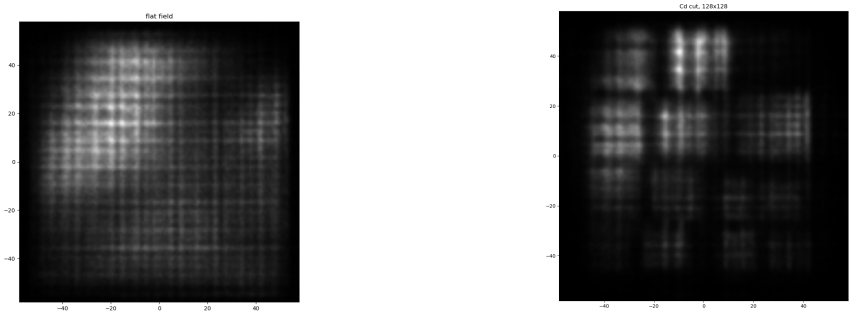

(a) (b)

Figure 4.9: Flat field image (a) and uncorrected sample image (b).

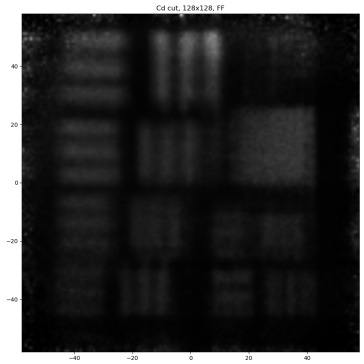

Figure 4.10: Flat field corrected sample image.

field image, U is the uncorrected image and $|F|$ is the mean pixel value of the flat field). A flat field image is an exposure of the sensor system without a sample object. Ideally this exposure should be with a spatial, angular, and energetically uniform source. Typically, a flat field correction will also contain terms for the so-called dark current however this is not a significant factor in this instrument. The dark current is a factor in photosensitive devices; a small current produced when the device is not illuminated. Dark current is the source of many noise features in optical instruments.

This instrument operates by coincidence measurements of four position signals and a trigger signal so the event rate becomes negligible when it is not exposed to neutrons. The dark current contribution to the image can therefore be neglected.

$$C = \frac{|F| \cdot U}{F} \tag{4.3.1}$$

Features in Figure 4.10 can be used to determine length/pixel calibration factors m and image resolution σ. Line profiles can be drawn across the triplet rectangular elements to measure the length/pixel calibration factor along the X and Y axis. Example calculations are seen in Figure 4.11. The full table of values and calibration factors are seen in Table 4.1.

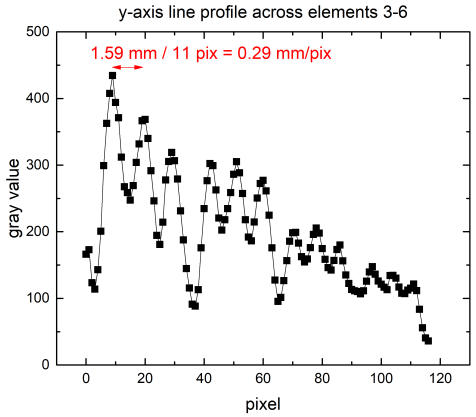

Figure 4.11: Line profile across standard elements 3-6. Noted in red is a sample calculation of the Y-axis length/pixel calibration factor.

The point spread function (PSF) of any imaging system is a measure of its response to a point source and can be used to determine the resolution of the system. For a point source with real diameter much smaller than the pixel size of the detector, the

Table 4.1: Calibration factors measured by peak to peak distances across line elements. $\langle m_Y \rangle = (0.32 \pm 0.02)$ mm $\cdot$ pix^{-1} and $\langle m_X \rangle = (0.33 \pm 0.02)$ mm $\cdot$ pix^{-1}.

Element	Pitch (mm)	m_Y (mm/pix) Peak 1–2	Peak 2–3	m_X (mm/pix) Peak 1–2	Peak 2–3
3	3.17	0.29	0.35	0.32	0.32
4	2.83	0.31	0.31	0.31	0.35
5	2.52	0.36	0.32	0.32	0.32
6	2.24	0.32	0.32	0.37	0.32

diameter of its image spot size is a measure of the system resolution. One could produce a neutron point source by drilling a very small hole in a cadmium wafer but with this instrument and beam source the event rate would be too low to be practical. Instead, an approximation of the PSF using the edge spread function (ESF) technique [64] is calculated. The ESF is determined from the gray value profile across an illuminated straight edge. By differentiating across the ESF the PSF is approximated. The width of the differentiated data is then a measure of the system resolution. The line profile and differentiation along the Y-axis across the square feature can be seen in Figure 4.12. A similar analysis is seen along the X-axis in Figure 4.13 however image artifacts smear one edge of the square feature. Because of this smearing this edge is ignored and instead straight edges from element 6 are used to take a measure of the ESF and PSF. A table of full width at half maximum (FWHM) values of the PSFs for various features are seen in Table 4.2. Multiplying the mean FWHM values by the calibration factor results in the X and Y axis resolutions:

$$\langle \sigma_X \rangle = (1.37 \pm 0.24) \text{ mm}$$
$$\langle \sigma_Y \rangle = (1.15 \pm 0.13) \text{ mm}$$

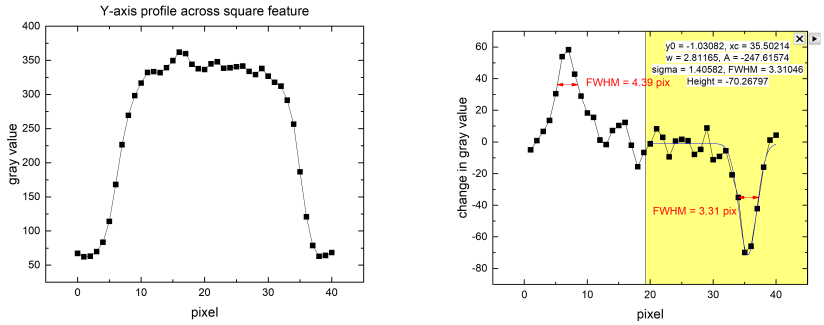

(a) (b)

Figure 4.12: Y-axis profile across 8.9 mm wide square feature (a) derivative and gaussian fit of feature upper edge (b).

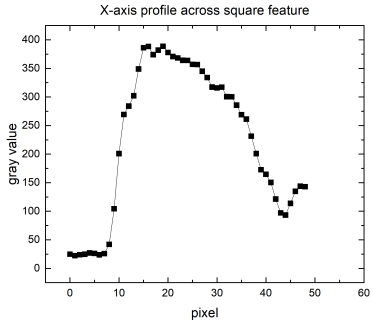

Figure 4.13: X-axis profile across 8.9 mm wide square feature.

4.4 Discussion of imaging results

Several image artifacts are seen in Figure 4.10 which are likely the result of flat field correction. While image quality is improved in terms of pixel-to-pixel noise and overall clarity there are also artifacts appearing in the corners which obscure sample features. The pixelated blurring in the upper left corners is likely due to the beam spot size not fully illuminating the readout board in the flat field image. In Figure 4.9 it is seen that the flat field image is darkened at the upper left which supports this, indicating misalignment of the readout and the beam center. The beam spot size in Figure 4.6 is approximately 5.8x4.3 cm^2 compared to the effective area of the THGEM which

Table 4.2: Table of PSF FWHM values from various straight edge features. The mean values for the PSF FWHMs are determined to be $\langle \mathrm{FWHM_Y} \rangle = (3.55 \pm 0.31)$ pix and $\langle \mathrm{FWHM_X} \rangle = (4.19 \pm 0.66)$ pix

feature	FWHM (pixels) X-axis		feature	FWHM(pixels) Y-axis	
square	5.50		square	4.47	3.28
element 3	5.83	3.28	element 4	3.11	3.32
element 6	4.02	2.30			

is 3.85x3.85 cm^2. In the upper right corner it is also seen what may be a reflection of the square feature. Blurring between elements such as between horizontal element 4 and the square feature may also be a reflection. The delay line was designed with a 50 Ω characteristic impedance to match the transmission lines and avoid artifacts caused by reflections. To check this the neutron converter was replaced a ^{241}Am alpha source approximately 7 mm above the top of the first THGEM and collected an image. In Figure 4.14 an example event as measured by an oscilloscope is seen without a reflected pulse. The corresponding image is seen in Figure 4.15.

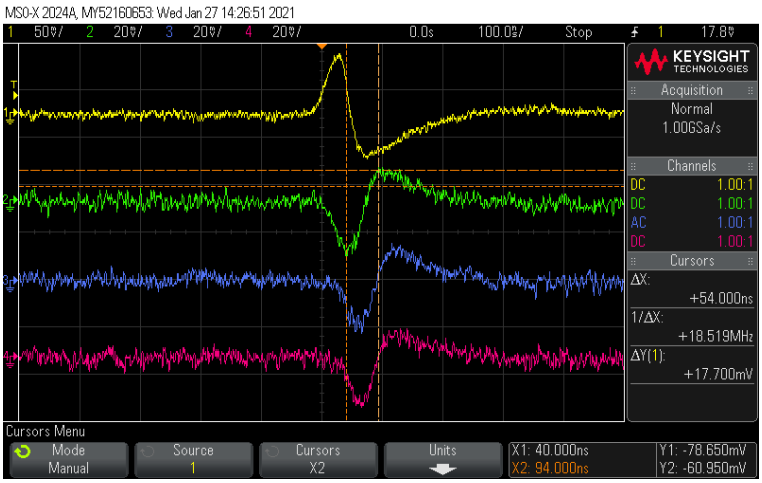

Figure 4.14: Preamplifier output of trigger (yellow), X-axis left (green), X-axis right(blue), and Y-axis left (red).

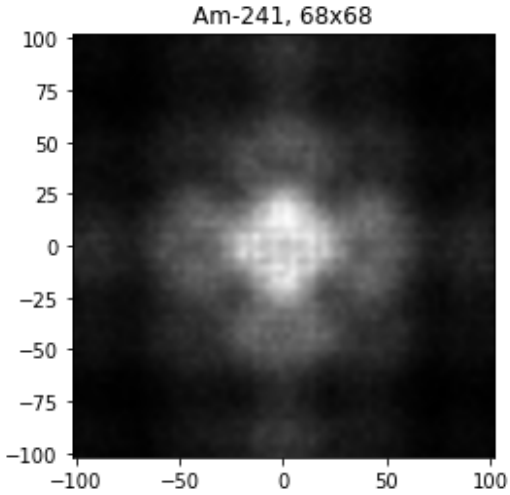

Figure 4.15: Image collected from an ^{241}Am alpha source illuminating a spot at the center of the 2D readout.

In the image a diamond shaped central spot surrounded by 4 reflections is seen with 2 reflections along each axis. These artifacts are laid over a low intensity background outlining the array. This background is likely due to gamma products from ^{10}B neutron capture events. The full delay length of the array is 58 ns and its edges can be seen at $\pm$58 ns along the X and Y axis but there are what appear to be reflection artifacts extending beyond this length. The cause of these artifacts is unclear because signal reflections are not seen in the preamplifier output. Further work needs to be done to identify the source of these artifacts.

The X and Y resolutions were found to be in agreement within experimental uncertainty however they varied over the image and the value of $\langle\sigma_Y\rangle$ is slightly less than $\langle\sigma_X\rangle$. This difference is likely due to stray capacitance between internal traces and the readout pads. Traces on the uppermost internal layer closest to the pads will feel a greater effect than deeper traces. Placing a ground plane between the readout pads and traces may mitigate this effect. Despite THGEM and readout pad

dimensions being under 1 mm, the resolution is still greater than 1 mm. This is likely due to image smearing caused by long tracks of energetic alpha and ^{7}Li capture products in 760 torr P-10 gas. To reduce effects caused by smearing of the signal the converter was placed flush against the top of the first THGEM. A single THGEM configuration may mitigate this but it has reduced gain and the signal-to-noise ratio becomes too poor to be practical for imaging. A simple geometric calculation where a point source situated at the top of a hole in the top THGEM will form a cone with a maximum base diameter of 2.4 mm on the bottom THGEM set 2 mm below the top. This cone can be reduced by decreasing the distance between THGEMs however when this was attempted below 2 mm high voltage discharges and visible damage to the detector was observed. Novel THGEM designs produced from multilayer PCBs [65] would prevent image smearing caused by ion tracks between THGEMs. Resistive THGEMs may also improve image results by allowing for higher gain from a single amplifier. Future instruments designs should investigate the use of these components.

Chapter 5

Discussion and Conclusions

5.1 Further discussion of imaging results

When comparing the performance of a 20 cell readout with pad width 1.00 mm and pitch 1.70 mm, and a 32 cell readout with a pad width 0.74 mm and pad pitch 1.27 mm a drastic improvement in resolution is observed. Using a similar technique used to evaluate the 32 cell readout board discussed in Chapter 4 the length·pixel^{-1} calibration constant and resolution are determined. Using the USAF-1951 derived Cd sample described in Chapter 2 the pixel width of the 8.9 mm wide square feature is measured to calculate the calibration constants $m_X = 1.1 \pm 0.1$ mm·pix^{-1} and $m_Y = 1.2 \pm 0.2$ mm·pix^{-1} (see Figure 5.1). By imaging the edge of a 1 mm thick Cd wafer the ESF is measured and from its derivation the PSF is obtained (see Figure 5.2). These are the system response to a sharp edge and an approximation of the system response to a point source respectively. From the width of the PSFs and their corresponding axis calibration factors the X and Y axis resolutions for the 20 cell readout board are obtained. Resolution and calibration factors for the 20 cell board are determined

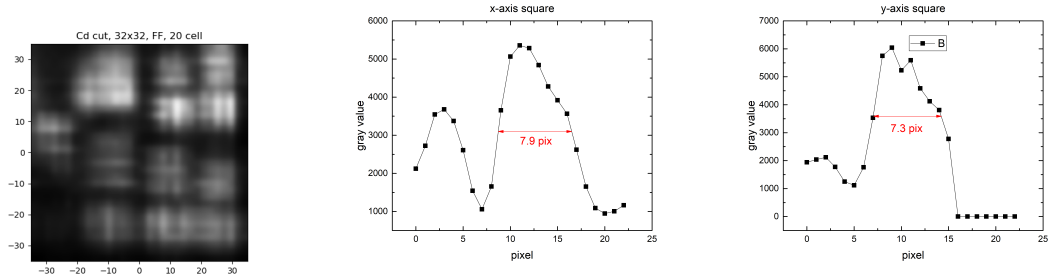

(a) Image of Cd sample.

(b) X-axis gray value profile across square.

(c) Y-axis gray value profile across square.

Figure 5.1: Image of USAF-1951 derived Cd sample and profiles over 8.9 mm wide square feature.

from 32x32 images instead of 128x128 board images to reduce digital noise artifacts. Increasing pixel density does not significantly improve the measured resolution for the 20 cell readout.

$$\sigma_{X20} = (4.4 \pm 0.6) \text{ mm and } \sigma_{Y20} = (2.4 \pm 0.3) \text{ mm} \tag{5.1.1}$$

$$\langle \sigma_{X32} \rangle = (1.37 \pm 0.24) \text{ mm and } \langle \sigma_{Y32} \rangle = (1.15 \pm 0.13) \text{ mm} \tag{5.1.2}$$

When images of the USAF-1951 Cd standard taken with each readout board are compared we see a distinct difference in digital noise. Figure 5.3a and Figure 5.3b contain the same data but are binned into a 32x32 image and a 128x128 image. Both images exhibit black crosshatch lines caused by the lack of data with timing that would fall *between* delay line cells. This effect is caused both by the discrete pad structure of the readout board and the square pattern of THGEM holes. These artifacts do not appear to be present in the image taken with the 32 cell board because flat field correction was able to smooth out the pixel-to-pixel inconsistencies. This effect is most prominently seen in the triplet element sample features which are all

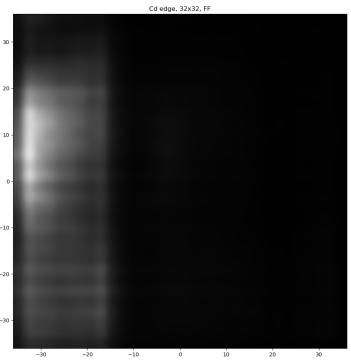

(a) Flat field corrected image of the edge of a Cd wafer to measure the x-axis ESF.

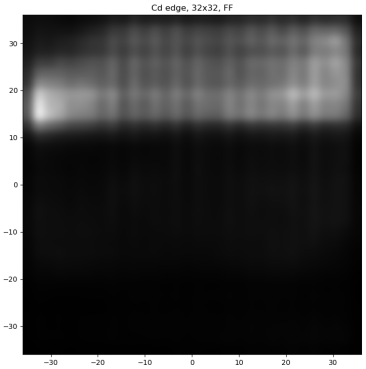

(b) Flat field corrected image of the edge of a Cd wafer to measure the y-axis ESF.

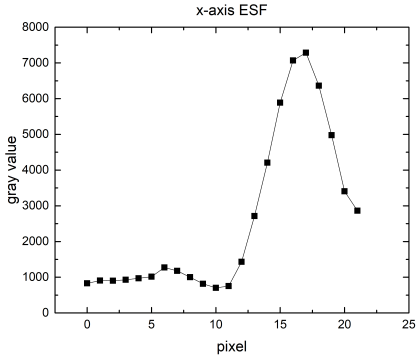

(c) X-axis ESF.

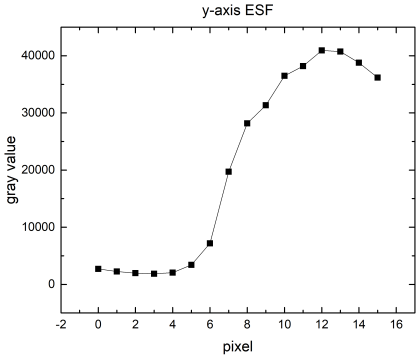

(d) Y-axis ESF.

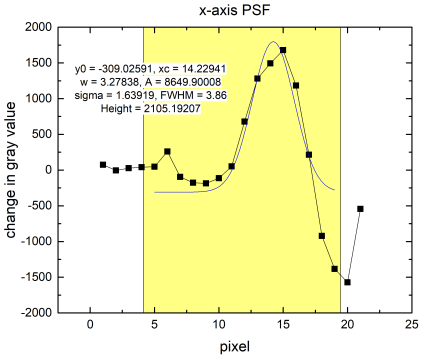

(e) X-axis PSF.

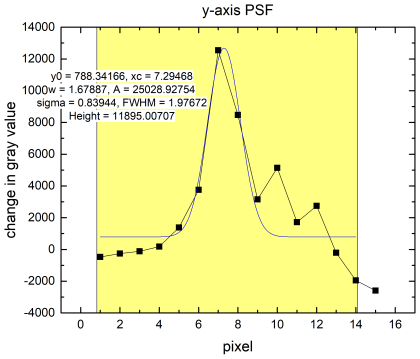

(f) Y-axis PSF.

Figure 5.2: Images, ESFs and PSFs for the straight edge of a Cd wafer.

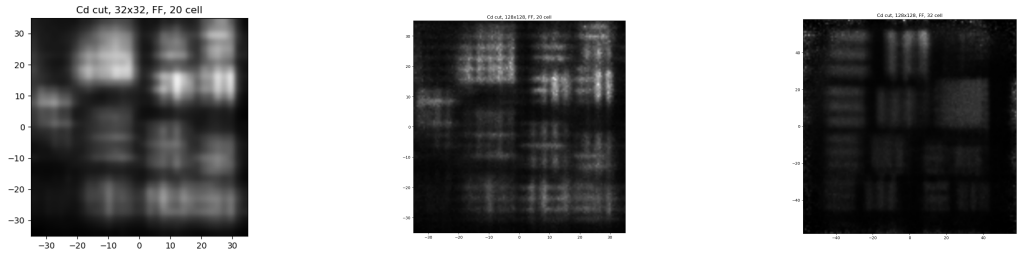

(a) 32x32 pixel corrected image with 20 cell board.

(b) 128x128 pixel corrected image with 20 cell board.

(c) 128x128 pixel corrected image with 32 cell board.

Figure 5.3: Image comparison of 20 and 32 cell readout boards.

below 1.70 mm in thickness. 1.70 mm is the pitch of the 20 cell board so it may be the fact that all sample elements have dimensions smaller than the pitch of the readout board which causes these noise artifacts. The 32 cell board has a pad pitch of 1.27 mm and these noise artifacts are not apparent after flat field correction.

It is observed that in both readout boards the X-axis has worse resolution than the Y-axis. As discussed in Chapter 4 it is believed that this is due to stray capacitance between the pads and the upper layer of internal traces. This effect is observed in the aspect ratio of sample elements. As specified in the USAF-1951 standard, elements should have a length five times greater than their width. However when the length and width of bottom horizontal element 4 is measured in Figure 5.3c it is observed that they are 22 ± 1 pixels long by 6 ± 1 pixels wide. This is a feature aspect ratio of $3.7 \pm 0.6 : 1$; the length of the feature appears contracted along the x-axis.

In Figure 5.4 the Gd_2O_3 painted sample and the Cd sample images are compared. The painted sample is three stacked painted wafers; the same sample used in Chapter 3. The uncorrected images are used because when flat field correction is attempted on the painted sample image the image quality worsens and many features become indistinguishable from background. This may be the result of changes in the beam

profile between the flat field and image collection times when they are taken many days apart. As discussed in Chapter 3 the attenuation of three coats of the shielding paint is effective at producing image contrast but less effective than Cd. In Figure 5.4 gray value profiles are compared across the 8.9 mm wide square feature and a significant difference in gray value feature to background contrast is observed. When the paint was produced and tested, we did not have a Cd sample and the paint was expected to be our primary contrast medium. It is seen here to be less effective than Cd as we expect and we conclude that for a painted sample to be a resolution standard with comparable effectiveness to Cd a more intense neutron beam is required to improve counting statistics and image contrast. Some loss of contrast may be due to reflections into the dark regions of the image. As seen in many of these images and discussed in Chapter 4 we observe large signal reflections in bright features. Since bright regions in Figure 5.4b correspond with negative space on the sample, reflections are expected to extend into dark sample feature regions, reducing feature contrast.

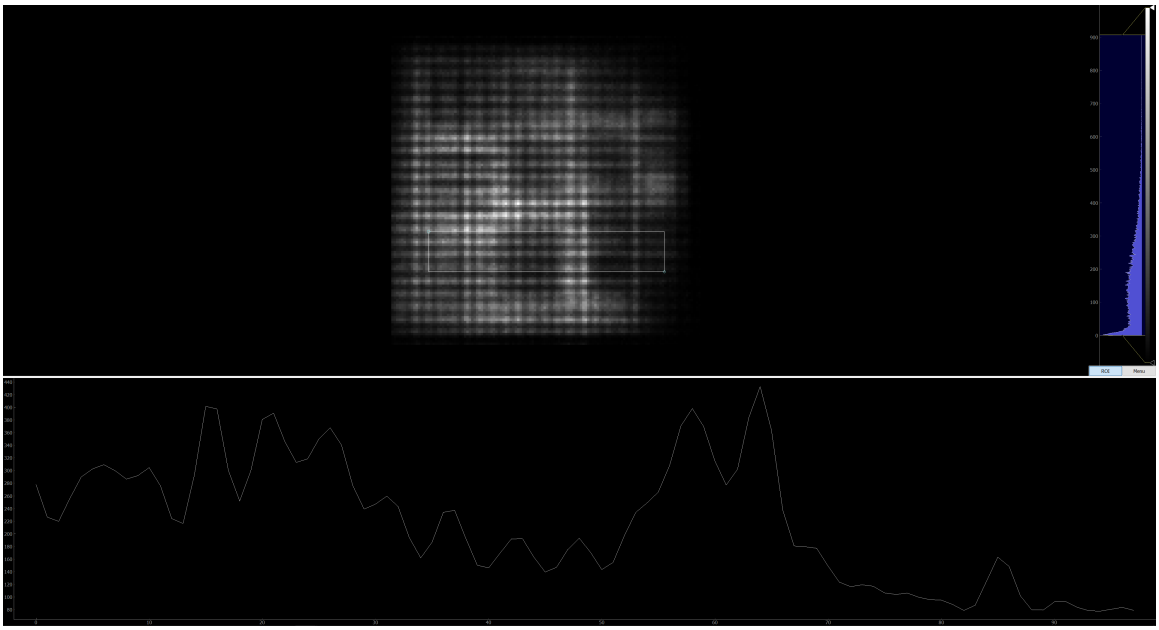

(a) 128x128 uncorrected image of Gd_2O_3 paint sample.

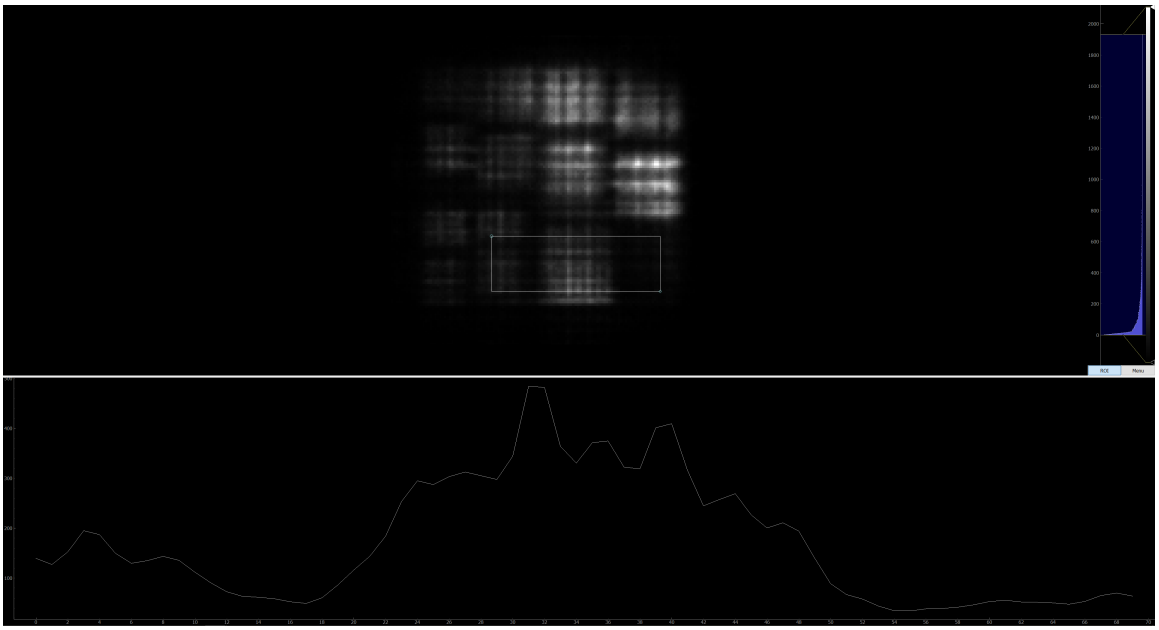

(b) 128x128 uncorrected image of Cd sample.

Figure 5.4: Comparison of Gd_2O_3 painted sample and Cd sample.

5.2 Conclusions

In this work a proof of concept is successfully demonstrated for a novel digital neutron imaging system. The capability to take images with moderate resolution sufficient to probe object features with linear dimension greater that 1.5 mm using simple and scalable components is demonstrated. The next step in this project should be to prepare the prototype for scalability and to produce a truly modular prototype that can be tiled or otherwise arranged with similar modules. A consistent issue in these images taken using a CAEN digitizer is the limitation imposed by data transfer rates. The total coincidence event rates are capped at about 500 events·second^{-1} and when using the optical transfer communication card the data collection PC would often crash after several hours. Adapting the original hardware implementation of the TDC-DAQ to modern instrumentation would allow for greater event rates and improved counting statistics and contrast. From this point the issue of reflections may be easier to investigate or it may be discovered to be an artifact of using the desktop digitizer.

The resolution of the imaging system may be improved by increasing the pad density of the readout, introducing a ground plane below the readout array to reduce the effect of stray capacitance on the interior traces, and reducing the width of the transfer region between subsequent THGEMs. A 51 cell readout board design was attempted but because of manufacturing constraints we were unable to produce a design with a ground plane protecting the interior traces. Future designs should be developed in cooperation with PCB manufacturers in order to introduce a ground plane. Recent advancements in THGEM systems may prove useful in future iterations of this instrument. Cortesi et al. [66] have reported that the inclusion of resistive anodes after

the amplification stage improves image resolution by decoupling the readout board from the amplification stage. A novel design for a multilayer THGEM manufactured from 4-layer PCBs has been shown to be comparably effective to detached THGEM designs but lack transfer regions [65]. In such a design, secondary ion tracks are fully contained within amplification holes of the multilayer THGEM and it is expected that such a device would reduce feature broadening by this effect and improve resolution. The use of resistive thick gas electron multipliers (RETGEMs) should also be investigated. These are THGEM designs which use a resistive material such as graphite paint or resistive Kapton instead of copper cladding. This resistive material protects the THGEM from high voltage discharge damage and it has been reported that resistive THGEMs can achieve 10 fold higher gains than their non-resistive counterparts [67]. To improve the neutron conversion efficiency, future designs may make use of multiple conversion layers in a dual-sided or stacked design. Future designers may also consider conversion layers on a contoured surface to increase single layer efficiency.

Appendix A

PCB schematics

This appendix will include electrical and board schematics for various PCBs designed and manufactured for the project presented here. Since this project builds off the PhD thesis of Dr. Andrei Hanu [43] we will not include drawings and schematics for any re-used components. Drawings and schematics for the detector chamber, the chamber lid, pulse amplifiers, readout boards, as well as code for FPGA firmware and MATLAB software can be found by referring to the prior work.

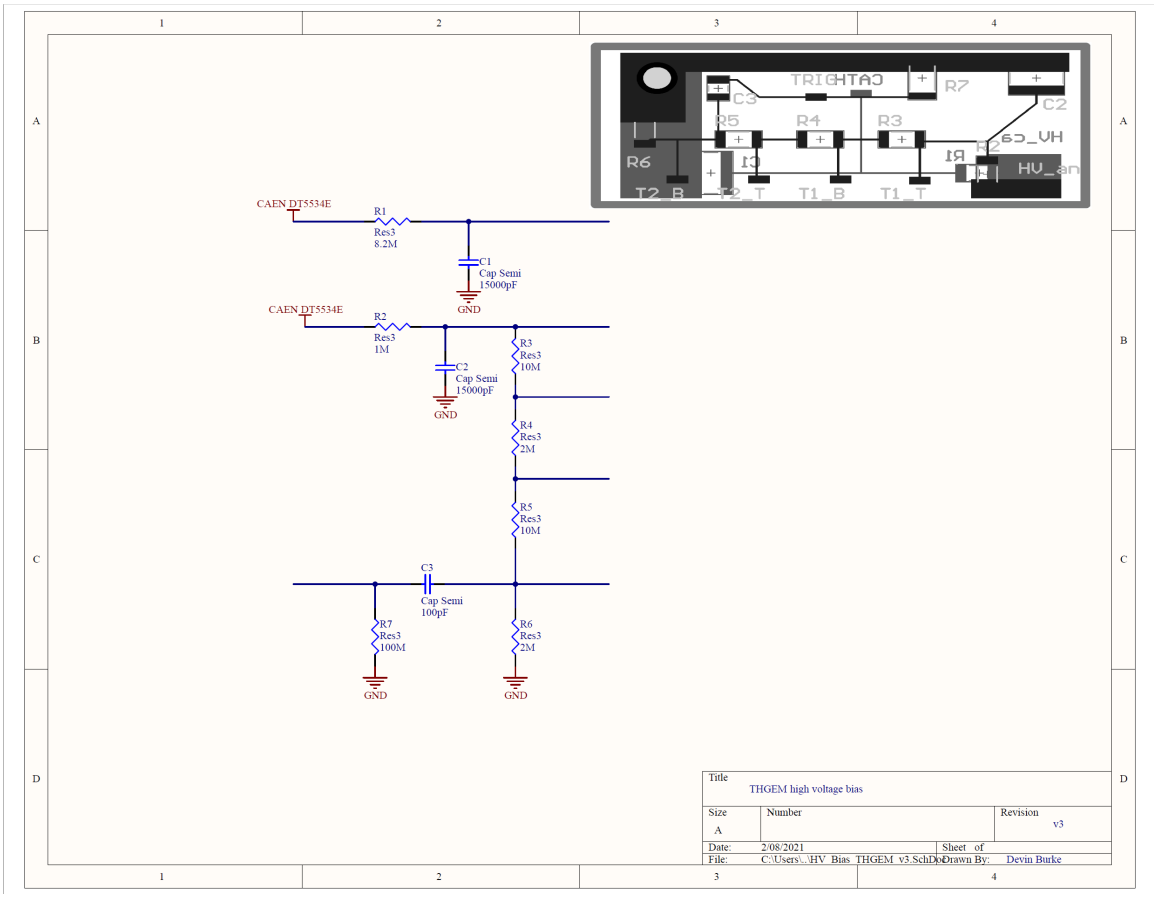

Figure A.1: Schematic and PCB layout for high voltage bias. Low pass filter pads are not populated on the PCB, components are housed in external module.

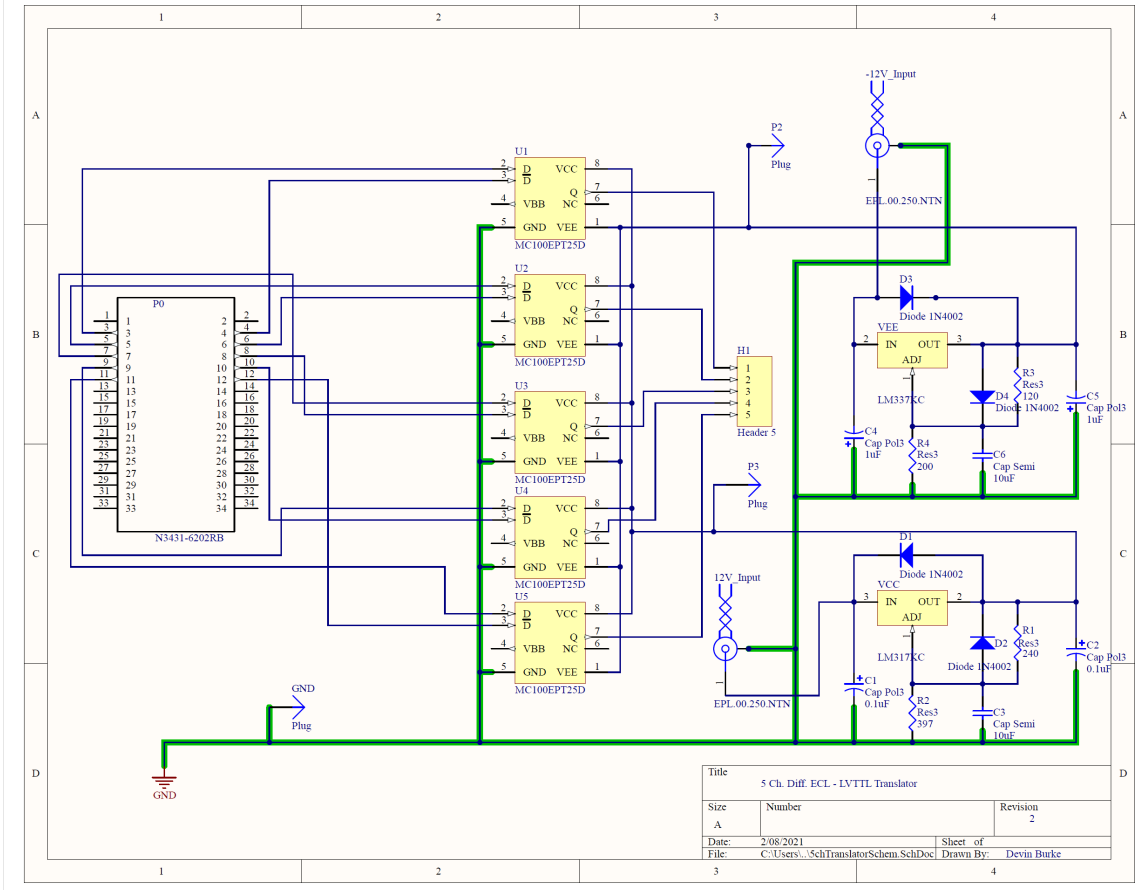

Figure A.2: Electrical schematic for 5 channel Diff. ECL to LVTTL translator.

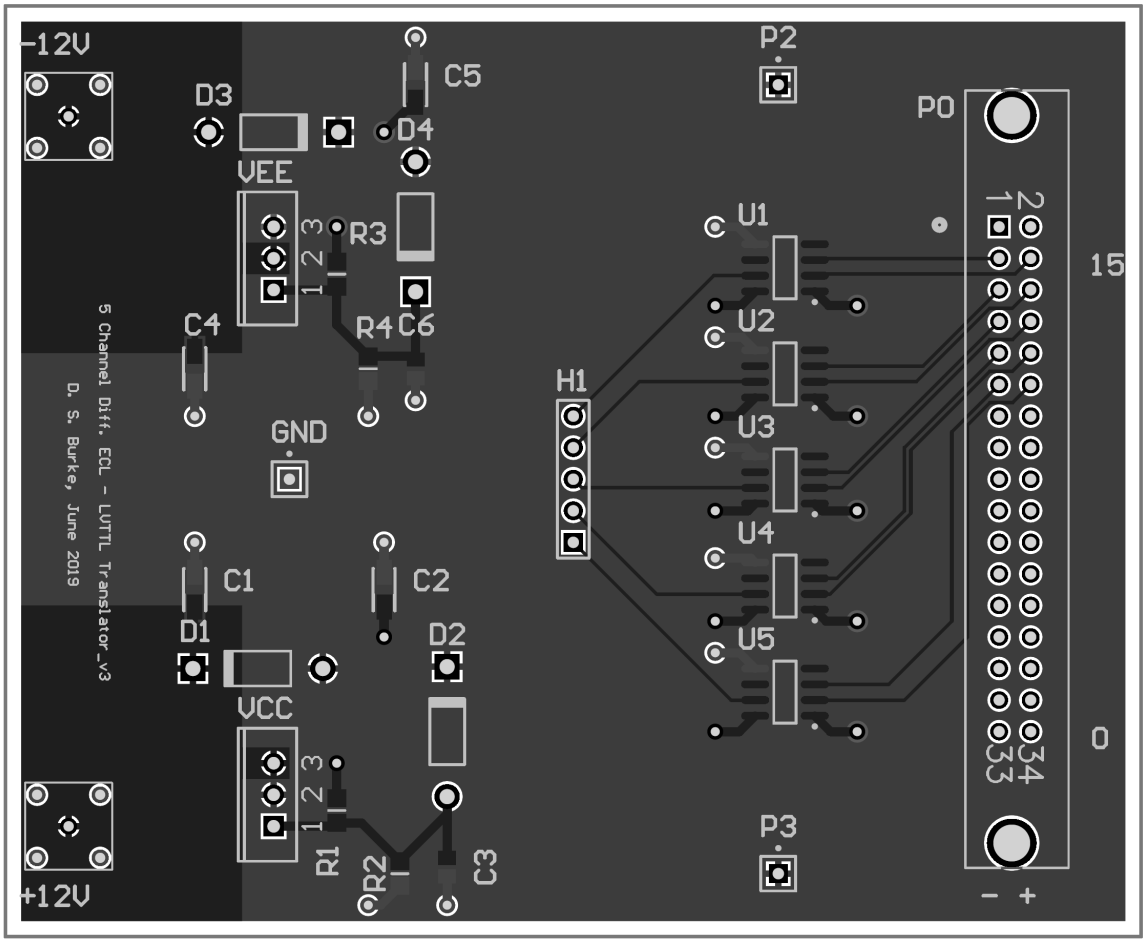

Figure A.3: PCB layer for 5 channel Diff. ECL to LVTTL translator.

#	Name	Material	Type	Weight	Thickness	Dk	Df
	Top Overlay		Overlay				
	Top Solder	Solder Resist	Solder Mask		0.4mil	3.5	
1	Signal Layer		Signal	1oz	1.4mil		
	Dielectric 1	FR-4	Core		10mil	4.2	
2	VCC Layer		Signal	1oz	1.417mil		
	Dielectric 2		Prepreg		5mil	4.2	
3	GND Layer		Signal	1oz	1.417mil		
	Dielectric 3	FR-4	Core		10mil	4.2	
4	VEE Layer		Signal	1oz	1.4mil		
	Bottom Solder	Solder Resist	Solder Mask		0.4mil	3.5	
	Bottom Overlay		Overlay				

Figure A.4: Schematic of PCB layer stack for 5 channel Diff. ECL to LVTTL translator.

Appendix B

Python analysis code

```
1  # -*- coding: utf-8 -*-
2  """
3  Created on Fri Nov 15 10:40:53 2019
4
5  @author: burkeds
6  """
7  import sys
8  import numpy as np
9  from matplotlib.image import NonUniformImage
10 import matplotlib as mpl
11 import matplotlib.pyplot as plt
12 """
13
14 Get total number of events N which satisy trigger conditions
15 initialize N dimensional arrays
16 """
17 """
18 test data
```

```
19 make sure N is the number of events in the file
20 make sure bins and timelimit are the same as those used to generate flatfield
21 """
22 testfile = open(r"C:\\Users\\Devin\\OneDrive - McMaster University\\Tests\\beamline\\
23 # N is the number of events
24 lines = testfile.read().splitlines()
25 eventno = int(lines[-6].split()[2])
26 N = eventno
27 #N = 249530
28 bins = 1024
29 timelimit = 58 #set positive and negative limit of time of flight axis
30 flatflag = 1 #flat field corrects the image. You must run flatfield.py first.
31 logflag = 0 #adds log colour scale to image
32 offsetflag = 0 #subtracts mean axis values from exposed image to account for left/ri
33 darkflag = 0
34 #interp = 'gaussian' #image interpolation
35 interp = 'gaussian'
36 ptitle = 'Cd cut, 128x128, FF, 32 cell'
37
38 yaxmean = 7.109000000000009
39 xaxmean = -8.605999999999995
40
41 #Select image type. Only flag one as true
42 nonuniformimage_flag = 0
43 imshow_flag = 1
44 pcolormesh_flag = 0
45
46 #axis of interest select
47 axX = 15
```

```
48 axY = 15
49
50
51
52 xmin = -timelimit
53 xmax = timelimit
54 ymin = -timelimit
55 ymax = timelimit
56 stepsizex = (xmax-xmin)/float(bins)
57 stepsizey = (ymax-ymin)/float(bins)
58
59 #Define bin edges
60 xedges = np.arange(xmin, xmax+stepsizex, stepsizex, float)
61 yedges = np.arange(ymin, ymax+stepsizey, stepsizey, float)
62
63 # Select pixel resolution
64
65 #bin_edges = [[xmin, xmax], [ymin, ymax]]
66
67 # data arrays
68 t1 = np.zeros(N)
69 t2 = np.zeros(N)
70 t3 = np.zeros(N)
71 t4 = np.zeros(N)
72 d12 = np.zeros(N)
73 d34 = np.zeros(N)
74
75 index = 0
76
```

```
77 for line in lines:
78     if line[0] == "2":
79         t1[index] = float(line.split()[5])
80
81     if line[0] == "3":
82         t2[index] = float(line.split()[5])
83
84     if line[0] == "4":
85         t3[index] = float(line.split()[5])
86
87     if line[0] == "5":
88         t4[index] = float(line.split()[5])
89         index+=1
90
91
92 testfile.close()
93
94 #data arrays for differences between pairs of arrays
95
96 d12 = np.array(N)
97 d34 = np.array(N)
98
99 d12 = t1-t2
100 d34 = t3-t4
101
102 if (offsetflag):
103     #subtract mean values from the flatfield to account for timing offset
104     d12 = d12 - yaxmean
105     d34 = d34 - xaxmean
```

```
106
107 h1, xedges, yedges = np.histogram2d(d12, d34, (xedges, yedges))
108
109 if darkflag == 1:
110     darkcurrent = np.load('./darkcurrent.npy')
111     h1 = h1-darkcurrent
112
113 if (flatflag):
114     #use flatfield image to correct test data
115     flatfield = np.load('./flatfield.npy')
116     h1 = np.multiply(h1, flatfield)
117
118 h1 = h1.astype(int)
119
120 #make image
121 fig = plt.figure(0)
122 fig.clf()
123
124 if (nonuniformimage_flag):
125     ax = fig.add_subplot(111)
126     ax.set_title(ptitle + ' nonuniformimage')
127     if (logflag):
128         im = NonUniformImage(ax, interpolation=interp, norm=mpl.colors.LogNorm(), cma
129     else:
130         im = NonUniformImage(ax, interpolation=interp, cmap=mpl.cm.gray)
131     xcenters = xedges[:-1] + 0.5 * (xedges[1:] - xedges[:-1])
132     ycenters = yedges[:-1] + 0.5 * (yedges[1:] - yedges[:-1])
133     im.set_data(xcenters, ycenters, h1)
134     ax.images.append(im)
```

```
135     ax.set_xlim(xedges[0], xedges[-1])
136     ax.set_ylim(yedges[0], yedges[-1])
137     ax.set_aspect('equal')
138     plt.show()
139
140 if (imshow_flag):
141     ax = fig.add_subplot(111)
142     ax.set_title(ptitle)
143     if (logflag):
144         plt.imshow(h1, interpolation = interp, aspect='equal', origin = 'low', extent
145     else:
146         plt.imshow(h1, interpolation = interp, aspect = 'equal', origin = 'low', exte
147
148 if (pcolormesh_flag):
149     ax = fig.add_subplot(111)
150     ax.set_title(ptitle + ' pcolormesh')
151     ax.set_aspect('equal')
152     X, Y = np.meshgrid(xedges, yedges)
153     if (logflag):
154         ax.pcolormesh(X, Y, h1, norm=mpl.colors.LogNorm(), cmap=mpl.cm.gray)
155     else:
156         ax.pcolormesh(X, Y, h1, cmap=mpl.cm.gray)
157
158 #Create histograms
159 #Select an axis of interest
160 xselect = h1[:,axX]
161 plt.figure(1)
162 plt.clf()
163 xaxis = np.arange(len(xselect))
```

```
164 xedges = np.arange(xmin, xmax+stepsizex, stepsizex, float)
165 plt.bar(xaxis, xselect, width=1.0)
166
167 yselect = h1[axY,:]
168 plt.figure(2)
169 plt.clf()
170 yaxis = np.arange(len(yselect))
171 plt.bar(yaxis, yselect, width=1.0)
172
173 #output histograms to text
174
175 np.savetxt('test.txt', h1[axY,:])
176 np.save('./output',h1)
```

```
1  # -*- coding: utf-8 -*-
2  """
3  Created on Thu Jan  9 15:52:20 2020
4
5  @author: burkeds
6  """
7  import sys
8  import numpy as np
9  from matplotlib.image import NonUniformImage
10 import matplotlib as mpl
11 import matplotlib.pyplot as plt
12 """
13
14 Get total number of events N which satisy trigger conditions
15 initialize N dimensional arrays
16 """
```

```
17 """
18 test data
19 """
20
21 np.set_printoptions(threshold=sys.maxsize)
22 testfile = open(r"C:\\Users\\Devin\\OneDrive - McMaster University\\Tests\\beamline\\
23 #testfile = open(r"C:\\Users\\USER\\Desktop\\Nov27\\test.dat","r")
24 # N is the number of events
25 lines = testfile.read().splitlines()
26 eventno = int(lines[-6].split()[2])
27 N = eventno
28 #N =  249530
29 bins = 1024
30 timelimit = 58
31 logflag = 0
32 darkflag = 0
33
34
35 xmin = -timelimit
36 xmax = timelimit
37 ymin = -timelimit
38 ymax = timelimit
39
40 # Select pixel resolution
41
42 bin_edges = [[xmin, xmax], [ymin, ymax]]
43
44 """
45 xmin = -200.0
```

```
46 xmax = 200.0
47 ymin = -200.0
48 ymax = 200.0
49 """
50
51 # data arrays
52 t1 = np.zeros(N)
53 t2 = np.zeros(N)
54 t3 = np.zeros(N)
55 t4 = np.zeros(N)
56 d12 = np.zeros(N)
57 d34 = np.zeros(N)
58
59 index = 0
60
61 for line in lines:
62     if line[0] == "2":
63         t1[index] = float(line.split()[5])
64
65     if line[0] == "3":
66         t2[index] = float(line.split()[5])
67
68     if line[0] == "4":
69         t3[index] = float(line.split()[5])
70
71     if line[0] == "5":
72         t4[index] = float(line.split()[5])
73         index+=1
74
```

```
75
76  testfile.close()
77
78  #data arrays for differences between pairs of arrays
79
80  d12 = np.array(N)
81  d34 = np.array(N)
82
83  d12 = t1-t2
84  d34 = t3-t4
85
86  ymean = 0.0
87  Ny = 0.0
88  for y in d12:
89      if (y > -1*timelimit):
90          if (y < timelimit):
91              ymean += y
92              Ny += 1.0
93  ymean = ymean / Ny
94
95  xmean = 0.0
96  Nx = 0.0
97  for x in d34:
98      if (x > -1*timelimit):
99          if (x < timelimit):
100             xmean += x
101             Nx += 1.0
102 xmean = xmean / Nx
103
```

```
104
105 print('y-axis mean: ', ymean, " ns")
106 print('x-axis mean: ', xmean, " ns")
107 print('y-axis median: ', np.median(d12), " ns")
108 print('x-axis median: ', np.median(d34), " ns")
109
110 scalefactor = 1
111
112
113
114 hist2d1 = np.histogram2d(d12, d34, [bins, bins], bin_edges, normed = False)
115 h1 = hist2d1[0]
116 h1 = h1 + 1
117
118
119
120 if darkflag == 1:
121     darkfile = open(r"C:\\Users\\dburk\OneDrive - McMaster University\\Tests\\photon
122     lines = darkfile.read().splitlines()
123     eventno = int(lines[-6].split()[2])
124     N = eventno
125
126     t1 = np.zeros(N)
127     t2 = np.zeros(N)
128     t3 = np.zeros(N)
129     t4 = np.zeros(N)
130     d12 = np.zeros(N)
131     d34 = np.zeros(N)
132
```

```
133     index = 0
134
135     for line in darkfile:
136         if line[0] == "2":
137             t1[index] = float(line.split()[5])
138
139         if line[0] == "3":
140             t2[index] = float(line.split()[5])
141
142         if line[0] == "4":
143             t3[index] = float(line.split()[5])
144
145         if line[0] == "5":
146             t4[index] = float(line.split()[5])
147             index+=1
148
149
150     darkfile.close()
151     d12 = np.array(N)
152     d34 = np.array(N)
153
154     d12 = t1-t2
155     d34 = t3-t4
156
157     hist2d1 = np.histogram2d(d12, d34, [bins, bins], bin_edges, normed = False)
158     h2 = hist2d1[0]
159     np.save('./darkcurrent',h2)
160
161     h1 = h1-h2
```

```
162
163 for tester in h1:
164     for index in tester:
165         index = 0
166
167 h1 = np.mean(h1)/h1 * scalefactor
168
169 np.save('./flatfield', h1)
```

Appendix C

Preliminary work to prepare RETGEMs by electroplating Ge

Here is presented a procedural outline to manufacture a RETGEM produced by electroplating Ge onto a THGEM. The Ge will act as a resistive coating on a THGEM to protect it from high voltage discharge damage. Pre-manufactured THGEMs are first electropolished to clean the copper surfaces and prepare them for plating. A THGEM is then placed in a dilute solution of $GeCl_4$ in propylene glycol in a double-sided electroplating setup with two graphite anodes. A schematic layout is seen in Figure C.1.

Electrochemical polishing of substrate [68]

1. Prepare solution of 2 parts H_3PO_4, 1 part distilled water.

2. (Optional) add 1.5 g gelatin to polishing solution. Gelatin tends to gather in THGEM holes and requires an extra cleaning step to remove. Polishing appears

effective without this step.

3. Apply 1.7 V between anode and cathode elements. Graphite rods will function as an anode by plates are preferred for more even plating thickness.

4. When surface is mirror-like rinse with distilled water and allow to dry.

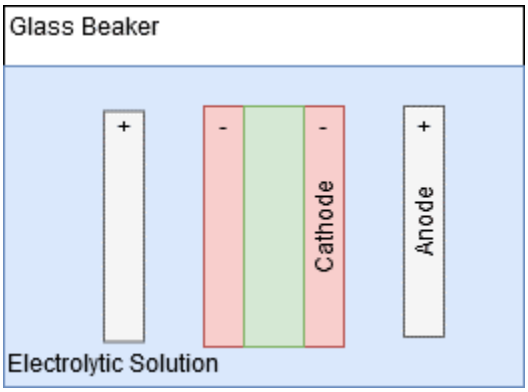

Figure C.1: Schematic double sided electroplating setup to plate Ge onto copper from a 5% by volume solution of $GeCl_4$.

Electroplating procedure [69]

1. Prepare 5% vol solution of $GeCl_4$ in propylene glycol.

2. Rinse, dry and reuse graphite from polishing step and prepare setup.

3. Apply voltage until current density 100 mA/cm^2 is satisfied.

4. Keep solution at room temperature, this will require a cooling strategy.

5. Plate to desired thickness. Expected growth rate 0.62 ± 0.2 nm/s [69].

This procedure was attempted with a standard laboratory desktop power supply. Electropolishing results are seen in Figure C.2. Resulting THGEMs have a mirror

finish. Various sources in literature recommend adding gelatin to polishing solution however in testing it was observed that the gelatin solution would froth until it touched the sample holder and gelatin would build up in the THGEM holes. It was decided not to include it in later tests. When electroplating was attempted several issues were discovered that will need to be resolved before this can be attempted again. The THGEMs used in this work have large copper areas to plate, approximately 26.1 cm^2, necessitating a target current of 2.61 A. The plating solution is not very conductive; the total current of 0.122 A at our supply's highest voltage setting of 8.20 V was measured. Furthermore if the target current were meant, the solution would rapidly approach its flash point. Without the equipment necessary to safely apply the necessary current while keeping the solution this experiment cannot be completed at this time. Future experimental designs should be developed in cooperation with experienced electroplating research groups with the necessary equipment or industrial partners.

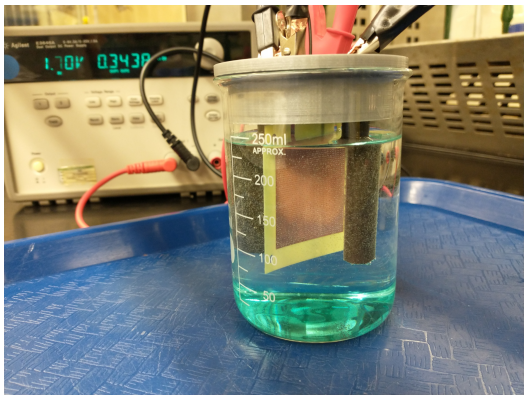

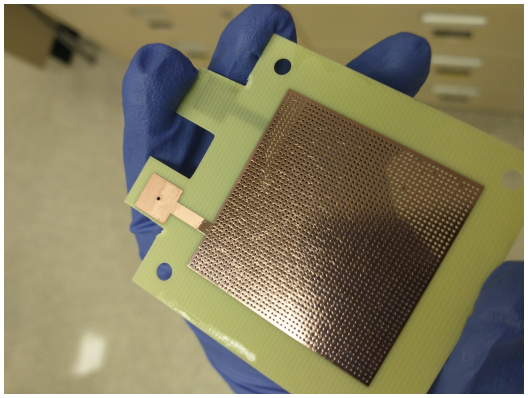

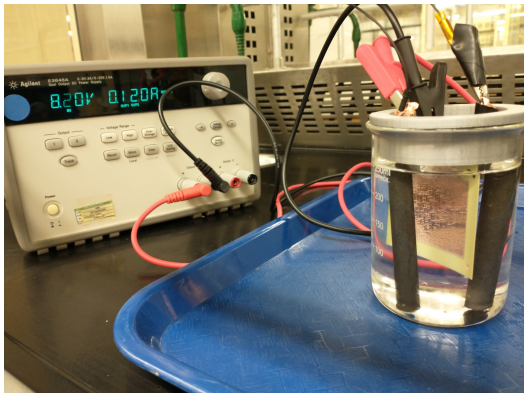

Figure C.2: a) electropolishing a THGEM, b) a polished THGEM, and c) attempting to reach 100 mA/cm^2 current density

Bibliography

[1] Nikolay Kardjilov, Ingo Manke, Robin Woracek, André Hilger, and John Banhart. Advances in neutron imaging. *Materials Today*, 21(6):652–672, 2018.

[2] NB Selvaraj, J Czub, H Figiel, D Chapelle, N Kardjilov, A Hilger, I Manke, et al. Imaging of an operating lani4. 8al0. 2–based hydrogen storage container. *international journal of hydrogen energy*, 36(16):9751–9757, 2011.

[3] HK Jenssen and BC Oberländer. Improvements in pie-techniques at the ife hot-laboratory.'neutron radiography, three dimensional profilometry and image compilation of pie data for visualization in an image based user-interface'. 2002.

[4] Genoveva Burca, Sri Nagella, Thomas Clark, Dimitar Tasev, Imran A Rahman, Russell J Garwood, Alan RT Spencer, Martin J Turner, and Joe F Kelleher. Exploring the potential of neutron imaging for life sciences on imat. *Journal of microscopy*, 272(3):242–247, 2018.

[5] Krysta Ryzewski, S Herringer, H Bilheux, Lakeisha Walker, B Sheldon, S Voisin, J-C Bilheux, and V Finocchiaro. Neutron imaging of archaeological bronzes at the oak ridge national laboratory. *Physics Procedia*, 43:343–351, 2013.

[6] Toru Matoh. Boron in plant cell walls. *Plant and Soil*, 193(1):59–70, 1997.

[7] Martin Dawson, Jane Francis, and Rosemary Carpenter. New views of plant fossils from antarctica: a comparison of x-ray and neutron imaging techniques. *Journal of Paleontology*, 88(4):702–707, 2014.

[8] Tapan Chatterji. Chapter 1 - magnetic neutron scattering. In Tapan Chatterji, editor, *Neutron Scattering from Magnetic Materials*, pages 1–24. Elsevier Science, Amsterdam, 2006. ISBN 978-0-444-51050-1. doi: https://doi.org/10.1016/B978-044451050-1/50002-1. URL `https://www.sciencedirect.com/science/article/pii/B9780444510501500021`.

[9] Nuclear security report 2020, international atomic energy agency, 2020. GOV/2020/31-GC(64)/6*.

[10] Hajir Al Hamrashdi, Stephen D Monk, and David Cheneler. Passive gamma-ray and neutron imaging systems for national security and nuclear non-proliferation in controlled and uncontrolled detection areas: Review of past and current status. *Sensors*, 19(11):2638, 2019.

[11] Marc G Paff, Shaun D Clarke, Richard T Kouzes, and Sara A Pozzi. Fast and thermal neutron detectors for radiation portal monitors. In *2017 IEEE Nuclear Science Symposium and Medical Imaging Conference (NSS/MIC)*, pages 1–2. IEEE, 2017.

[12] DJ Thomas and AV Alevra. Bonner sphere spectrometers—a critical review. *Nuclear Instruments and Methods in Physics Research Section A: Accelerators, Spectrometers, Detectors and Associated Equipment*, 476(1-2):12–20, 2002.

[13] Dana A Shea and Daniel L Morgan. The helium-3 shortage: Supply, demand, and options for congress, 2010.

[14] Michael E Moore, Joris Lousteau, Pavel Trtik, Hassina Z Bilheux, Diego Pugliese, Daniel Milanese, Angela T Simone, Gilberto Brambilla, and Jason P Hayward. Fabrication and experimental evaluation of microstructured 6li silicate fiber arrays for high spatial resolution neutron imaging. *Nuclear Instruments and Methods in Physics Research Section A: Accelerators, Spectrometers, Detectors and Associated Equipment*, 954:161695, 2020.

[15] A Stoykov, J-B Mosset, U Greuter, M Hildebrandt, and N Schlumpf. A sipm-based zns: 6lif scintillation neutron detector. *Nuclear Instruments and Methods in Physics Research Section A: Accelerators, Spectrometers, Detectors and Associated Equipment*, 787:361–366, 2015.

[16] John EM Goldsmith, Mark D Gerling, and James S Brennan. A compact neutron scatter camera for field deployment. *Review of Scientific Instruments*, 87(8): 083307, 2016.

[17] Y Giomataris. Development and prospects of the new gaseous detector "micromegas". *Nuclear Instruments and Methods in Physics Research Section A: Accelerators, Spectrometers, Detectors and Associated Equipment*, 419(2-3):239–250, 1998.

[18] Georges Charpak, J Derre, Y Giomataris, and Ph Rebourgeard. Micromegas, a multipurpose gaseous detector. *Nuclear Instruments and Methods in Physics Research Section A: Accelerators, Spectrometers, Detectors and Associated Equipment*, 478(1-2):26–36, 2002.

[19] F Belloni, F Gunsing, and T Papaevangelou. Micromegas for neutron detection and imaging. *Modern Physics Letters A*, 28(13):1340023, 2013.

[20] G. Tsiledakis, A. Delbart, D. Desforge, I. Giomataris, A. Menelle, and T. Papaevangelou. A large high-efficiency multi-layered micromegas thermal neutron detector. *Journal of Instrumentation*, 12(09):P09006–P09006, sep 2017. doi: 10.1088/1748-0221/12/09/p09006. URL `https://doi.org/10.1088/1748-0221/12/09/p09006`.

[21] Rachel Chechik, Marco Cortesi, Amos Breskin, David Vartsky, D Bar, and V Dangendorf. Thick gem-like (thgem) detectors and their possible applications. *arXiv preprint physics/0606162*, 2006.

[22] Ian S Anderson, Robert L McGreevy, and Hassina Z Bilheux. *Neutron Imaging and Applications*. Number 1868-0372 in Neutron Scattering Applications and Techniques. Springer US, 1 edition, 2009. ISBN 978-1-4419-4619-5.

[23] Glenn F. Knoll. *Radiation Detection and Measurement*. Wiley India Pvt. Ltd., 4 edition, 2010. ISBN 978-0-470-13148-0.

[24] MA Gryzinski and M Wielgosz. Intelligent uranium fission converter for neutron production on the periphery of the nuclear reactor core (maria reactor in swierk-poland). Technical report, Institute of Electrical and Electronics Engineers-IEEE, 3 Park Avenue, 17th ..., 2015.

[25] Said Mughabghab. *Atlas of Neutron Resonances*, volume 2: Resonance Properties and Thermal Cross Sections Z=61-102. Elsevier Science, 6 edition, 2018. ISBN 9780444637864.

[26] Yoshinori Sakurai and Tooru Kobayashi. Experimental verification of the nuclear data of gadolinium for neutron capture therapy. *Journal of Nuclear Science and Technology*, 39(sup2):1294–1297, 2002.

[27] Richard T Kouzes, James H Ely, Luke E Erikson, Warnick J Kernan, Azaree T Lintereur, Edward R Siciliano, David C Stromswold, and Mitchell L Woodring. Alternative neutron detection testing summary. Technical report, Pacific Northwest National Lab.(PNNL), Richland, WA (United States), 2010.

[28] Kevin S McKinny, Thomas R Anderson, and Nathan H Johnson. Optimization of coating in boron-10 lined proportional counters. *IEEE Transactions on Nuclear Science*, 60(2):860–863, 2012.

[29] I Stefanescu, Y Abdullahi, Jens Birch, I Defendi, Richard Hall-Wilton, Carina Höglund, Lars Hultman, M Zee, and K Zeitelhack. A 10b-based neutron detector with stacked multiwire proportional counters and macrostructured cathodes. *Journal of Instrumentation*, 8(12):P12003, 2013.

[30] Francesco Piscitelli, Francesco Messi, Michail Anastasopoulos, Tomasz Bryś, Faye Chicken, Eszter Dian, Janos Fuzi, Carina Höglund, Gabor Kiss, Janos Orban, et al. The multi-blade boron-10-based neutron detector for high intensity neutron reflectometry at ess. *Journal of Instrumentation*, 12(03):P03013, 2017.

[31] Christian Cowles, Spencer Behling, Phoenix Baldez, Micah Folsom, Richard Kouzes, Vladislav Kukharev, Azaree Lintereur, Sean Robinson, Edward Siciliano, Sean Stave, et al. Development of a lithium fluoride zinc sulfide based

neutron multiplicity counter. *Nuclear Instruments and Methods in Physics Research Section A: Accelerators, Spectrometers, Detectors and Associated Equipment*, 887:59–63, 2018.

[32] Pavel Trtik, Jan Hovind, Christian Grünzweig, Alex Bollhalder, Vincent Thominet, Christian David, Anders Kaestner, and Eberhard H Lehmann. Improving the spatial resolution of neutron imaging at paul scherrer institut–the neutron microscope project. *Physics Procedia*, 69:169–176, 2015.

[33] Christian Tötzke, Nikolay Kardjilov, Ingo Manke, and Sascha E Oswald. Capturing 3d water flow in rooted soil by ultra-fast neutron tomography. *Scientific reports*, 7(1):1–9, 2017.

[34] AP Kaestner, S Hartmann, G Kühne, G Frei, C Grünzweig, L Josic, F Schmid, and EH Lehmann. The icon beamline–a facility for cold neutron imaging at sinq. *Nuclear Instruments and Methods in Physics Research Section A: Accelerators, Spectrometers, Detectors and Associated Equipment*, 659(1):387–393, 2011.

[35] Sea Agostinelli, John Allison, K al Amako, John Apostolakis, H Araujo, P Arce, M Asai, D Axen, S Banerjee, G 2 Barrand, et al. Geant4—a simulation toolkit. *Nuclear instruments and methods in physics research section A: Accelerators, Spectrometers, Detectors and Associated Equipment*, 506(3):250–303, 2003.

[36] James Ziegler. The stopping and range of ions in matter. `http://www.srim.org/`, 2013.

[37] F Sears Varley. Neutron scattering lengths and cross sections. *Neutron news*, 3 (3):29–37, 1992.

[38] L Periale, V Peskov, P Carlson, T Francke, P Pavlopoulos, P Picchi, and F Pietropaolo. Detection of the primary scintillation light from dense ar, kr and xe with novel photosensitive gaseous detectors. *Nuclear Instruments and Methods in Physics Research Section A: Accelerators, Spectrometers, Detectors and Associated Equipment*, 478(1-2):377–383, 2002.

[39] Amos Breskin, R Alon, M Cortesi, R Chechik, J Miyamoto, V Dangendorf, JM Maia, and JMF Dos Santos. A concise review on thgem detectors. *Nuclear Instruments and Methods in Physics Research Section A: Accelerators, Spectrometers, Detectors and Associated Equipment*, 598(1):107–111, 2009.

[40] GM Orchard, K Chin, WV Prestwich, AJ Waker, and SH Byun. Development of a thick gas electron multiplier for microdosimetry. *Nuclear Instruments and Methods in Physics Research Section A: Accelerators, Spectrometers, Detectors and Associated Equipment*, 638(1):122–126, 2011.

[41] A Hanu, SH Byun, and WV Prestwich. A monte carlo simulation of the microdosimetric response for thick gas electron multiplier. *Nuclear Instruments and Methods in Physics Research Section A: Accelerators, Spectrometers, Detectors and Associated Equipment*, 622(1):270–275, 2010.

[42] MR Bernacci and SH Byun. Development of a thick gas electron multiplier-based beta-ray detector. *Nuclear Instruments and Methods in Physics Research Section A: Accelerators, Spectrometers, Detectors and Associated Equipment*, 954: 161531, 2020.

[43] Andrei Hanu. *Development of a THGEM imaging detector with delay line readout*. PhD thesis, McMaster University, 2014.

[44] P Ray, G Baishali, V Radhakrishna, and K Rajanna. Spatial resolution optimization in a thgem-based uv photon detector. *Radiation Detection Technology and Methods*, 2(2):1–7, 2018.

[45] AR Hanu, WV Prestwich, and SH Byun. A data acquisition system for two-dimensional position sensitive micropattern gas detectors with delay-line readout. *Nuclear Instruments and Methods in Physics Research Section A: Accelerators, Spectrometers, Detectors and Associated Equipment*, 780:33–39, 2015.

[46] IPC (November 2012). Generic standard on printed board design. *IPC-2221B*. URL `https://www.ipc.org`.

[47] Berkeley Nucleonics Corporation. Model pb-5 precision nim pulse generator. URL `https://www.berkeleynucleonics.com/model-pb-5-precision-nim-pulse-generator`.

[48] CAEN S.p.A. N1068 16 ch programmable spectroscopy amplifier and 16 ch cfd. URL `https://www.caen.it/products/n1068/`.

[49] Caen 16ch. spectroscopy amplifier and cfd rev. 4, 2018.

[50] Muhammad Arif Sazali, Nahrul Khair Alang Md Rashid, and Khaidzir Hamzah. A review on multilayer radiation shielding. In *IOP Conference Series: Materials Science and Engineering*, volume 555, page 012008. IOP Publishing, 2019.

[51] Yang Dong Huo Junde, Huo Su. Nuclear data sheets 11, 1513 (2011). Data extracted from the ENSDF database, version of June 4th, 2020, IAEA Nuclear Data Services.

[52] C.M. Baglin. Nuclear data sheets 111, 275 (2010). Data extracted from the ENSDF database, version of Jan 11th, 2021, IAEA Nuclear Data Services.

[53] Yao Cai, Huasi Hu, Ziheng Pan, Guang Hu, and Tao Zhang. A method to optimize the shield compact and lightweight combining the structure with components together by genetic algorithm and mcnp code. *Applied Radiation and Isotopes*, 139:169–174, 2018.

[54] Guang Hu, Huasi Hu, Quanzhan Yang, Bo Yu, and Weiqiang Sun. Study on the design and experimental verification of multilayer radiation shield against mixed neutrons and γ-rays. *Nuclear Engineering and Technology*, 52(1):178–184, 2020.

[55] C Grünzweig, G Frei, E Lehmann, G Kühne, and C David. Highly absorbing gadolinium test device to characterize the performance of neutron imaging detector systems. *Review of Scientific instruments*, 78(5):053708, 2007.

[56] ASTM E545-19, standard test method for determining image quality in direct thermal neutron radiographic examination. URL `http://www.astm.org/cgi-bin/resolver.cgi?E545`. ASTM International, West Conshohocken, PA, 2019,.

[57] Boris Pritychenko, E Běták, MA Kellett, B Singh, and J Totans. The nuclear science references (NSR) database and web retrieval system. *Nuclear Instruments and Methods in Physics Research Section A: Accelerators, Spectrometers, Detectors and Associated Equipment*, 640(1):213–218, 2011.

[58] J Dumazert, R Coulon, Q Lecomte, GHV Bertrand, and M Hamel. Gadolinium for neutron detection in current nuclear instrumentation research: A review.

Nuclear Instruments and Methods in Physics Research Section A: Accelerators, Spectrometers, Detectors and Associated Equipment, 882:53–68, 2018.

[59] Danielle Castley, Cameron Goodwin, and Jifeng Liu. Computational and experimental comparison of boron carbide, gadolinium oxide, samarium oxide, and graphene platelets as additives for a neutron shield. *Radiation Physics and Chemistry*, 165:108435, 2019.

[60] United states air force document mil-std-150, 1959.

[61] McMaster nuclear operations & facilities. 1280 Main St. W. Hamilton, ON L8S 4K1.

[62] McMaster alignment diffractometer. McMaster University, Nuclear Operations and Facilities.

[63] E Lehmann, D Mannes, A Kaestner, and C Grünzweig. Recent applications of neutron imaging methods, 2017.

[64] David N. Sitter, James S. Goddard, and Regina K. Ferrell. Method for the measurement of the modulation transfer function of sampled imaging systems from bar-target patterns. *Appl. Opt.*, 34(4):746–751, Feb 1995. doi: 10.1364/AO.34.000746. URL `http://ao.osa.org/abstract.cfm?URI=ao-34-4-746`.

[65] M Cortesi, S Rost, W Mittig, Y Ayyad-Limonge, D Bazin, J Yurkon, and A Stolz. Multi-layer thick gas electron multiplier (m-thgem): A new mpgd structure for high-gain operation at low-pressure. *Review of Scientific Instruments*, 88(1): 013303, 2017.

[66] M Cortesi, R Alon, R Chechik, A Breskin, D Vartsky, and V Dangendorf. Investigations of a thgem-based imaging detector. *Journal of Instrumentation*, 2(09): P09002, 2007.

[67] G Agocs, B Clark, P Martinego, R Oliveira, V Peskov, P Pietropaolo, and P Picchi. Developments and the preliminary tests of resistive gems manufactured by a screen printing technology. *Journal of Instrumentation*, 3(02):P02012, 2008.

[68] AM Awad, NA Abdel Ghany, and TM Dahy. Removal of tarnishing and roughness of copper surface by electropolishing treatment. *Applied Surface Science*, 256(13):4370–4375, 2010.

[69] Masatoshi Saitou, K Sakae, and W Oshikawa. Evaluation of crystalline germanium thin films electrodeposited on copper substrates from propylene glycol electrolyte. *Surface and Coatings Technology*, 162(1):101–105, 2003.